2003 Edward DeMille Campbell Memorial Lecture
ASM International

Phase Diagram Calculations in Teaching, Research, and Industry

Y. AUSTIN CHANG

I have a long-standing interest in alloy thermodynamics/phase diagrams and in utilizing the principles of this subject for materials research and engineering applications. At the same time, I also have a long association with ASM International as a member and a former Trustee of the Society. The Society's initiative in promoting critical assessments of phase diagrams beginning in the late 1970s rekindled this field and stimulated further research, particularly in phase diagram calculations. Significant advancements have been made in phase diagram calculations using the Calphad approach since the late 1980s due primarily to the availability of inexpensive computers and robust software. In this article, I first present the use of computational thermodynamics including phase diagram calculation in teaching, next the use of calculated phase diagrams, particularly for multicomponent systems, for materials research/development, and manufacturing, and last describe some current research in advancing this methodology when the phases involve ordering with decreasing temperature.

Y. AUSTIN CHANG, Wisconsin Distinguished Professor, Department of Materials Science and Engineering, College of Engineering, University of Wisconsin–Madison, Madison, WI 53706-1595. He received his BS from the University of California–Berkeley and his MS from the University of Washington–Seattle, both in Chemical Engineering, and his Ph.D. in Metallurgy from the University of California–Berkeley. After spending 4 years in industry, he joined the faculty of the College of Engineering and Applied Science, University of Wisconsin–Milwaukee, as Associate Professor in 1967 and was promoted to Professor in 1970. He served as the Chair of the Materials Department from 1971 to 1977 and then as the Associate Dean for Research in the Graduate School from 1978–1980. In 1980, he joined the faculty of the University of Wisconsin–Madison, in the Fall of 1980 as Professor, served as the Chair of the Department of Materials Science and Engineering from 1982 to 1991, and was named Wisconsin Distinguished Professor in 1988. He delivered the Edward DeMille Campbell Lecture at the Annual ASM International (ASM) Meeting, Pittsburgh, PA, on October 14, 2003.

Professor Chang has a strong interest in research, teaching, and education. He is a Member of the National Academy of Engineering, a Foreign Member of the Chinese Academy of Sciences, and Fellow of ASM and the Minerals, Metals and Materials Society (TMS). He has focused his research on thermodynamic modeling/phase diagram calculation and in applying thermodynamics and kinetics to extraction/refining in his earlier career and then structural, electronic, and magnetic materials in bulk form as well as at the nanoscale. Among his recognitions are the Wisconsin Idea Fellow Award (UW System, 2004), a highly cited materials scientist covering the period 1981–1999 (ISHighlyCited, 2003), John Bardeen Award (TMS, 2000), Albert Sauveur Achievement Award (ASM, 1996), Champion H. Mathewson Medal (TMS, 1996), Extraction and Processing Lecturer Award (TMS, 1993), William Hume-Rothery Award (TMS, 1989), Belton Lecturer Award (CSIRO, Clayton, Victoria, Australia, 2000), Winchell Lecturer Award (Purdue University, 1999), Best Paper Award with Dr. W.-M. Huang (Alloy Phase Diagram International Commission or APDIC, 1999), Honorary Professorship (Northeast University, Shenyang, 1998–, Southeast University, Nanjing, 1997–, Central South University of Technology, Changsha, Hunan, 1996–, and University of Science and Technology Beijing, 1995–, all in the People's Republic of China), Summer Faculty (Quantum Structure Research Initiative, Hewlett-Packard Laboratory, Palo Alto, CA, 1999), Honorary Chair Professor (National Tsing Hua University, Hsinchu, Taiwan, Republic of China, 2002–2005), Visiting Professorship (MIT, 1991 and Tohoku University, Sendai, 1987), Honorary Life Membership of Alpha Sigma Mu (1985), and Byron Bird Award (University of Wisconsin–Madison, 1978). He also received recognitions in teaching and education: an Outstanding Instructor Award (University of Wisconsin–Milwaukee, 1972), Educator Award (TMS, 1990), and Albert Easton White Distinguished Teacher Award (ASM, 1994). He served as a Trustee of ASM (1981–1984), as the 2000 President of TMS, and as the National President of Alpha Sigma Mu (1984).

I. INTRODUCTION

WHEN I learned from Bill Scott of ASM International some time ago that I was selected to be the 2003 Edward DeMille Campbell Lecturer, my immediate reaction was to speak on a specific topic of research I have done in the past or on a research topic I am actively pursuing. However, I eventually decided to present an overview, undoubtedly a personal one, on the impact of Phase Diagram Calculations on Teaching, Research and Industrial Applications since the early 1980s. I made this decision for two reasons. First, I have a long-standing interest in thermodynamics and phase diagrams, and second, the field of phase diagrams is a subject of great interest to the ASM community. The leadership of the ASM, both their staff and the membership, has played an important role in revitalizing phase diagram research, particularly for data assessment and industrial applications since the early 1980s. In this article, I will first give a brief introduction and then stress the importance of phase diagram calculations in teaching. I will then present the application of phase diagram calculations or computational thermodynamics first for materials research/development, and then manufacturing. Finally, I will point to some possible future directions in research on phase diagram calculations.

Phase diagrams are roadmaps for materials and processing research/development. However, I believe that phase diagram calculations will in the near future make a difference even in manufacturing. Phase diagrams and thermodynamics are closely interrelated and can be considered as the same subject. For instance, when the thermodynamic properties of all the phases in a system are known, the phase diagram can be calculated. Recognizing the importance of phase diagrams in the materials world, leaders in the ASM community took the initiative in the late 1970s to raise funding to support phase diagram evaluation including thermodynamic modeling, where this was possible. This effort revitalized worldwide interest on the subject of "phase diagrams."[1] In the intervening years, significant advances have been made in calculating phase diagrams of multicomponent alloy systems built on the ASM activities on phase diagram data assessment. I will focus my effort on the use of the phenomenological approach to calculating phase diagrams, while recognizing the important contributions and advances being made by the "first principles" computational community. In particular, the first principles calculated energies at 0 K now often approach the accuracy of those measured by calorimetry. Further, they can just as easily provide information for metastable/unstable phases, something which experimentalists cannot do. The calculated values are just as useful as the measured values in developing thermodynamic databases.

II. TEACHING

For many years, I have been teaching a materials thermodynamics course to incoming graduate students and a senior level course on multicomponent phase equilibria with applications in mind to seniors and graduate students. I give one example in the following section, which I teach in the graduate level thermodynamics course in relating the characteristic features of a phase diagram in terms of the relative thermodynamic stabilities of the phases involved. Advances made in utilizing computers to calculate phase diagrams has made this exercise less challenging. The other example I give in this section following the first one is to utilize computer-calculated quaternary phase diagrams to help better visualize the paths of solidification of alloys.

A. *Relationship between the Characteristic Features of a Binary Phase Diagram and the Relative Thermodynamic Stabilities of the Phases Involved*

One of the important lessons a student should learn about phase diagrams from alloy thermodynamics lectures is that the characteristic features of a phase diagram are governed by the relative thermodynamic stabilities of the phases involved. For instance, in a binary T-composition phase diagram at constant T and p, normally 1 bar, there usually is a two-phase field of solid and liquid from pure A to B. However, congruent melting does take place either at a minimum or maximum. The question one may ask is under what thermodynamic conditions does this kind of melting take place? Why does it sometimes occur as a maximum and other times as a minimum? What does a rather flat liquidus (or a solidus) curve mean thermodynamically? In other words, there is a point of inflection in the liquidus (or solidus) curve. Since we have presented a lecture on this topic at the symposium on Computational Methods in Materials Education at the 2003 Annual TMS Meeting, San Diego, CA, and a manuscript summarizing our presentation has been published in the December 2003 issue of JOM-e: a Web-Only Supplement to JOM,[2] I will only make a brief summary here. Readers are referred to this article for a more thorough presentation.

Figure 1 shows a phase diagram for the Mo-W system taken from Rudy.[3] It is a simple diagram indeed. Both Mo and W exhibit the bcc structure and are completely soluble in each other both in the liquid and solid states. The solidus curve was measured experimentally but the liquidus curve was estimated. The melting temperature increases monotonically from 2896 K for Mo to 3695 K for W.[4] This is not surprising since the difference in the lattice parameters of Mo and W is

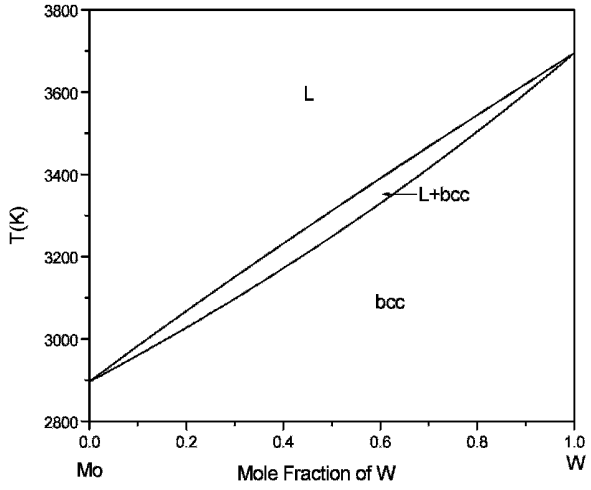

Fig. 1—A calculated phase diagram of Mo-W assuming ideal behavior for both the solid and liquid phases. The Gibbs energies of fusion for Mo and W are $\Delta_{fus} G(\text{Mo}) = 32{,}500 - 11.3T$ J mol^{-1} and $\Delta_{fus} G(\text{W}) = 38{,}429 - 10.4T$ J mol^{-1}.

within 0.5 pct.[5] Within the uncertainties of the measured solidus and estimated liquidus curves, the calculated solid/liquid phase boundaries or the solidus/liquidus curves shown in Figure 1, assuming ideal solution behavior for both the solid and liquid phases, are in accord with the measured and estimated values. In other words, the regular solution parameters L_0 (L) and L_0 (bcc) are 0. The enthalpies and entropies of fusion of Mo and W given in the Figure 1 caption were obtained from the Gibbs energies of fusion of Mo and W given by Dinsdale[4] assuming the difference between the specific heats of the liquid and those of the solid to be zero. Let me now introduce the Redlich–Kister[6] equation since it is the almost universally accepted expression in the materials thermodynamic community for describing the thermodynamic behavior of substitutional alloys. This equation is

$$G^E = x_A x_B \sum_{j=0}^{n} L_j (x_A - x_B)^j \qquad [1]$$

where G^E is the excess Gibbs energy, x_A and x_B the mole fractions of the component elements, and L_j's are parameters. When j is 0, we have the regular solution parameter L_0. The parameter L_j is often expressed as a linear function of T when T is higher than the Debye temperature. It is noteworthy to point out that one should avoid using more than three parameters at a constant temperature to represent the solution behavior using this type of representation. Otherwise, artifacts could be introduced.

A cigar-shaped liquidus-solidus curve results when the values of the L_0 (S) and L_0 (L) are comparable and when the melting points and entropies of fusion of the component elements remain essentially the same. When they are both positive, the width of the liquidus-solidus increases when compared with that for the case when L_0 (S) = L_0 (S) = 0. On the other hand, when they are negative, the width decreases. Chang and Oates have presented these results elsewhere.[2] Other examples of phase diagrams with cigar-shaped liquidus/solidus curves other than Mo-W are the Ag-Au, Ag-Pd, Cd-Mg, Co-Ni,[7] and Ge-Si[8] systems.

I will next use the Mo-W binary as a reference and show the effect of changing the regular solution parameters of the liquid and solid phases on the resulting phase diagrams. In order to avoid causing any possible confusion, I will designate these binaries as A-B but take the enthalpies and entropies of fusion for A and B to be the same as those of Mo and W, respectively. In each of these calculated diagrams, the cigar-shaped solidus-liquidus curves (when both solid and liquid phases behave ideally) is shown as a reference in order to appreciate the changes in the calculated diagrams when the solution parameters of the competing phases are changed. Figures 2(a) and (b) show the calculated phase diagram using L_0 (L) = 0 and L_0 (S) = -20 kJ mol^{-1} as well as L_0 (L) = 0 and L_0 (S) = 20 kJ mol^{-1}. In this article, I will always use the convention that the thermodynamic quantities are expressed in terms of 1 mole of atoms, *i.e.*, $A_{1-x_B}B_{x_B}$, unless stated otherwise. It is evident from Figure 2(a) that melting occurs at higher temperatures when compared with the cigar-shaped solidus-liquidus curves. Moreover, the maximum melting temperature occurs at a single composition, *i.e.*, the compositions of the liquid and the solid at the melting point are the same. This kind of melting is referred to as congruent melting. It is similar to the melting of a pure component A or B. On the other hand, other two-phase alloys melt over a range of temperature with corresponding composition changes. This resulting higher melting temperatures are reasonable since the solid phase becomes thermodynamically more stable with respect to the liquid phase. The results shown in Figure 2(b) are the reverse since the regular solution parameter of the solid phase is less exothermic than that of the liquid phase. A minimum congruent melting occurs in this case. In addition to exhibiting minimum congruent melting, something else also happens. The solid phase undergoes phase separation or the formation of a miscibility gap at lower temperatures. According to the regular solution model, the critical point for phase separation is T_c = L_0 (S)/2R = 1203 K, with T_c being the critical point and R the universal gas constant. Real examples with phase diagram shown in Figure 2(a) are Mo-Rh and Pb-Tl,[8] while those in Figure 2(b) are Co-Pd, Co-Rh, and Cr-Mo.[8]

Figure 2(c) shows two calculated phase diagrams. The solid lines are calculated using L_0 (L) = 0 and L_0 (S) = 50 kJ mol^{-1}, yielding a eutectic phase diagram. Let us compare the values of L_0 (S) used here with that used in calculating the phase diagram (Figure 2(b)) since the liquid is ideal in both cases. The thermodynamic parameters indicate that the liquid in this case is much more stable than the solid phase. This condition favors the liquid existing to lower temperatures. A familiar real binary exhibiting this type of diagram is Ag-Cu.[8] Both of these elements exhibit the fcc structure and form a eutectic phase diagram. When we next increase the value of L_0 (L) from 0 to -50 kJ mol^{-1} and keep that of L_0 (S) = 50 kJ mol^{-1}, the eutectic point goes to a much lower temperature, as shown also in Figure 2(c). This is due to the fact that liquid becomes even more stable than the solid phase. Binary alloys exhibiting such a feature tend to form glass when solidified from the melt at or near the eutectic composition. Figure 2(d) shows a calculated diagram when the liquid becomes highly endothermic with a value of L_0 (L) = 64 kJ mol^{-1}, keeping that of L_0 (S) = 50 kJ mol^{-1}. This calculated diagram is referred to as a monotectic phase diagram. In other words, a liquid separates into two phases just as a solid phase does when it is highly endothermic. We note from this phase diagram that the shape of the solidus curve is rather flat at the nearly equal atomic composition. The entire solidus curve shows a point of inflection. This type of phase boundary, whether it is solid or liquid, is anticipated to undergo phase separation at slightly lower temperatures. This is indeed the case for the phase diagram shown in Figure 2(d). One can find many real examples in the literature such as the Fe-rich liquidus in Fe-S[9] and the Cr-rich bcc phase solidus in Cr-Ni.[10]

It is noteworthy to point out that the pioneering work in relating the characteristic features of binary phase diagrams in terms of the relative thermodynamic stabilities of the phases involved was done nearly a century ago by Van Laar.[11,12] More recently a number of other researchers have published similar diagrams to those presented here.[2,13–15] The only difference is that with the availability of commercial phase diagram calculation software nowadays such as the Lukas *et al*. program,[16] ThermoCalc,[17] MTDATA,[18] ChemSage,[19] FACT,[20] WinPhad,[21] PANDAT,[22,23] FactSage,[24] as well as other general software solving nonlinear problems, the students can readily calculate a large number of prototype phase diagrams without spending much

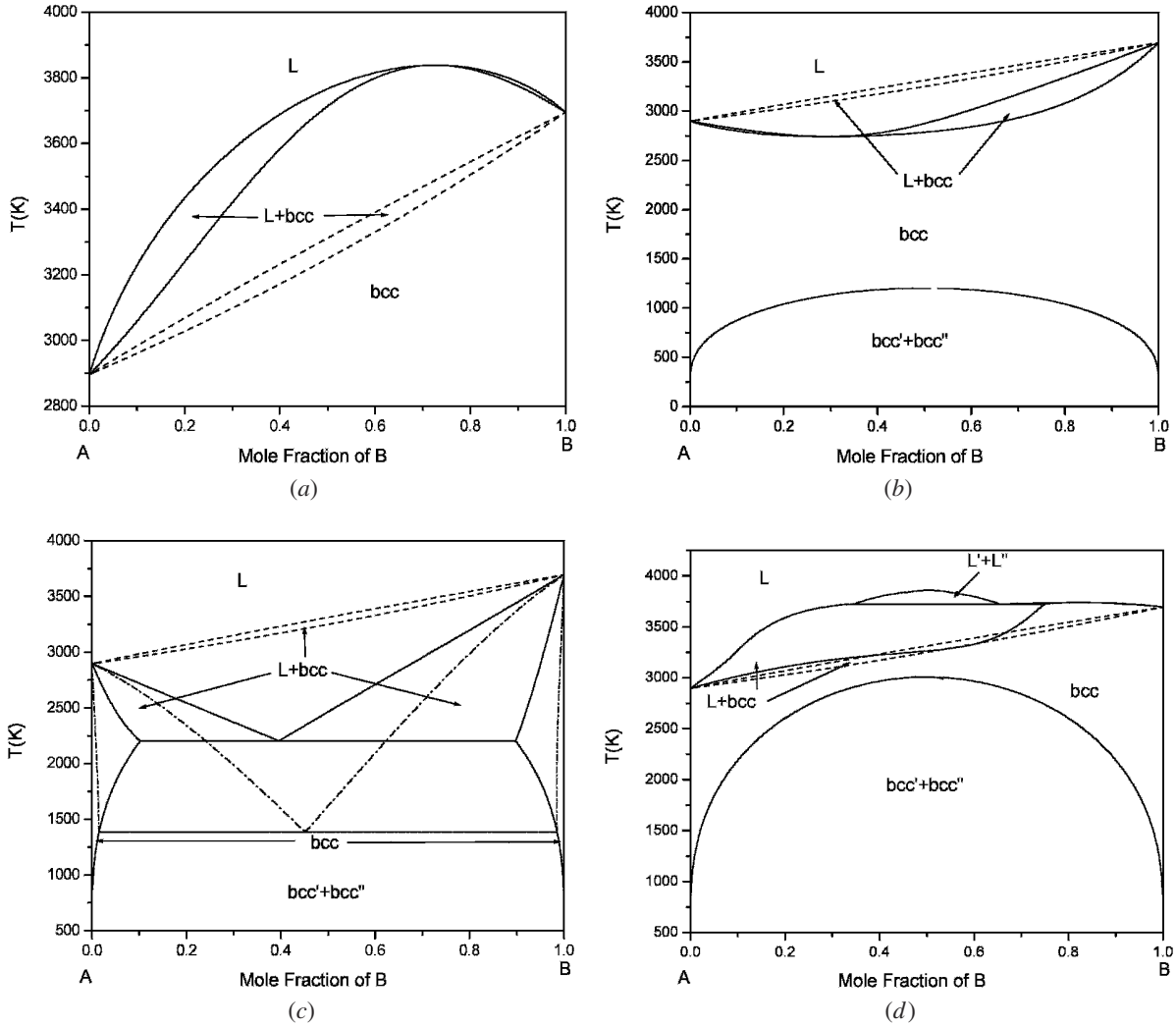

Fig. 2—(*a*) A calculated phase diagram of a hypothetical binary A-B using L_0 (L) = 0 J mol^{-1} and L_0 (S) = −20,000 J mol^{-1}. The Gibbs energies of fusion of A and B are taken to be the same as those of Mo and W. The dashed lines are the solidus-liquidus curves calculated when both solid and liquid phases behave ideally. (*b*) A calculated phase diagram of a hypothetical binary A-B using L_0 (L) = 0 J mol^{-1} and L_0 (S) = 20,000 J mol^{-1}. The Gibbs energies of fusion of A and B are taken to be the same as those of Mo and W. The dashed lines are the solidus-liquidus curves calculated when both solid and liquid phases behave ideally. (*c*) Calculated phase diagrams of a hypothetical binary A-B using two different sets of parameters: (1) L_0 (L) = 0 J mol^{-1} and L_0 (S) = 50,000 J mol^{-1} and (2) L_0 (L) = −50,000 J mol^{-1} and L_0 (S) = 50,000 J mol^{-1}. The Gibbs energies of fusion of A and B are taken to be the same as those of Mo and W. The dashed lines denote the solidus-liquidus curves calculated when both solid and liquid phases behave ideally. The solid lines denote the calculated phase diagram using the parameters from (1) and the dash-dot-dashed lines using the parameters from (2). (*d*) A calculated phase diagram of a hypothetical binary A-B using L_0 (L) = 64,000 J mol^{-1} and L_0 (S) = 50,000 J mol^{-1}. The Gibbs energies of fusion of A and B are taken to be the same as those of Mo and W. The dashed lines are the solidus-liquidus curves calculated when both solid and liquid phases behave ideally.

effort. They can then concentrate their effort on learning materials thermodynamics and phase diagrams.

I will next give only one ternary example that behaves contrary to intuition. This ternary A-B-C consists of two constituent binaries with a regular solution parameter L_0 (B,C) = L_0 (C,A) = −1 kJ mol^{-1} and a third one with parameter L_0 (A,B) = −40 kJ mol^{-1}. In other words, although the excess Gibbs energies of all three binary phases, let us take the phase to be liquid, are exothermic, the third binary liquid is significantly more exothermic. In our example, the regular solution parameter of the third binary phase is 40 times more exothermic than those of the other two binary phases. The question is what happens when we mix the three binary liquid phases together. Are they going to form a single homogeneous liquid phase or are they going to be phase separated? I think most people's initial reaction is that they would form a single homogeneous phase instead of phase separation. Figure 3(a) shows a calculated isothermal section at 500 K using the parameters given earlier. Contrary to our initial intuitive reaction, a ternary miscibility forms. This example was first, as far as I know, pointed out by Meijering[25,26] and Meijering and Hardy.[27] Figures 3(b) and (c) show two calculated isopleths: $A_{0.5}B_{0.5}$-C and $A_{0.4}C_{0.6}$-$B_{0.4}C_{0.6}$. These two isopleths differ in that the tie-lines for the diagram in Figure 3(b) lie within the *T vs* composition plane; thus, their tie-lines are shown in this figure but not for the diagram in Figure 3(c). Figure 3(b) can be considered

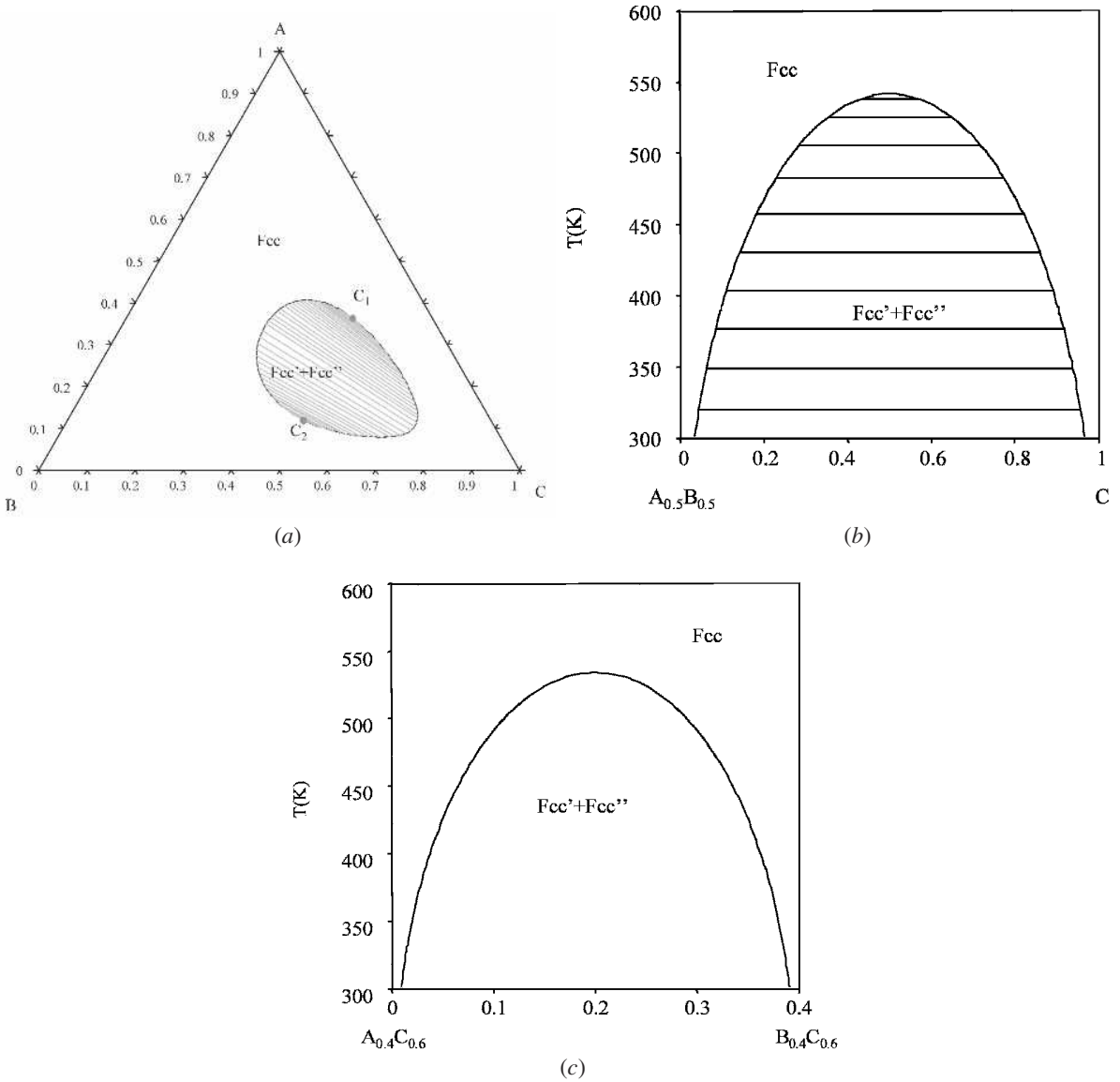

Fig. 3—(*a*) A calculated isothermal section of A-B-C at 500 K with L_0 (A-B, L) = −40 kJ mol^{-1} and L_0 (B-C, L) = L_0 (C-A, L) = −1 kJ mol^{-1}. The elements A, B, and C and the solutions are liquid at this temperature. The compositions are given in mole fractions. (*b*) A calculated isopleth of $A_{0.5}B_{0.5}$-C using the parameters given in the caption of (a). This isopleth can be considered as a quasi-binary system. The compositions are given in mole fraction of C. (*c*) A calculated isopleth of $A_{0.4}C_{0.6}$-$B_{0.4}C_{0.6}$ using the parameters given in the caption of (a). The tie-lines are not in the plane of the T-composition section. The compositions are given in mole fractions of B.

as a true binary (or pseudo- or quasi-binary) phase diagram. This is a rare case since the phase behaves like a regular solution. Had we drawn the T-composition sections between $A_{1-x}B_x$ and C, we would not have quasi-binaries except for the one shown in Figure 2(b) when $x = 0.5$. In reality, most of the T-composition sections in ternaries are not quasi-binaries but are isopleths. In other words, the tie-lines do not lie in the T-composition plane. One real example exhibiting this type of behavior is ternary (Cu,Pb,Sn) liquid.[28] The constituent binary liquid alloys do not behave regularly. However, I estimated the regular solution parameters for these three binary liquids using the thermodynamic data given by Hultgren *et al.*[7] They are L_0 (Cu,Pb) = 20.7 kJ mol^{-1}, L_0 (Pb,Sn) = 9.8 kJ mol^{-1}, and L_0 (Cu,Sn) = −20.7 kJ mol^{-1}, respectively. In other words, the regular solution parameter for one of the three binary liquids, *i.e.*, (Cu,Sn), is much more negative than those of the other two.

B. *Phase Diagrams of High-Order Alloy Systems*

Visualization of binary T-composition diagrams at constant pressure, *p*, as well as ternary isotherms, also at constant *p*, is straightforward since they are two-dimensional representations of temperature-composition and composition-composition relationships. My experience in teaching ternary-phase diagrams leads me to believe that most of us can readily

learn to analyze three-dimensional representations when the information on one of the dimensions is projected onto a two-dimensional plane such as the liquidus projection of a ternary system. Most of us metallurgists learn to use these diagrams to estimate phase formation sequences during nonequilibrium solidification of an alloy in a rather simple ternary system. However, the task becomes much more challenging when we carry out such an analysis for a quaternary, not to mention a higher order, system. Yet, most real alloys consist of at least four component elements. On the other hand, I have recently found that rapid advancement made in commercial software to calculate multicomponent phase diagrams and the availability of reliable thermodynamic databases has allowed me to make some progress in teaching quaternary phase diagrams in this direction. I here give one example to illustrate the use of a computer graphics presentation to convey the information given on a liquidus projection of the Al-rich Al-Cu-Mg-Si system to the students.

Figure 4 shows the calculated liquidus projections of Al-Cu-Si, Al-Mg-Si, and Al-Cu-Mg, three constituent Al ternaries of Al-Cu-Mg-Si. The compositions are given in weight fractions. The symbols θ, β, S, T, and W denote the intermetallic phases Al_2Cu, Al_3Mg_2, Al_2CuMg, $(Al,Cu)_{49}Mg_{32}$, and $Al_7Cu_3Mg_6$ respectively. Moreover, the liquid compositions of the monovariant equilibrium, L + (Al) + Mg_2Si, in the vicinity of e_3, the binary Al-Mg eutectic nearly coincide with the compositional axis for the Al-Mg binary. The liquid compositions of this monovariant equilibrium in Al-Mg-Si are shown in the inset of Figure 4, allowing us to comprehend the equilibria in the compositional vicinity of I_4 and I_5 (two ternary eutectics in Al-Mg-Si and Al-Cu-Si, respectively). Explanation of these symbols I_4 and I_5 is given in a later paragraph. Phase diagram calculations of these ternaries as well as the quaternary Al-Cu-Mg-Si system were carried out using the software PANDAT[22] and the thermodynamic database PanAluminum.[29] The three binary Al-rich

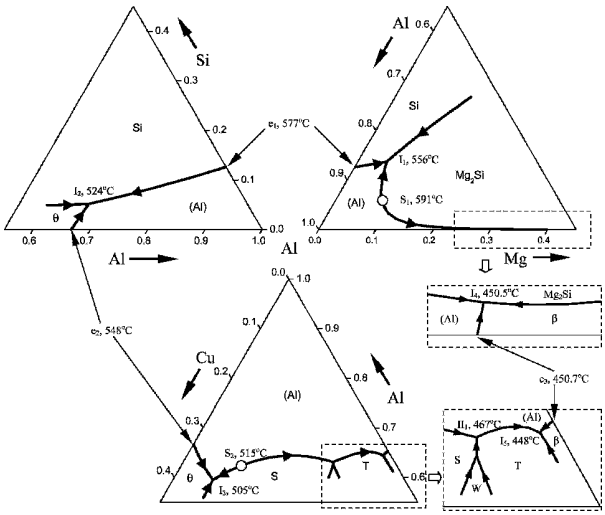

Fig. 4—Calculated liquidus projections of three constituent Al ternaries of Al-Cu-Mg-Si in the Al-rich corner using PANDAT[22] and PanAluminum.[29] The symbols θ, β, S, T, and W denote the intermetallic phases Al_2Cu, Al_3Mg_2, Al_2CuMg, $(Al,Cu)_{49}Mg_{32}$, and $Al_7Cu_3Mg_6$, respectively. The compositions are given in weight fractions.

eutectics with their temperatures are shown in Figure 4 as e_1 for Al-Si, e_2 for Al-Cu, and e_3 for Al-Mg, respectively. As shown in these diagrams, there are five type-I four-phase invariant and two type-II four-phase invariant equilibria. However, only the II_1 invariant at 467 °C is presented in the inset in Figure 4 (the lower one). The temperatures of these invariant equilibria are also given in this figure. The two saddle points, L + (Al) + S and L + (Al) + Mg_2Si, are denoted as s_1 (591 °C) and s_2 (515 °C), respectively.

Figure 5(a) shows three compositional coordinates in the *x*, *y*, and *z* directions. The compositions of the liquid for the three binary eutectics, taken from Figure 4, are replotted on these axes and denoted as e_1 for the (Al) + Si eutectic, e_2 for the (Al) + θ eutectic, and e_3 for the (Al) + β eutectic. The symbols θ and β have been defined previously. The compositions of the liquid for the monovariant three-phase equilibria, L + solid$_1$ + solid$_2$, in these three Al ternaries, emanating from their constituent binary eutectics as well as from the two saddle points, s_1 (L + (Al) + $MgSi_2$) and s_2 (L + (Al) + S) in the ternary regime, are also shown in these ternaries. When three such monovariant equilibria intersect with each other, a four-phase invariant forms. Figure 5(a) shows the existence of five type-I four-phase equilibria, *i.e.*, ternary eutectics, and two type-II four-phase equilibria (also Figure 4), but only II_1 is identified, as noted previously. Adopting the notations of Rhine[30] and following the format of Chang and co-workers,[28,31–33] these invariants are denoted as I_1, I_2, *etc.* to I_5 and II_1, with the subscript 1 indicating the highest temperature and 5 the lowest. There are two saddle points, one in Al-Cu-Mg and the other in Al-Mg-Si. For the I_4 and I_5 invariant equilibria, see the inserts in Figure 4 for details. In addition, the primary phases of solidification are also given in this figure. It then becomes abundantly clear, for instance, that the liquid compositions represented by the line from e_1 to I_2 are in equilibrium with Si and (Al) and those from s_2 to I_3 in equilibrium with (Al) and S. The symbols S and T have been defined previously.

The four-phase invariants in the three ternaries enter into the four-component Al-Cu-Mg-Si space as monovariant equilibria, in a manner similar to the way binary invariants enter into the two-dimensional plane for ternaries. The compositions of the liquid for the monovariant four-phase equilibria, L + solid$_1$ + solid$_2$ + solid$_3$, are shown in Figure 5(b) as red lines to differentiate them from those monovariants for the ternaries. There are a total of 6 five-phase invariants denoted as $I_1(q)$, $I_2(q)$, $I_3(q)$, $II_1(q)$, $II_2(q)$, and $II_3(q)$ and 3 saddle points $s_1(q)$, $s_2(q)$, and $s_3(q)$, with the symbol (q) indicating that they are for the quaternary system. The calculated compositions of the phases at the invariant equilibria are given in Table I and the calculated reaction sequences for the invariant equilibria are given in Figure 5(c). The four- and five-phase equilibria given in Figure 5(b) are enclosed with boxes by full lines, as shown in Figure 5(c). On the other hand, the four-phase equilibria, not given in Figure 5(b) but needed to complete the invariant reactions in Figure 3(c), are enclosed with boxes by dashed lines. It is worthwhile noting that one additional primary phase of solidification in the center part of this figure is the quaternary intermetallic phase $Al_5Cu_2Mg_8Si_6$ denoted as Q. Again, we can read from this figure (certainly with the help of the reaction sequences given in Figure 5(c)) the solid phases in equilibrium with the liquid along the monovariant equilibria. For instance,

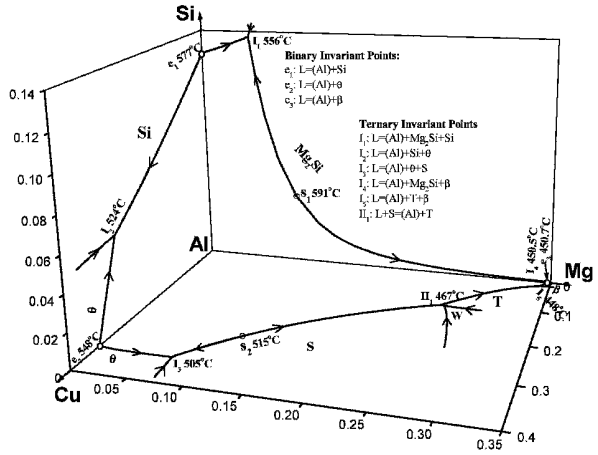

(*a*)

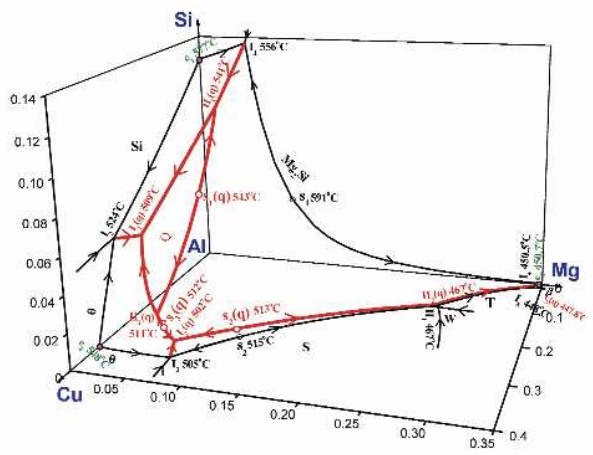

(*b*)

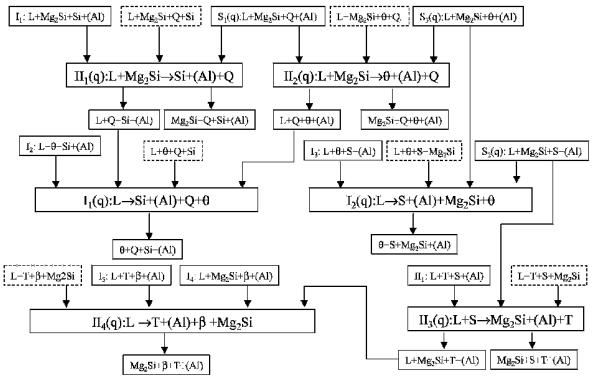

(*c*)

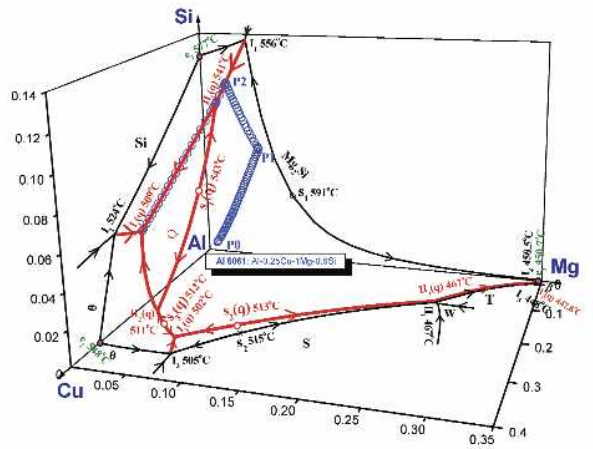

(*d*)

Fig. 5—(*a*) Calculated liquidus projections of Al-Cu-Mg-Si in the Al corner showing the liquid compositions of the binary eutectics e_1, e_2, and e_3, as well as those of the monovariant equilibria emanating from binaries to the three ternary regions including those at the four-phase invariants. The primary phases of solidification in the respective ternaries are also shown. The symbols θ, β, S, T, and W denote the intermetallic phases Al_2Cu, Al_3Mg_2, Al_2CuMg, $(Al,Cu)_{49}Mg_{32}$, and $Al_7Cu_3Mg_6$, respectively. The compositions are given in weight fractions. (*b*) Calculated liquidus projections of Al-Cu-Mg-Si in the Al corner showing the liquid compositions of the binary invariant reactions, e_1, e_2, and e_3, and the ternary invariant reactions, I_1, I_2, *etc.* to I_5 and III, as well as those of the monovariant four-phase equilibria emanating from the ternaries to the quaternary space including those at the five-phase invariants. The additional primary phase of solidification in this quaternary is the quaternary phase Q. All the liquid composition curves and the primary phase of solidification are presented in red color. The symbols $I_1(q)$, $I(q)_2$, *etc.* and $II_1(q)$, $II_2(q)$, *etc.* refer to the types of invariants for the quaternary Al-Cu-Mg-Si system. The symbols θ, β, S, T, W, and Q denote the intermetallic phases Al_2Cu, Al_3Mg_2, Al_2CuMg, $(Al,Cu)_{49}Mg_{32}$, $Al_7Cu_3Mg_6$, and $Al_5Cu_2Mg_2Si_6$, respectively. The compositions are given in weight fractions. (*c*) Reaction sequences for the invariant equilibria shown in the liquidus projections of Al-Cu-Mg-Si (b). The four-phase invariant equilibria enclosed with dash line boxes are not shown in (b). (*d*) Calculated path of solidification of 6061 Al alloy, Al-0.25Cu-1Mg-0.6Si (in wt pct) according to the Scheil solidification condition shown on the liquidus surface of the quaternary Al-Cu-Mg-Si system. At P0 (651 °C), (Al) forms, or L + (Al) coexist; at P1 (579 °C), Mg_2Si forms, or L + (Al) + Mg_2Si coexist; at P2 (546 °C), Si forms or L + (Al) + Mg_2Si + Si coexist; at II1(q) (541 °C), L + Mg_2Si = (Al) + Si + Q; from II1 → I1(q) (541 °C to 509 °C), L + (Al) + Si + Q coexist; and at I1(q) (509 °C), L = (Al) + Si + Q + θ. The freezing temperature range is 142 °C. The symbols θ, β, S, T, W, and Q denote the intermetallic phases Al_2Cu, Al_3Mg_2, Al_2CuMg, $(Al,Cu)_{49}Mg_{32}$, $Al_7Cu_3Mg_6$, and $Al_5Cu_2Mg_2Si_6$, respectively. The compositions are given in weight fractions.

the liquid with compositions from $II_1(q)$ to $I_1(q)$ is in equilibrium with (Al), Si, and Q, that from II_1 to $s_1(q)$ with (Al), Q, and Mg_2Si, and that from $s_3(q)$ to $I_2(q)$ with (Al), θ, and Mg_2Si, respectively.

Let us suppose that we do not have the reaction sequences given in Figure 5(c), how can we deduce the equilibrium reactions involved for any of the five-phase invariants presented in the liquidus projection, *i.e.*, Figure 5(b). I will first take a type-I five-phase invariant equilibrium such as $I_1(q)$ as an example. Since it is a eutectic reaction, L = (Al) + θ + (Si) + Q, there must exist 4 four-phase equilibria above the invariant temperature and 1 four-solid-phase equilibrium below.[30] Three of the four above the invariant temperature presented in the liquidus projection are L + Q + Si + (Al), L + θ + Si + (Al), and L + Q + θ + (Al). The fourth one must be L + θ + Q + Si. These four equilibria react with each other at the invariant temperature to form a type-I five-phase equilibrium. Immediately below this invariant temperature, the fifth four-phase

Table I. Calculated Compositions of the Phases at the Invariant Temperatures in the Al-Cu-Mg-Si System[33]*

Type of Invariants	Reaction	T (°C)	Phase	Composition, Mol Fraction			
				xAl	xCu	xMg	xSi
$II_1(q)$	$+MgL_2Si = (Al) + (Si) + Q$	541	L	0.799	0.039	0.053	0.109
			(Si)	0	0	0	1
			Mg2Si	0	0	0.667	0.333
			Q	0.238	0.095	0.381	0.286
			(Al)	0.974	0.006	0.009	0.011
$II_2(q)$	$L + Mg_2Si = (Al) + \theta + Q$	511	L	0.747	0.164	0.067	0.022
			(Al)	0.965	0.019	0.013	0.003
			Mg2Si	0	0	0.667	0.333
			Q	0.238	0.095	0.381	0.286
			θ	0.679	0.321	0	0
$I_1(q)$	$L = (Al) + \theta + (Si) + Q$	509	L	0.767	0.137	0.036	0.060
			(Si)	0	0	0	1
			Q	0.238	0.095	0.381	0.286
			(Al)	0.967	0.019	0.005	0.009
			θ	0.679	0.321	0	0
$I_2(q)$	$L = (Al) + \theta + Mg_2Si + S$	502	L	0.725	0.171	0.096	0.008
			Mg_2Si	0	0	0.667	0.333
			(Al)	0.960	0.018	0.021	0.001
			S	0.5	0.25	0.25	0
			θ	0.678	0.322	0	0
$II_3(q)$	$L + S = (Al) + Mg_2Si + T$	467	L	0.651	0.047	0.301	0.001
			Mg_2Si	0	0	0.667	0.333
			(Al)	0.881	0.003	0.116	0
			T	0.539	0.066	0.395	0
			S	0.5	0.25	0.25	0
$I_3(q)$	$L = (Al) + \beta + Mg_2Si + T$	448	L	0.625	0.005	0.369	0.001
			Mg_2Si	0	0	0.667	0.333
			T	0.567	0.038	0.395	0
			β	0.615	0	0.385	0
			(Al)	0.836	0.0004	0.1636	0

*The symbols θ, β, S, T, W, and Q denote the intermetallic phases Al_2Cu, Al_3Mg_2, Al_2CuMg, $(Al,Cu)_{49}Mg_{32}$, $Al_7Cu_3Mg_6$, and $Al_5Cu_2Mg_8Si_6$, respectively.

equilibrium with all solid phases, (Al), θ, (Si), and Q, forms. The reaction sequence for this type-I five-phase equilibrium is shown schematically subsequently. It is the same as that calculated thermodynamically, as shown in Figure 5(c). It is worth noting that the only four-phase equilibrium, $L + \theta + Q + Si$, given below is enclosed in a box with a dashed instead of

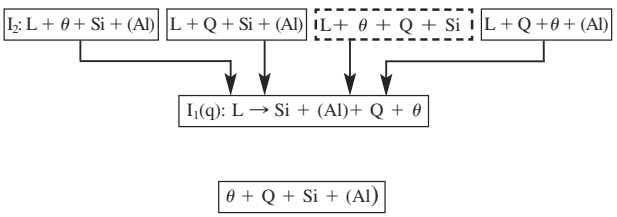

solid line to indicate that this four-phase equilibrium is not presented in Figure 5(b). This example may appear straightforward and obvious. However, I will next give another example, a type-II invariant reaction such as $II_1(q)$;[30] it is a bit less obvious when compared with a type-I invariant reaction. For such a reaction, there exist 3 four-phase equilibria about the invariant temperature and 2 below.[30] Two of the 3 four-phase equilibria, as presented in Figure 5(b), are $L + Mg_2Si + Si + (Al)$, represented by the monovariant line from I_1 to $II_1(q)$, and $L + Mg_2Si + Q + (Al)$, represented by the monovariant line from $s_1(q)$ to $II_1(q)$. The 2 four-phase invariant equilibria below the invariant temperature are $L + Q + Si + (Al)$, represented by the monovariant line from $II_1(q)$ to $I_1(q)$, and $Mg_2Si + Q + Si + (Al)$, all solid phases. The existence of the $L + Q + Si + (Al)$ four-phase equilibrium below the five-phase invariant temperature leads to the conclusion that Mg_2Si must be the high-temperature phase. Accordingly, this type II reaction is deduced to be $L + Mg_2Si = Q + Si + (Al)$. Since a five-phase equilibrium can be represented by a tie hexahedron consisting of five tie tetrahedrons, it is possible to deduce that the third four-phase equilibrium is $L + Mg_2Si + Q + Si$, as shown subsequently. It is the same as that calculated

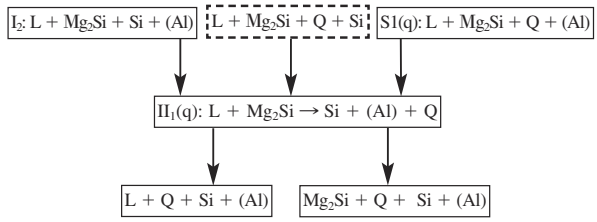

thermodynamically, as shown in Figure 5(c). A simpler approach is to note that each of the five phases only appear four times in the 5 four-phase equilibria. In other words, the

phases L and Mg_2Si must be in equilibrium with Q and Si at temperatures higher than the invariant temperature.

With classes in the past, I used to discuss solidification paths only for binary and ternary alloys. However, with the availability of computer calculated multicomponent higher order phase diagrams, I can now present the solidification paths of higher order alloys. In the following, I will do so for a 6061 alloy, Al-0.25Cu-1Mg-0.6Si (in wt pct), according to the Scheil solidification condition again using the software PANDAT. Since the major elements in 6061 alloys are Al, Cu, Mg, and Si, neglecting the other minor elements makes little difference as far as teaching is concerned. The calculated solidification path is plotted in Figure 5(d) from P0 → P1 → P2 → $II_1(q)$ → $I_1(q)$ as a circled line. Solidification of (Al) begins when the temperature drops to the Al-Cu-Mg-Si liquidus surface at 651 °C, P0 (Figure 5(d)). The temperature of the liquid in equilibrium with (Al) decreases continuously from P0 to P1. Once the liquid composition reaches P1 on the L + (Al) + Mg_2Si three-phase surface, the Mg_2Si phase starts to solidify from the melt and the composition of L follows the curve P1-P2. When the composition of L reaches the point P2 (546 °C) on the monovariant four-phase equilibrium, L + (Al) + Mg_2Si + Si, the composition of L changes its direction and then follows the monovariant line P2-$II_1(q)$. At this point, the quaternary phase Q starts to form from the liquid *via* a five-phase invariant reaction, $II_1(q)$: L + Mg_2Si = (Al) + Si + Q (Figure 5(d) and Table I). With further decreases in temperature, the remaining L continues solidifying along the four-phase L + (Al) + Si + Q monovariant line $II_1(q)$-$I_1(q)$. At the five-phase invariant $I_1(q)$ (509 °C, also Figure 5(d) and Table I), solidification ends at the quaternary eutectic invariant, L = (Al) + Si + Q + θ, similar to what happens in binary and ternary liquid alloys. The only difference is that this quaternary liquid alloy transforms isothermally to four solids instead of three for a ternary and two for a binary alloy. With a computer-generated graphical presentation in a formal class, I can first show Figure 4 and give the students time to appreciate the liquidus projections in the three Al-ternaries and then show essentially the same information on Figure 5(a). By this time, the students are quite familiar with this information and I can then show (in red color) the extension of the four-phase invariant equilibria (in the ternaries) into the quaternary space as monovariant equilibria. When three of these monovariant four-phase equilibria (plus another four-phase equilibrium, not shown in this figure) intersect with each other, a five-phase invariant equilibrium forms, as discussed earlier.

Composition changes in the liquid of the 6061 alloy during solidification under the Scheil condition cannot be obtained from Figure 5(d). However, these changes can be calculated readily using PANDAT and PanAluminum and presented in Figure 6 in terms of temperature as a function of the liquid compositions of Cu, Mg, and Si, respectively. Although the initial Cu composition in 6061 alloy is only 0.25 wt pct, that in the liquid during the final stage of solidification could be higher than 25 wt pct, an increase of two orders of magnitude. This drastic composition difference is a result of microsegregation during the course of solidification. The fractions of each phase formed during solidification are shown in Figure 7. The fractions for Si, Q, and θ are very small, being less than 0.2 vol pct and are difficult to detect experimentally in the cast alloys unless extreme care is taken.

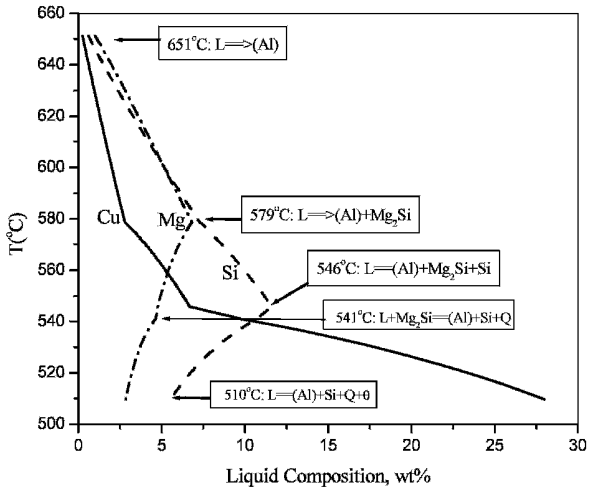

Fig. 6—Liquid compositions as a function of temperature during the solidification of the 6061 Al alloy, Al-0.25Cu-1Mg-0.6Si (in wt pct).

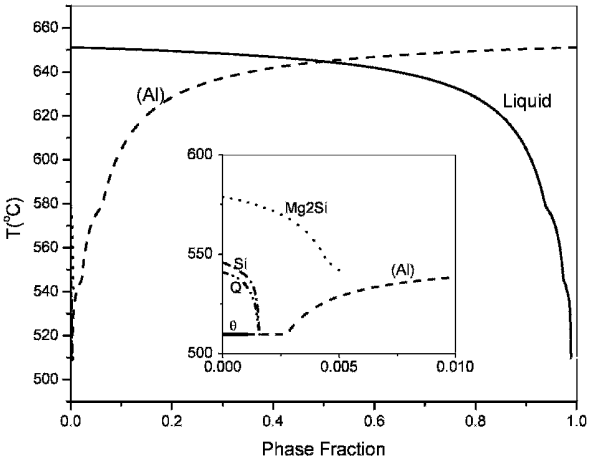

Fig. 7—Calculated phase fractions of the 6061 alloy, Al-0.25Cu-1Mg-0.6Si, as a function of temperature under the Scheil solidification condition; the insert shows an enlarged view for the phase fractions below 0.01. The phase fractions are given in volume percent.

The preceding analysis does not tell us what happens when an alloy solidifies under global equilibrium condition, *i.e.*, when it is cooled infinitely slowly from the melt. Even though an alloy rarely solidifies under these conditions, it is helpful to know the equilibrium phases formed when the temperature is decreased. Such information can be readily obtained from a calculated isopleth, as shown in Figure 8. It is a T *vs* Cu composition section of Al-Cu-Mg-Si, or an isopleth, with the compositions of Mg and Si kept constant at 1 and 0.6 wt pct, respectively. It is clear from Figure 8 that global equilibrium solidification of the 6061 alloy, Al-0.25Cu-1Mg-0.6Si, begins also at 651 °C and ends at 600 °C. This freezing range is 51 °C, only one-third of the freezing range of 142 °C when solidification takes place under the Scheil condition. The Scheil solidification condition is closer to actual casting conditions for substitutional alloys. While it is possible to estimate the

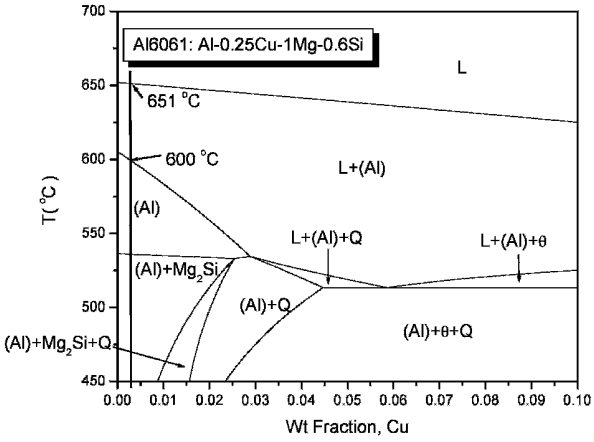

Fig. 8—A calculated isopleth in terms of T *vs* the composition of Cu with the compositions of Mg and Si held constant at 1 and 0.6 wt pct, respectively. The dark vertical line highlights the alloy composition, Al-0.25Cu-1Mg-0.6Si. The abscissa is the composition of Cu in weight fractions. When the composition of Cu is 0, the weight fraction of Al is 0.984.

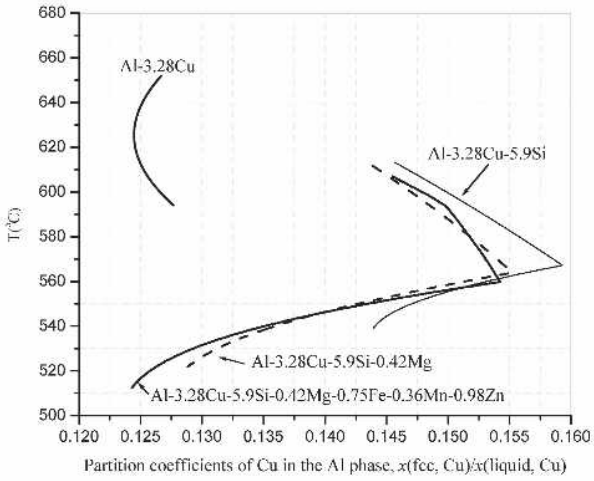

Fig. 9—Calculated partition coefficients of Cu in the (Al) phase for a binary Al-3.28Cu alloy, a ternary Al-3.28Cu-5.9Si alloy, a quaternary Al-3.28Cu-5.9Si-0.42Mg alloy, and a seven-component B-319 alloy. The composition of B-319 is given in the figure. All compositions of these alloys are given in weight percent.

phase formation sequence when binary and ternary alloys solidify from their phase diagrams, it is very difficult, if not impossible, to do so for a multicomponent alloy from an isopleth such as that for 6061 from Figure 8. However, such information can be readily obtained from a curve similar to that shown in Figure 7 calculated using a thermodynamic database such as PanAluminum.

I would like to add one more comment concerning partition coefficients. In multicomponent alloys, these have usually been assumed to be constant in the past when computer calculation of phase diagram was not the norm. These coefficients are the ratios of the compositions of solid and liquid in equilibrium with each other at a specified temperature with the pressure being held constant, normally 1 bar. While this assumption is not serious for binary alloys, it could cause serious errors for multicomponent alloys. As shown in Figure 9, while the partition coefficients of Cu in (Al) in binary Al-3.28Cu do not change appreciably with temperature, those in ternary Al-3.28Cu-5.9Si, quaternary Al-3.28Cu-5.9Si-0.42Mg, and a multicomponent commercial B319 alloy Al-3.28Cu-5.9Si-0.42Mg-0.75Fe-0.36Mn-0.98Zn do change appreciably with temperatures.[33]

III. APPLICATIONS

In this section, I give five examples to illustrate the use of computational thermodynamics including phase diagram calculation for materials research/development and manufacturing with four focusing on the former and one on the latter, *i.e.*, manufacturing. Out of the four examples for materials research/development, two are for structural materials, one for functional materials, and the other one could be either. The first example is concerned with a rapid and efficient approach for generating a thermodynamic description or database for a quaternary Mo-Si-B-Ti system for identifying potential alloy compositions that may exhibit desirable microstructures for high-temperature applications. The second one is to use a thermodynamically calculated isopleth to identify optimum compositions of Ti addition in order to improve the glass-forming ability (GFA) of a known glass-forming quaternary (Al,Cu,Ni,Zr) alloy. Since bulk metallic glasses represent a new class of materials with great potentials as either structural or functional materials, there is an urgent need to use a scientifically sound approach to identify potential alloys for glass formation instead of the traditional empirical trial and error experimentation. In a recent review article, Loffer[34] made the following statement: "... the search for new bulk metallic glass compositions is somewhat a 'trial-and-error' method, involving in many cases the production of hundreds to thousands of different alloy compositions." The third example is the use of computational thermodynamics for selecting appropriate filler metals to minimize cracks in welding multicomponent aluminum alloys. The fourth example is to use computational thermodynamics to identify potential binary alloys with a tendency to form glass or amorphous alloy thin films *via* a rapid quenching process such as sputtering deposition. The metallic alloys in the amorphous state can be readily oxidized to form a smooth surface for potential applications as the tunnel barriers in magnetic tunnel junctions (MTJs). These junctions are being considered as sensitive magnetic sensors and nonvolatile storage cells in magnetic memories. In the last case, I will present one example to show that computational thermodynamics can even replace experimentation to certify alloys for commercialization such as Ti6Al4V. The numerals 6 and 4 represent the wt pct of Al and V in these alloys, respectively.

A. *Materials Research/Development and Manufacturing: (1) Rapid Development of a Thermodynamic Description of Mo-Si-B-Ti Using a Computational/Experimental Approach Serving as a Road Map for Developing Materials beyond Nickel-Based Superalloys*

The limit imposed on improving the efficiency of turbine engines for high-temperature applications such as aircraft

engines is the lack of suitable materials since the currently used nickel-based superalloy in these engines is already subjected to a temperature as high as 90 pct of its melting point. Facing this challenge, the materials community has been motivated to pursue research on very high-temperature alloys in order to develop new materials beyond the nickel-based superalloys. In addition to high melting points, these materials must exhibit resistance to oxidation, deformation, creep, fracture, *etc*. at all temperatures. Moreover, since these materials are being developed for aerospace applications, their densities must be low. Above all of these technical challenges, the cost of producing these materials has to be economically competitive. A review of the elements in the periodic table suggests that the two obvious elemental candidates are Nb and Mo. While refractory metals such as Nb and Mo have very high melting points and relatively low densities, they lack oxidation resistance. One way to improve their oxidation resistance is to have a multiphase structure material consisting of a ductile metallic phase in equilibrium with one or more oxidation-resistant and yet strong metallic silicides. It is well known that metal silicides form protective silica glass scales at very high temperatures. Although Nb-silicide and Mo-silicide composites showed early promise, additional alloying elements are needed so as to develop balanced overall properties in terms of high-temperature strength, low-temperature damage tolerance, oxidation resistance, and creep strength. About 5 years ago, Y. Yang began to do her doctoral thesis research on the phase equilibria of quaternary Mo-Si-B-Ti system[35–39] at the University of Wisconsin (Madison, WI). Here, I will first introduce this subject briefly and then present the strategy used to rapidly develop a thermodynamic description of this quaternary system using a minimum amount of experimentation. On the basis of the calculated phase diagrams of this quaternary system, potentially interesting multiphase equilibria or composites have been identified and studied.

Figure 10 shows a 1600 °C isotherm of Mo-Si-B in the Mo-rich corner of this ternary system.[40,41] The intermediate phases in the Mo-rich corner are Mo_3Si(A15) and Mo_5Si_3(T1, tI32, $D8_m$) in Mo-Si and Mo_2B and MoB in Mo-B. There is additionally a ternary phase Mo_5SiB_2 (T2, tI32, $D8_1$). It is worth noting that even though both T1 and T2 have the same Pearson symbol, their structures differ. The prototype for T1 is W_5Si_3 and that for T2 is Cr_5B_3. In order to simplify the notations, I will in this article refer to Mo_3Si as A15, Mo_5Si_3 as T1($D8_m$), and Mo_5SiB_2 ($D8_1$) as T2. As shown in this figure, α-(Mo) is in equilibrium with the A15 and T2 phases, and the A15 phase is in turn also in equilibrium with the T2 and T1 phases. Berczik[42,43] found that the ductile α-(Mo) phase in the composites of α-(Mo) + A15 + T2 can greatly enhance the room-temperature and high-temperature toughness of the materials, but the side effect is degradation of the oxidation resistance. On the other hand, Meyer *et al*.[44] found that composites consisting of A15 + T1 + T2 exhibit good oxidation resistance but poor fracture toughness. This is due to the fact that all three component elements in the A15 + T1 + T2 composites are brittle. The most promising route is to develop multiphase equilibria consisting of a ductile α phase in equilibrium with T1 and T2. This is impossible with Mo-Si-B, but probable when we add other metallic elements. Instead of a three-phase equilibrium of α-(Mo) + A15 + T2, we may have one consisting of α-(Mo,M) + T1 + T2 with M an added metal. In the present article, I use α-(Mo,M) and bcc interchangeably to represent the solid solution of (Mo,M) with the bcc structure.

After reviewing the literature on the thermodynamics and phase equilibria of relevant binary and ternary systems, Ti was identified as such an added element based on the following rationale: (1) Ti can completely substitute Mo at high temperatures in the bcc structure in addition to having extensive solubilities in the T1 and A15 phases (the Mo-Ti-Si isotherm in Figure 11) and (2) substitution of Mo by Ti improves the strength of the metallic phase and the fracture toughness of intermetallic phases.[43,45] The quaternary Mo-Si-B-Ti system consists of four constituent ternaries and six binaries. In order

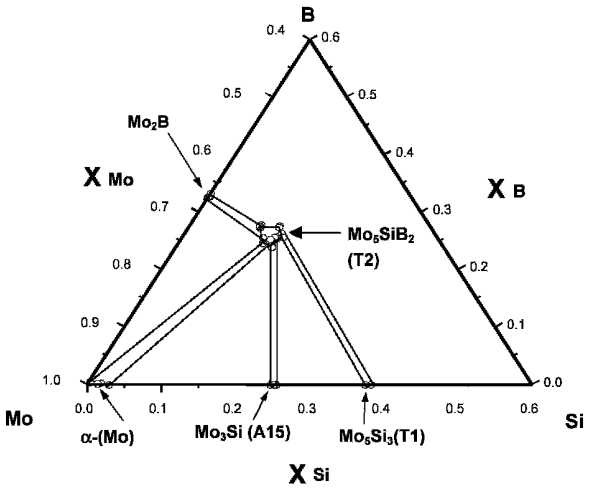

Fig. 10—A 1600 °C isotherm of Mo-Si-B in the Mo-rich corner of this ternary system. Compositions are given in mole fractions.

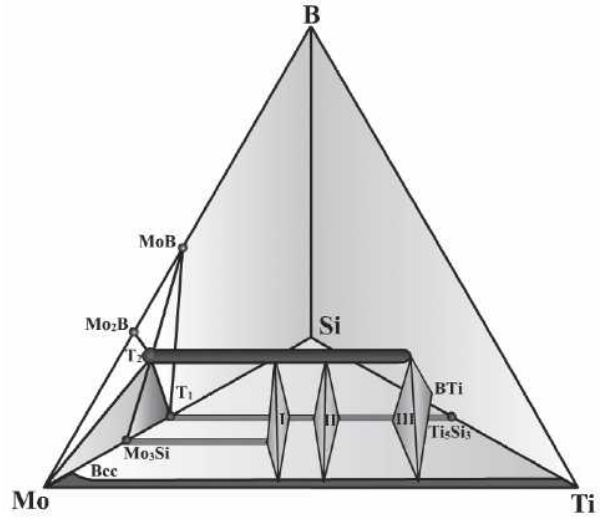

Fig. 11—A schematic isothermal tetrahedron that displays the phase relationship among the bcc, T2, A15, T1, and $D8_8$ phases on the metal-rich side of the Mo-Si-B-Ti quaternary system at 1600 °C. This diagram was drawn based on the results calculated from the preliminary thermodynamic modeling. The compositions are given in mole fractions.

to obtain a thermodynamic description for this quaternary, it is essential to first obtain descriptions for the constituent binaries and then the ternaries.[46] Thermodynamic descriptions were available for all six constituent binaries: Mo-Si,[47] Mo-B,[48] Mo-Ti,[49] Si-B,[50] Si-Ti,[51] and B-Ti.[52] However, it was found necessary to develop an improved description for Mo-B.[39] Of the four constituent ternaries, Mo-Si-B, Mo-Si-Ti, Mo-B-Ti, and Si-B-Ti, experimental data were not available in the literature for Mo-Si-Ti and Si-B-Ti. Yang[35,38] began to determine the phase equilibria of the two later ones experimentally and at the same time to develop descriptions for the other two ternaries, *i.e.*, Mo-Si-B[39] and Mo-B-Ti,[36] using experimental data available in the literature and the descriptions of the constituent binaries. She subsequently developed descriptions for the other two ternaries Mo-Si-Ti[35] and B-Si-Ti[38] when her experimental data became available. It has been a common practice to obtain a thermodynamic description of a quaternary system when such descriptions for the lower systems, *i.e.*, ternaries and binaries, are available by extrapolation without further experimentation.[46,53] In many cases, this approach works quite well. However, a closer examination of the phase equilibria of the constituent ternaries of Mo-Si-B-Ti indicates that T2 is likely to dissolve large amounts of Ti, thus extending its compositional stability into the quaternary space. In order to accommodate the multiphase equilibria involving T2 in the quaternary space, optimization of the thermodynamic model parameters of this phase was necessary. In the following, I will present the strategy used to rapidly establish a description of this quaternary using a minimum amount of experimental effort.

First, a preliminary thermodynamic description of the Mo-Si-B-Ti quaternary system was developed based on thermodynamic descriptions of the four constituent ternaries[35,36,38,39] as well as the thermodynamics of T2 in quaternary space. The focus of obtaining a thermodynamic description of Mo-Si-B-Ti was to model the thermodynamics of the T2 phase, which will be discussed in detail later. From this preliminary thermodynamic description, a 1600 °C isothermal tetrahedron of Mo-Si-B-Ti was calculated and a schematic representation of these equilibria in the α-(Mo,Ti)-rich region is shown in Figure 11, with α-(Mo, Ti) denoted by its crystal structure, bcc. As shown in this figure, there are four ternary isotherms. The left face of this tetrahedron gives the Mo-Si-B equilibria. The two three-phase equilibria of interest are bcc + A15 + T1 and A15 + T1 + T2. Phase equilibria of Mo-Si-Ti are shown on the bottom face of the tetrahedron. For the purposes of clarity, the phase equilibria for the remaining two ternaries are not shown since they are of no interest in describing the bcc-rich phase equilibria in this quaternary region. However, it is important to note that a corresponding A15 phase is not stable in the Si-Ti binary. Yet, there are extensive solubilities of the unstable Ti_3Si compound in the A15 phase. In a similar manner, the intermediate phase $T1(Ti_5Si_3)(D8_m)$ is not stable in binary Si-Ti but also has extensive solubilities in $T1(Mo_5Si_3)$. The stable Ti_5Si_3 compound in binary Ti-Si has the $D8_8$ structure. The $(Mo_5Si_3)(D8_8)$ compound, unstable in binary Mo-Si, also dissolves in $Ti_5Si_3(D8_8)$ to a large extent. It is worth noting that extensive homogeneity ranges in these metal silicides occur only along the direction parallel to binary Mo-Ti, meaning there are mutual substitutions of the Mo and Ti atoms on the metal sublattice. This evidence led to the obvious conclusion that the Ti atoms must also substitute for Mo on the metal sublattice of the T2 phase. This T2 phase can be represented by the formula $(Mo,Ti)_5SiB_2$.[36,37] The Gibbs energy of formation of Mo_5SiB_2, one of the two end members of the T2 solution phase, can be directly obtained from the thermodynamic description of Mo-Si-B.[39] An initial value of the Gibbs energy of the other end-member Ti_5SiB_2, unstable in Ti-Si-B, was estimated to be negative but less negative than that of the stable phases. In addition, ideal entropy of mixing was assumed between Mo and Ti on the metal sublattice in order to obtain a preliminary model for the T2 phase.

The phase equilibria of the five phases, bcc, A15, T1, T2, and $D8_8$, calculated from this preliminary thermodynamic description as presented previously, are shown schematically in Figure 11. These equilibria then served as a guide to make a minimum number of alloys for experimental determinations. The calculation shows the existence of 3 four-phase equilibria among these phases, bcc + A15 + T2 + T1 (I), bcc + T2 + T1 + $D8_8$ (II), and bcc + T2 + $D8_8$ + TiB (III), respectively. From the Mo-Si-B ternary to the four-phase equilibria (III), three "windows" exist and are separated by the two four-phase equilibria (I) and (II). In the left-hand window, there are 2 three-phase equilibria, bcc + T1 + T2 and A15 + T1 + T2. There is one three-phase equilibrium, bcc + T2 + T1, in the middle window, and another one, bcc + T2 + $D8_8$, in the third window. Based on this preliminary calculation, three alloy compositions, Mo-11Si-19B-10Ti, Mo-11Si-19B-20Ti, and Mo-11Si-19B-30Ti, were selected in such a way that the first alloy composition was located in the calculated three-phase bcc + A15 + T2 field, the second in bcc + T1 + T2, and the third in bcc + $D8_8$ + T2. All alloy compositions refer to atomic percentages. These three alloys were studied experimentally either to verify or to improve this preliminarily used thermodynamic description, and the experimental details were given elsewhere.[37] The experimental results showed the existence of bcc + A15 + T2 in the first sample consistent with the calculation. However, the experimental results also show the same three-phase equilibrium in the second sample, indicating the calculated four-phase equilibrium (I) should have been richer in Ti-Si-B. The three-phase equilibrium of bcc + T2 + $D8_8$ found in the third sample is consistent with the calculation. An improved description was developed using the newly obtained experimental results focusing primarily on the model parameters of the T2 phase. The newly calculated phase equilibria using the improved description were next used to identify six additional alloys for further experimental investigations. The compositions of the first two alloys were in the compositional vicinity of the newly calculated four-phase equilibrium (I), those of the next two were in that of the newly calculated four-phase equilibrium (II), and those of the last two were in that of the newly calculated four-phase equilibrium (III). These six alloy compositions were Mo-28.5Ti, Mo-32.5Ti, Mo-35Ti, Mo-37.5Ti, Mo-55Ti, and Mo-57.5Ti with 18 mol pct Si and 9 mol pct B in each alloy, respectively. The experimental results from the second group of alloys as well as those in the first group, a total of nine, were then used to develop another improved and final thermodynamic description.

In order to test the predictive capability of the current thermodynamic description, it was decided to compare the calculated phase equilibria with the experimental results

obtained from three additional samples. The arbitrarily selected compositions of these samples lay within the narrow compositional region between the 2 four-phase equilibria (I) and (II). They were Mo-10Si-10B-25Ti, Mo-10Si-10B-27.5Ti, and Mo-10Si-10B-30Ti. It is important to point out that the experimental results obtained from these three alloys were used only for comparisons between calculation and experimentation, not for optimization. If the calculated results are in good agreement with experimental data from the third group of alloys, the current thermodynamic description is believed to be a reliable knowledgebase for predicting and understanding the phase equilibria among the bcc, T2, A15, T1, and $D8_8$ phases.

A thorough experimental investigation was carried out for all alloy samples using powder X-ray diffraction (XRD) analysis, Electron probe microanalysis (EPMA), electron backscatter diffraction (EBSD) analysis, and scanning electron microscopy (SEM) with backscattered electron (BSE) imaging analysis. Comparisons between experimental and calculated results for all investigated alloys were in good agreement, as presented elsewhere.[37] I will present here only the results obtained for one typical sample, Mo-18Si-9B-32.5Ti. As shown in Figure 12, a calculated isopleth expressed in terms of T as a function of x_{Ti} with values of $x_{Si} = 0.18$ and $x_B = 0.09$, the composition of this alloy lies in the four-phase equilibrium of T1 + T2 + bcc + $D8_8$ at 1600 °C and 1200 °C respectively. The BSE images of this sample heat treated at both temperatures are shown in Figures 13(a) and (b). The EPMA and EBSD results show the presence of T1 + T2 + bcc + $D8_8$ with the bcc phase exhibiting the brightest contrast, the T2 phase light gray, the T1 phase dark gray, and the $D8_8$ phase black. The phase fractions of each phase (in mole percentage) *vs* T were calculated under global equilibrium and shown in Figure 14. This kind of plot gives information not only on the phases in equilibrium with each other but also their amounts. It is evident from this figure that the major phase in the Mo-18Si-9B-32.5Ti is T2 and the minor phase $D8_8$ with the amounts of T1 and bcc somewhere in between these two. These predictions are qualitatively confirmed by the BSE images shown in Figures 13(a) and (b), respectively. It should be stated that the crystal structures of

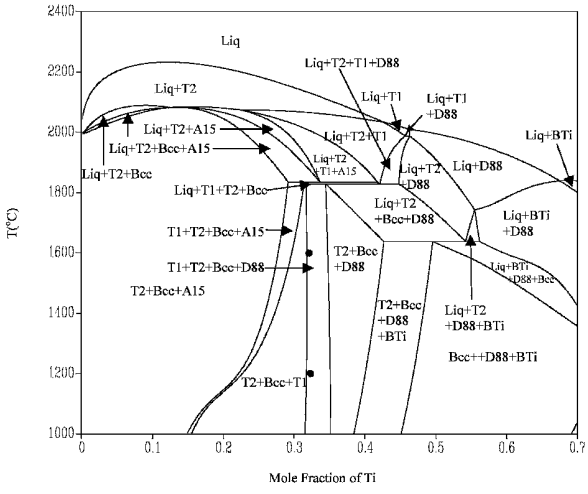

Fig. 12—A calculated isopleth of Mo-Si-B-Ti with the compositions of Si and B held constant at 18 and 9 mol pct, respectively. The solid circle refers to the alloy composition annealed at 1600 °C for 150 h and 1200 °C for 50 days, respectively. The compositions are given in mole fractions.

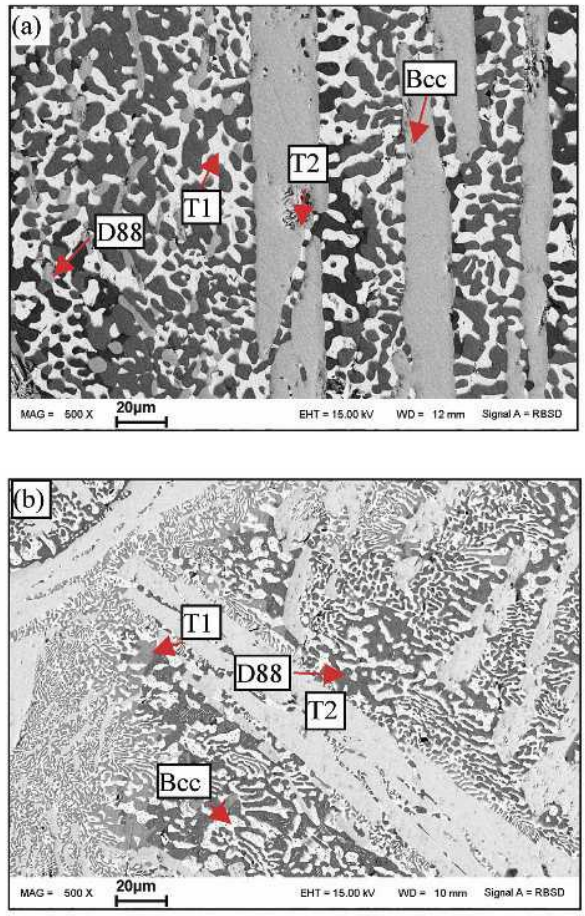

Fig. 13—(*a*) A BSE image of Mo-18Si-9B-32.5Ti annealed at 1600 °C for 150 h. (*b*) A BSE image of Mo-18Si-9B-32.5Ti annealed at 1200 °C for 50 days. The composition of the alloy is given in mol percent.

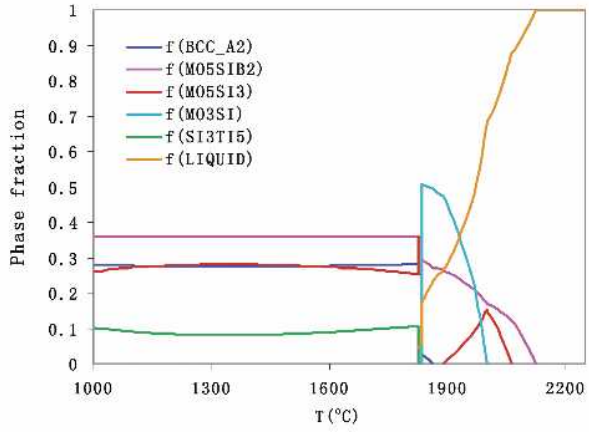

Fig. 14—Calculated phase fractions (in mole fractions) *vs* temperature for the Mo-18Si-9B-32.5Ti alloy with the compositions given in mol percent.

the phases were identified by XRD. However, it was found that the ternary T1 and $D8_8$ phases were difficult to discern by EPMA, since their atomic weights are very close to each other in view of the large mutual solubilities of the binary compounds. Furthermore, since they usually presented as minor phases (with small volume fractions) in the microstructure, XRD is incapable of differentiating them. However, EBSD was used to identify the crystal structures of these two ternary phases in this alloy, as shown in Figures 15(a) through (d). The EPMA measurements on phase compositions of the Mo-18Si-9B-32.5Ti alloy annealed at 1600 °C for 150 hours and 1200 °C for 50 days are listed in Table II. The concentrations of B and Si were relatively independent of the bulk alloy compositions. Taking the T2 phase as an example, the B and Si concentrations for all samples are 23.5 to 25.5 mol pct and 11 to 12.4 mol pct, respectively, which can be considered as constant values in view of experimental uncertainties. The equilibrium concentrations of Mo and Ti in the T2 phase vary with the overall compositions of the samples. This is also true for the bcc, T1, A15, and $D8_8$ phases. Therefore, only the Ti concentrations of each phase are listed in Table II. The B and Si concentrations were listed for each phase right below the phase name in the same table. The calculated phase compositions, also given in this table, are in accord with the experimentally measured values.

On the basis of the phase equilibrium data alone, the following five multiphase equilibria, bcc + T2 + A15, bcc + T2 + T1, bcc + T2 + $D8_8$, bcc + T2 + A15 + T1, and bcc + T2 + T1 + $D8_8$, offer the potentials to exhibit desirable mechanical properties since they all contain a ductile metallic phase with strong intermetallic compounds. In addition, the 2 three-phase equilibria consisting of bcc either with T2 and T1 or with T2 and $D8_8$ should also exhibit favorable oxidation resistance due to the higher Si concentrations in the silicides. The phase diagrams of Mo-Si-B-Ti calculated in this study, especially the following multiphase equilibria, bcc + T2 + A15, bcc + T2 + T1, bcc + T2 + $D8_8$, bcc + T2 + T1 + A15, and bcc + T2 + T1 + $D8_8$, offer wide processing windows to attain optimal microstructures and ultimately the desired mechanical performance. Since the

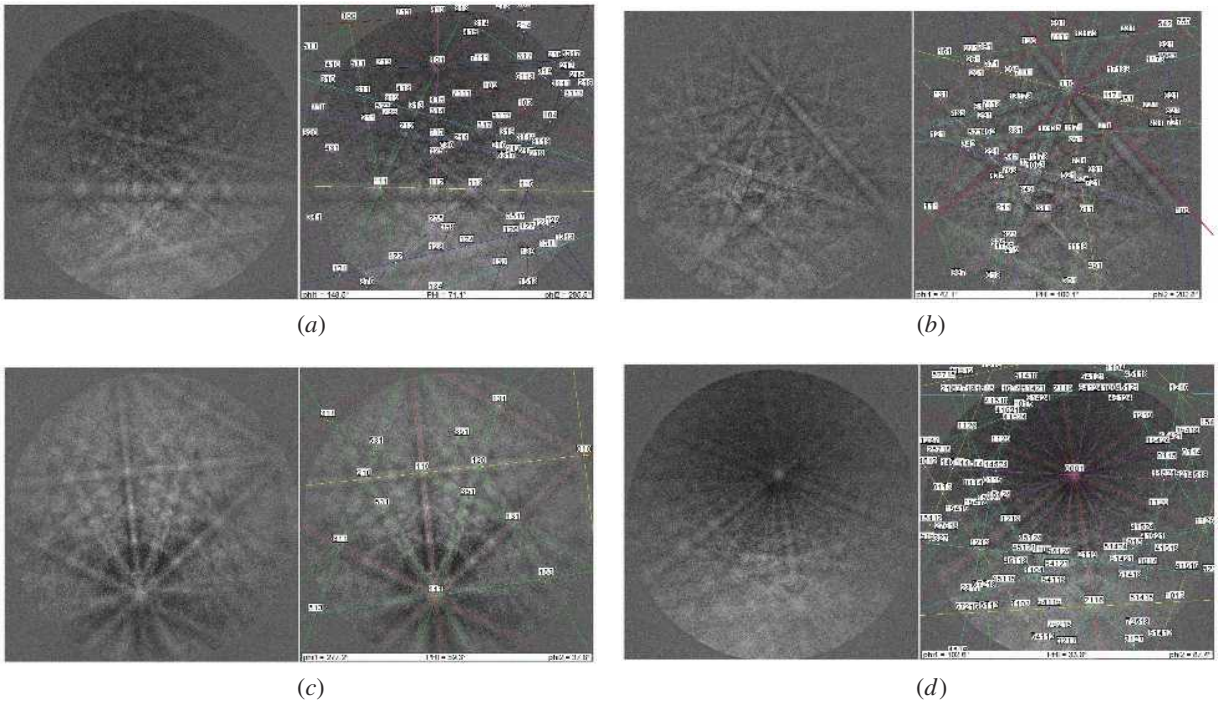

Fig. 15—EBSD patterns of the phases in the Mo-18Si-9B-32.5Ti sample (composition given in mol percent) with the unindexed patterns on the left and the indexed patterns on the right: (*a*) T1, (*b*) T2, (*c*) bcc, and (*d*) $D8_8$.

Table II. Comparisons between the Calculated and the EPMA Measured Values for the Compositions of Ti in Mol Fractions in Each of the Four Phases for the Alloys Annealed at 1600 °C for 150 Hours and 1200 °C for 50 Days

		T2	Bcc	T1	$D8_8$	
Samples	Annealing *T*	Si = 0.11 to 0.124 B = 0.235 to 0.255	Si = 0.016 to 0.03 B = 0 to 0.01	Si = 0.35 to 0.365 B = 0 to 0.01	Si = 0.35 to 0.37 B = 0 to 0.01	
Mo-18Si-9B-32.5Ti	1600 °C	0.265 ± 0.02	0.27 ± 0.01	0.423 ± 0.02	0.492 ± 0.01	exp
		0.248	0.278	0.416	0.502	cal
	1200 °C	0.26 ± 0.01	0.28 ± 0.02	0.43 ± 0.02	0.50 ± 0.02	exp
		0.249	0.261	0.427	0.521	cal

calculated phase diagrams far away from the Mo-Ti–rich region were extrapolated from the constituent ternary systems, it is expected that the topological features of the calculated phase diagrams are correct not necessarily the compositions of the co-existing phases in equilibrium with each other. Nevertheless, the calculated phase equilibria could offer an intelligent guide for identifying a few key alloy compositions for further experimental studies. In addition to new phase equilibria found in the Mo-Ti-Si-B system, another important message conveyed here is that thermodynamic modeling provides a powerful tool for studying and visualizing the multiphase equilibria, which otherwise would be a rather challenging task indeed.

B. *Materials Research/Development and Manufacturing: (2) Calculated Phase Diagrams of Al-Cu-Ni-Ti-Zr as a Guide to Identify Optimum Addition of Ti to Improve the Glass-Forming Ability of a Known Glass-Forming Quaternary (Al,Cu,Ni,Zr) Alloy*

As presented in Section II, the formation of a binary eutectic is a result of the greater stability of the liquid versus those of the competing solids. As shown in Figure 2(c), there are three phase diagrams: (1) the cigar-shaped liquidus/solidus phase boundaries are obtained when both the liquid and solid behave ideally; (2) a eutectic diagram is formed when L_0 (L) = 0 and L_0 (S) = 50,000 J mol^{-1}; and (3) a deep eutectic is formed when L_0 (L) = −50,000 mol^{-1} and L_0 (S) = 50,000 J mol^{-1}. This means that when L_0 (L) = 0 and L_0 (S) = 50,000 J mol^{-1}, the liquid is more stable than the solid phase and a eutectic is formed (case 2), *i.e.*, the stability of the liquid extends to lower temperatures. In the third case (3), when L_0 (L) = −50,000 mol^{-1}, meaning the liquid in this case becomes even more stable than that in case (2), a deep eutectic is formed. The stability of this already stable liquid is extended to a temperature lowered by additional 815 K. Since the viscosity of a liquid increases with decreasing temperature (with a corresponding decrease in diffusivity), it becomes kinetically favored for this liquid to form glass upon cooling. Moreover, it is known that glasses normally form over a range of composition in the compositional vicinity of the eutectic, but require larger undercooling at compositions away from the eutectic composition. In the following, I will give one example to illustrate the use of a calculated isopleth of a series of quinary (Zr,Cu,Ni,Al,Ti) alloys to identify the optimum composition for the best GFA. This isopleth is a two-dimensional representation of T *vs* the mol fraction of Ti, x_{Ti}, from 0 to 0.15 with constant compositions of x_{Cu} = 0.313, x_{Ni} = 0.04, and x_{Al} = 0.085.

Recent success in synthesizing centimeter-sized Cu- and Fe-based bulk metallic glasses (BMGs) using microalloying of Y[54,55] indicates that this success is due to decreases in the liquidus temperature with Y additions. This observation is consistent with the previous discussion. More recently, Ma *et al.*[56] demonstrated that this indeed is the case taking a quaternary glass-forming alloy $Zr_{56.28}Cu_{31.3}Ni_{4.0}Al_{8.5}$ as a model example with additions of Ti. As shown in Figure 16, the liquidus temperature from the quaternary alloy $Zr_{56.28}Cu_{31.3}Ni_{4.0}Al_{8.5}$, *i.e.*, without Ti, decreases rapidly, reaching a minimum at x_{Ti} = 0.049 and then increases again. These data suggest that the GFA of these alloys should increase with the addition of Ti, reaching a maximum at 4.9 mol pct Ti, and decrease again. I will present subsequently the experimental results obtained by Ma *et al.*[56] to show that this is indeed the case.

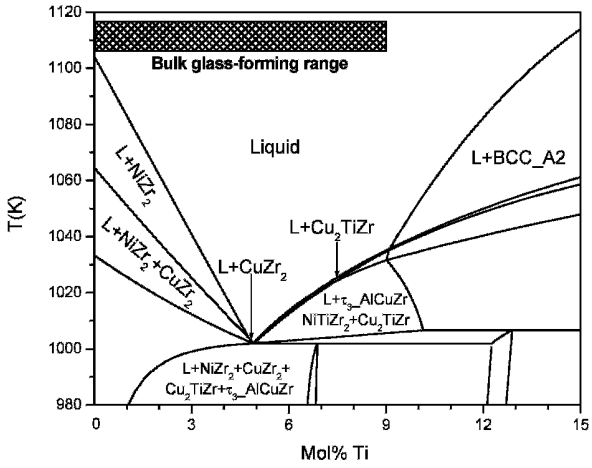

Fig. 16—A calculated isopleth of the quinary Al-Cu-Ni-Ti-Zr system expressed in terms of T as a function of the mol percent of Ti with the compositions of Cu, Ni, and Al held constant at 31.3, 4, and 8.5 mol pct, respectively. The composition of Ti at the origin is 0, corresponding to $Zr_{56.2}Cu_{31.3}Ni_{4.0}Al_{8.5}$. The shade area denotes the experimentally observed bulk glass-forming range.

A series of $Zr_{56.28-c}Ti_cCu_{31.3}Ni_{8.7}Al_{8.5}$ alloys with values of c varying from 0 to 10 mol pct Ti, were prepared by Ma et al. with the expectation that the alloy with 4.9 mol pct Ti would exhibit the highest GFA. The quaternary $Zr_{56.28}Cu_{31.3}Ni_{4.0}Al_{8.5}$ alloy was found to be a bulk glass-forming alloy based on the calculated low-lying liquidus surface of the quaternary Zr-Cu-Ni-Al system.[57] Alloy ingots with the nominal compositions $Zr_{56.28-c}Ti_cCu_{31.3}Ni_{8.7}Al_{8.5}$ (c = 0 to 10.0 mol pct) were prepared by arc melting pieces of high-purity metals, with Zr being 99.95 wt pct and the rest Ti, Cu, Ni, and Al being 99.99 wt pct, in a Ti-gettered argon atmosphere. Each of the ingot samples was remelted several times to assure good mixing and then suction cast (or drop cast), under a purified Ar (or He) atmosphere, into a copper mold with an internal cylindrical cavity with diameters ranging from 1 to 5 mm (or 6 to 14 mm). The amorphous nature of the as-cast rods was examined by analyzing the central part of their cross sections using XRD with a Cu K_α source and SEM in the backscattered electron imaging (BEI) mode. The glass transition and crystallization behaviors of these alloys upon reheating were characterized using a Perkin-Elmer DSC7 (differential scanning calorimeter) (Wellesley, MA) at a heating rate of 20 K/min.

As shown in Figure 17(a), the GFA of the quaternary base alloy increases with the addition of Ti in terms of the critical diameters of amorphous rods formed, reaching a maximum at 4.9 mol pct Ti, and then decreases again. At 10 mol pct Ti, it was no longer possible to achieve bulk glass formation. Also shown in Figure 17(b) are the 6-mm-diameter glass rod formed by casting the base alloy and the >14-mm-diameter glass rod formed with the alloy containing 4.9 mol pct Ti. Since the technique used by Ma *et al.*[56] is not capable of casting a rod larger than 14-mm diameter, it was concluded that larger diameters than 14 mm could be obtained.

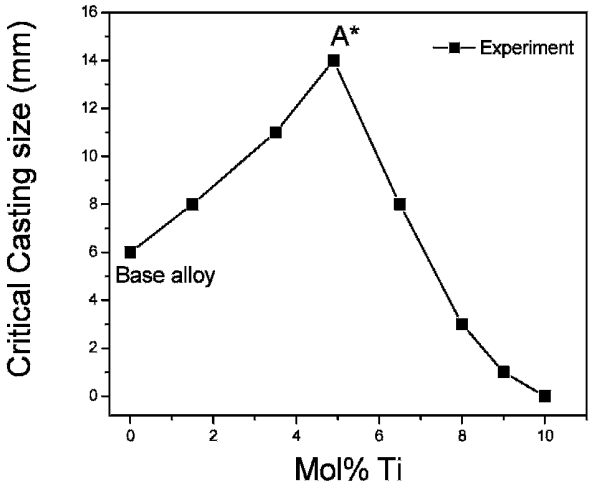

(*a*)

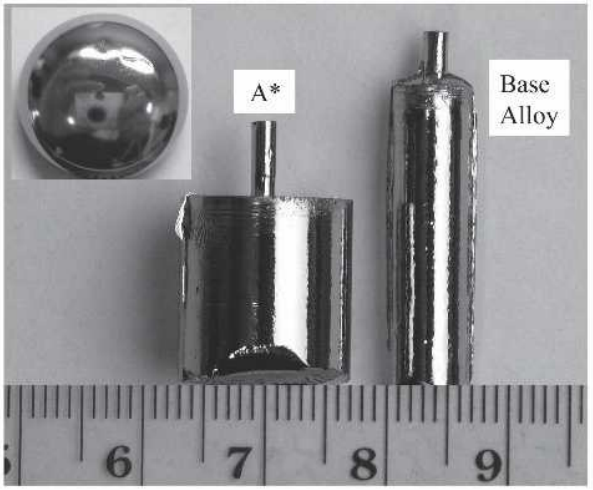

(*b*)

Fig. 17—(*a*) Critical diameters of the cast glassy rods as a function of the Ti concentration in mol percent. (*b*) Pictures of the 6-mm-diameter glass rod cast from the base alloy and of the 14-mm-diameter glass rod cast from the 4.9 mol pct Ti alloy, marked A*. The inset in (b) shows, with reduced image size, an arc-melted 20-g button used for casting the glass rod of alloy A*.

The inset in Figure 17(b) shows an arc-melted 20-g-button used for casting the amorphous rod of the alloy A*. These results are consistent with the liquidus temperatures shown in Figure 16. This is anticipated since a minimum amount of undercooling is required at the lowest temperature.

Figure 18 shows the XRD patterns obtained from the as-cast rods of four representative alloys, *i.e.*, $Zr_{56.2-c}Ti_cCu_{31.3}Ni_{4.0}Al_{8.5}$ with c = 0, 1.5, 4.9, and 6.5 mol pct, respectively. They are denoted as the base alloy, A1, A*, and A3, respectively. The base alloy exhibits two typical amorphous halos in its 6-mm-diameter sample. On the other hand, the 7-mm-diameter rod shows two crystalline peaks due to the presence of $CuZr_2$ and $NiZr_2$, respectively, indicating that the critical casting diameter for this alloy is ~6 mm. The diffraction patterns of the cast 10-mm-diameter rod, from the alloy containing 1.5 mol pct Ti and denoted as A1, also exhibit two similar crystalline peaks superimposed on the main halo. These peaks show that

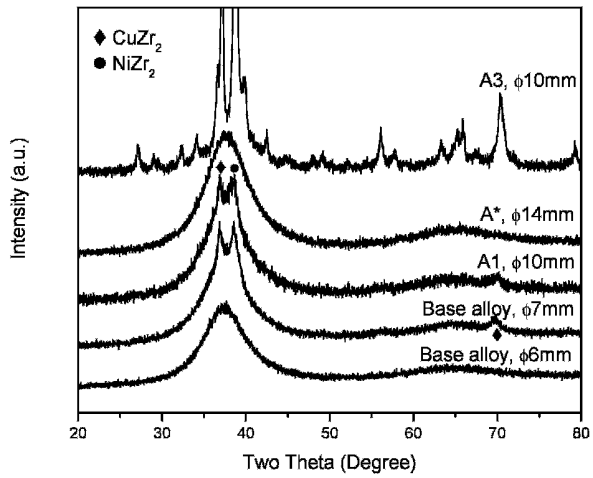

Fig. 18—X-ray diffraction patterns obtained from the as-cast rods with diameters of 6 and 7 mm for the base alloy ($Zr_{56.2}Cu_{31.3}Ni_{4.0}Al_{8.5}$), 10 mm for alloy A1 (containing 1.5 mol pct Ti), 14 mm for alloy A* (containing 4.9 mol pct Ti), and 10 mm for alloy A3 (containing 6.5 mol pct Ti).

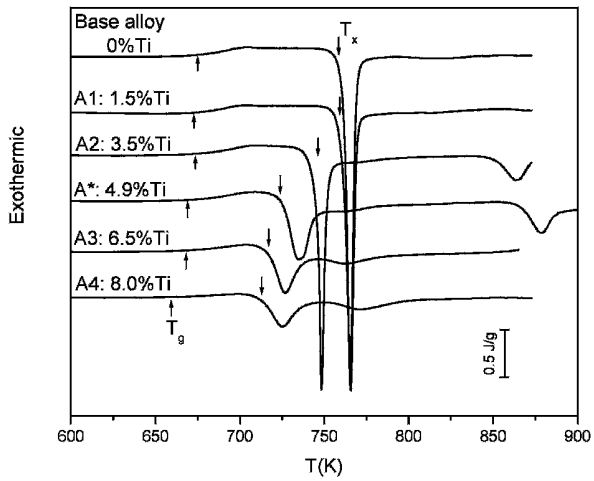

Fig. 19—DSC traces of a series of alloys $Zr_{56.2-c}Ti_cCu_{31.3}Ni_{4.0}Al_{8.5}$ (c = 0, 1.5, 3.5, 4.9, 6.5, 8.0 in mol pct), with the specimens being taken from 2-mm as-cast rods of these alloys. The upward arrows refer to the glass transition temperatures (T_g), and the downward ones denote the onset crystallization temperatures (T_x).

this rod is only partially glass. However, it is abundantly clear that there are no crystalline peaks discernible in the XRD patterns of alloy A* obtained from its 14-mm-diameter sample. This means that the rod is a monolithic glass. For alloys containing more than 6.5 pct Ti such as A3, their XRD patterns reveal even more and sharper peaks, indicating the presence of a considerable amount of crystalline phases in their 10-mm samples. However, with increasing Ti contents beyond this critical composition of 4.9 mol pct Ti, the critical casting diameter diminishes rapidly reducing to close to nothing when the Ti content reaches 10 mol pct.

The DSC curves of the cast amorphous rods presented in Figure 19 exhibit endothermic inflection characteristics of a glass transition at a temperature, T_g, ranging from 656 to 675 K, followed by one or two pronounced exothermic peaks

Table III. Glass-Forming Ability and Thermal Properties of a Series of (Zr, Ti, Cu, Ni, Al) Alloys (Denoted as Series A) Whose Compositions are Obtained by Replacing Zr with Ti in a Base Alloy $Zr_{56.2}Cu_{31.3}Ni_{4.0}Al_{8.5}$

Alloys	Ti Replacement (Mol Pct Ti)	d_{max} (mm)	T_l (K)	T_g (K)	T_x (K)	$T_x - T_g$ (K)	T_g/T_l	$T_x/(T_g + T_l)$
Base alloy	0.0	6	1104	675	761	86	0.611	0.428
A1	1.5	8	1073	673	762	89	0.627	0.436
A2	3.5	11	1030	674	746	72	0.654	0.438
A*	4.9	>14	1002	669	724	55	0.668	0.433
A3	6.5	8	1018	668	717	49	0.656	0.425
A4	8.0	3	1029	659	713	54	0.640	0.422
A5	9.0	1	1035	656	711	55	0.634	0.420
A6	10.0	0	1052	—	—	—	—	—

d_{max}: experimentally attained maximum diameter of glassy rods using copper mold casting.
T_l: the liquidus temperature calculated thermodynamically.
T_g: the glass transition temperature measured using DSC.
T_x: the onset temperature of crystallization measured using DSC.

corresponding to crystallization events. Values of T_x and T_g for each amorphous alloy obtained from the DSC traces with T_x being the onset crystallization temperature are summarized in Table III. The thermodynamically calculated liquidus temperatures T_l are also given in this table as well as the frequently used GFA criteria, $\Delta T_x = (T_x - T_g)$,[58] T_{rg},[59] and γ.[60] It is found that the value of T_{rg} peaks at 4.9 mol pct Ti, which corresponds exactly to the best glass-forming alloy, *i.e.*, A*. This is not surprising. Since values of T_g are insensitive to alloy composition, the shape of the compositional dependence of the reduced-glass temperatures is governed by the sharp decreases in the liquidus temperatures. On the other hand, the experimental measured results appear to be somewhat inconsistent with the other two criteria, *i.e.*, ΔT_x and γ.

Except for the aforementioned alloy series (A), Ma *et al.*[56] also calculated the isopleths in terms of *T vs* the compositions of Cu, Ni, Al, and ($Zr_{0.5628}Cu_{0.313}Ni_{0.040}Al_{0.085}$), respectively. In other words, each of the elements of Cu, Ni, Al, or ($Zr_{0.5628}Cu_{0.313}Ni_{0.040}Al_{0.085}$) was replaced with Ti. First, the experimentally determined values of the GFA are consistent with the calculated liquidus temperatures. Moreover, the minimum liquidus temperature calculated at 4.9 mol pct Ti when replacing Zr is by far the lowest. One can thus conclude that the strategy using the thermodynamically calculated liquidus temperatures has been proved to be robust in locating the bulkiest BMG former with optimum minor-alloying additions.

C. *Materials Research/Development and Manufacturing: (3) Calculated Solidification Paths as a Guide to Minimize Liquation Cracking in Aluminum Welds*

Metzger carried out an extensive investigation on liquation cracking in aluminum welds and found that this type of cracking in the 6061 alloy welds depended on the fillers used.[61] In other words, when a class of filler with a specific alloy composition is used, liquation cracking does not occur. Subsequently, several other researchers had extended his investigation to other aluminum alloys such as 6063 and 6082 and found similar results.[62–66] More recently, Huang and Kou[67,68] proposed a mechanism to explain the reason for liquation cracking, as shown in Figure 20. The top portion of this figure shows a schematic diagram of joining two pieces of Al metals with a weld pool in-between them. The partially melted zone (PMZ) is a portion of the base metal experiencing partial melting during welding, and the weld

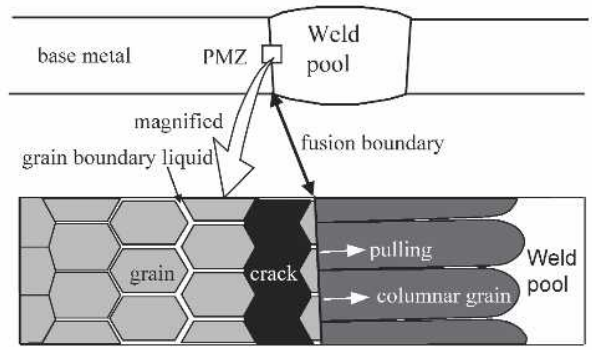

Fig. 20—A schematic diagram illustrating the mechanism of liquation cracking in full-penetration aluminum welds.[67]

pool is a mixture of the base metal with added filler at approximately 65 pct dilution. The interface, between the PMZ and the weld pool, referred to as the fusion boundary, is enlarged in the lower part of Figure 20. Huang and Kou postulated that when the fractions of solids in the weld pool during the later stage of solidification are less than those in the PMZ, liquation cracking should not occur since the base metal is stronger. On the other hand, if the reverse were the case, liquation cracking would occur because the solidifying weld metal is stronger and pulls away from the PMZ, causing cracking. Huang and Kou[67,68] calculated the fractions of solids in the PMZ and the weld pool using PANDAT[22] with a thermodynamic database for multicomponent Al alloys.[29] The results presented in Figure 21 indicate that the calculated fractions of the solid denoted as f_S in the PMZ according to the Scheil model are larger than those of the weld pool when the 4043 filler is used. The microstructures presented in Figure 22 show that this is indeed the case. Chang *et al.* had carried out similar calculations for other Al alloys and reached the same conclusion.[33]

D. *Materials Research/Development and Manufacturing: (4) Synthesis of Precursor Amorphous Alloy Thin Films of Oxide Tunnel Barriers Used in Magnetic Tunnel Junctions*

I will present in this section how computational thermodynamics can also facilitate processing innovation for synthesizing

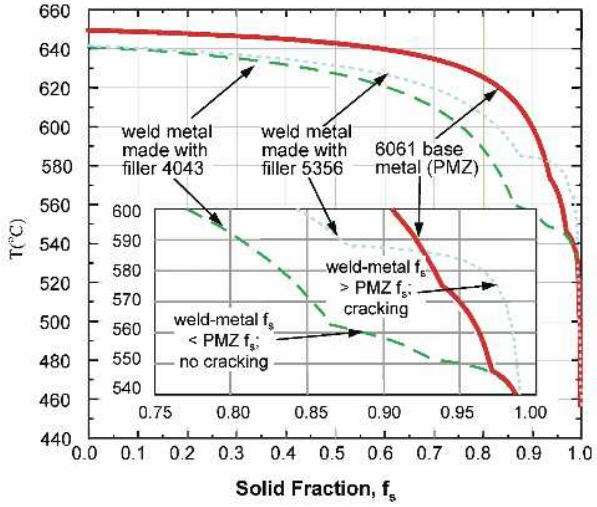

Fig. 21—The T vs f_S curves calculated by Huang and Kou[67] for the base metal or PMZ and the weld pool using PANDT[22] and an aluminum thermodynamic database[29] according to the Scheil model. The base metal is 6061 and the weld pool consists of the base metal with either filler 4043 or 5356 with 65 pct dilution. The base metals f_S are greater than the weld pools f_S with 4043 filler during the later stage of solidification (shown in the inset), and no liquation cracking occurs. The compositions of the base metal 6061 are Al-1Mg-0.6Si, filler 5356 Al-5Mg, and filler 4043:Al-5Si, all in weight percent.

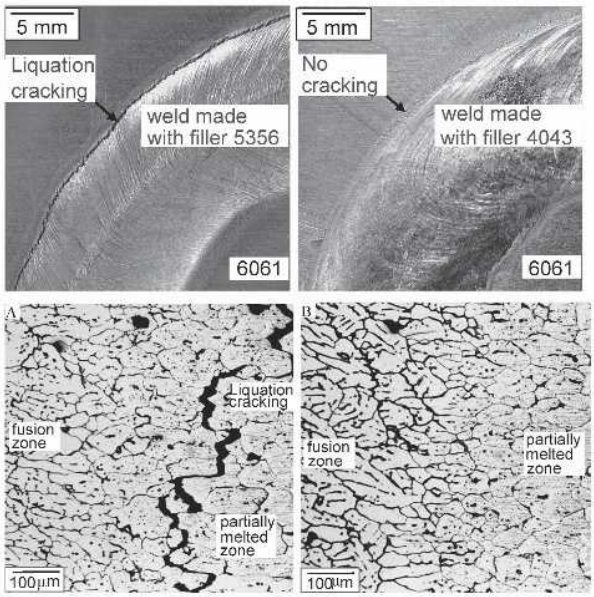

Fig. 22—Microstructures of the solidified weld pool and PMZ (base metal) near the fusion boundary (the top figure with low magnification and the lower one with higher magnification).

precursor amorphous alloy thin films of oxide tunnel barriers used in magnetic tunnel junctions (MTJs). These junctions are being considered as sensitive magnetic sensors and nonvolatile storage cells in magnetic access memories.[69–72] A MTJ consists of two ferromagnetic metal electrodes (*e.g.*, Co) separated by a thin tunnel barrier such as aluminum oxide with a thickness around 2 nms. One of the major challenges is to fabricate MTJs with both high tunneling magnetoresistance (TMR) and low product of junction resistance and area (RA) for practical applications.[73] The quality of a tunnel barrier such as aluminum oxide plays a critical role in the performance of such a device.[74,75] The current practice is to obtain an aluminum oxide barrier by oxidizing a thin crystalline Al layer.[76–81] However, since polycrystalline aluminum films have grain boundaries, the thin oxide barrier formed tends to exhibit nonuniform surfaces as well as other types of defects. An alternative approach is to oxidize an amorphous thin film without such boundaries of an alloy such as (Al,Zr). The oxide films thus formed tend to exhibit smooth interfaces with fewer defects, thus leading to higher performance of the MTJs, *i.e.*, with greater TMR.[74]

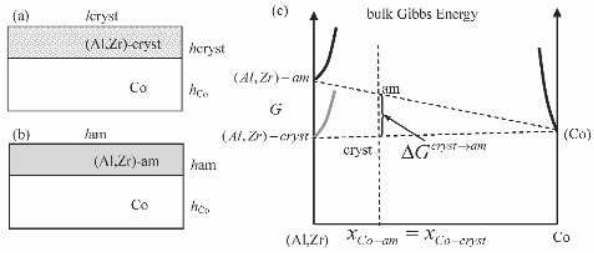

Fig. 23—Schematic diagrams of the bilayer structures with the (Al, Zr) layer in (*a*) crystalline state and (*b*) amorphous state; (*c*) the bulk Gibbs energy *vs* the composition of Co of the bilayer in (a) and (b) for the case that (Al, Zr)-cryst is more stable than (Al, Zr)-am. The symbols l and h refer to the length and height, respectively. The Co layer is in the crystalline state.

Since an amorphous phase was found in the Al-Zr system with different alloy preparation methods,[82–87] Yang *et al.*[88] adopted this binary as a model system for their thermodynamic and experimental study. They presented a thermodynamic formulation to predict alloy compositions that show tendencies to form amorphous thin films when fabricated by a rapid quenching process such as sputter deposition. The TEM and XRD were used to confirm the formation of amorphous alloy films. Based on the methodology proposed by Yang *et al.*, other alloys with higher amorphous-forming ability could be obtained as additional candidates for precursor metals of oxide tunnel barriers.

Figures 23(a) and (b) show two bilayered structures, one with an alloy of (Al,Zr) in the crystalline state on top of a thin layer of Co and the other with the same alloy in the amorphous state. The dimensions of the bilayered structure are given in these figures, *i.e.*, ℓcryst, ℓam, $h$am, and h_{Co}, with the subscripts denoting crystalline and amorphous, respectively. The total Gibbs energy of such a bilayer structure is taken to include three parts: bulk Gibbs energy, interfacial energy, and surface energy. The bulk Gibbs energies of these two (Co)/(Al,Zr) bilayer structures are shown schematically in Figure 23(c) as a function of the Co composition for the structure given in Figures 23(a) and (b), respectively. The assumption made is that all the intermetallic compounds normally stable in Al-Zr do not form due to kinetic constraints when using sputter deposition to fabricate these thin metallic films. In other words, the sputter-deposition process is so rapid that nucleation of these intermetallics becomes unfavorable. In deriving their thermodynamic model, Yang *et al.*[88] considered only the existence

of amorphous and crystalline phases of (Al,Zr). Moreover, the Gibbs energy curves of (Co), (Al,Zr)-am, and (Al,Zr)-cryst are represented by sharp curves at the two ends of the diagram because the mutual solubilities between Co and (Al,Zr)-am or (Al,Zr)-cryst are negligible at low temperatures (<500 °C). The tangent line between Co and (Al,Zr)-cryst represents the metastable phase equilibrium between Co and (Al,Zr)-cryst. Similarly, the tangent line between Co and (Al,Zr)-am represents the metastable phase equilibrium between Co and (Al,Zr)-am. The Gibbs energy of the amorphous phase is approximated to be that of the undercooled liquid and the volume Gibbs energies of (Al,Zr)-cryst can be either lower or higher than those of the amorphous phase depending on which state is more stable. Figure 23(c) shows the Gibbs energies of a mixture of (Al,Zr)-am and (Co) as well as that of (Al,Zr)-cryst and (Co) as a function of composition of Co at a constant T. For the case shown in this figure, the Gibbs energy of the two-phase mixture consisting of (Al,Zr)-am and (Co) is higher than that of (Al,Zr)-cryst and (Co). At a specific composition of x_{Co}, the Gibbs energy difference between the two states is shown in Figure 23(c) as $\Delta G^{cryst\rightarrow am}$. The symbol $\Delta G^{cryst\rightarrow am}$ denotes the Gibbs energy of transformation from a crystalline state for an (Aly_{Al},Zry_{Zr}) alloy to an amorphous state of an (Aly_{Al},Zry_{Zr}) alloy since (Co) in the structures shown in Figures 23(a) and (b) remains in the crystalline state. The symbols y_{Al} and y_{Zr} denote the mole fractions of Al and Zr in the binary (Al,Zr) alloys. This transformation energy is the barrier to be overcome for the formation of the amorphous state. The analytical equation of $\Delta G^{cryst\rightarrow am}$ at the as-deposited temperature is described as[88]

$$\frac{\Delta G^{cryst\rightarrow am}_{(Al,Zr)}}{(1-x_{Co})} = y^{am\,0}_{Al}\Delta H^{fus}_{Al}\left(1-\frac{T_{as}}{T^{cryst}_{m,Al}}\right) + y^{am\,0}_{Zr}\Delta H^{fus}_{Zr}\left(1-\frac{T_{as}}{T^{cryst}_{m,Zr}}\right) + \left({}^{ex}G^{am}_{(Al,Zr)} - {}^{ex}G^{cryst}_{(Al,Zr)}\right) \quad [2]$$

In Eq. [2], x_{Co} is the overall composition of Co in the bilayer structure and T_{as} the film deposition temperature; y^{am}_{Al} and y^{am}_{Zr} have been defined previously. Since the $(1-x_{Co})$ term is always positive and does not affect the sign of $\Delta G^{cryst\rightarrow am}$, the Co layer in the model can be replaced by other materials without changing the validity of the conclusions. The terms $T^{cryst}_{m,Al}$ and $T^{cryst}_{m,Zr}$ refer to the transition temperatures from the pure crystalline Al and Zr to their pure liquid, respectively. Similarly, $\Delta H^{cryst\rightarrow am}_{Al}$ and $\Delta H^{cryst\rightarrow am}_{Zr}$ represent the enthalpies of fusion of Al and Zr at their respective melting temperatures. The ${}^{ex}G^{am}_{(Al,Zr)}$ and ${}^{ex}G^{cryst}_{(Al,Zr)}$ denote the excess Gibbs energies of the (Al,Zr) alloys exhibiting the amorphous and crystalline state, respectively. In order to evaluate the energy barrier from the (Al,Zr) crystalline to (Al,Zr) amorphous structure, a prerequisite is to know which crystalline structure is the most stable structure. Based on the Gibbs energy of solution phases calculated from the thermodynamic description of the Al-Zr system developed by Wang *et al.*,[89] the Gibbs energy of the (Al,Zr) solution with the fcc structure was found to be the most stable among the common crystal structures, consistent with the experimental data to be presented later. Using the SGTE lattice stabilities of Al and Zr[4] and the excess Gibbs energies of the undercooled liquid (Al,Zr)-am and the fcc (Al, Zr)-cryst phases,[89] the values of $\Delta G^{cryst\rightarrow am}$ *vs* the composition of Zr in the top layer are shown in Figure 24. It is evident from the values of $\Delta G^{cryst\rightarrow am}$ shown in this figure that in the midpart of the diagram, amorphous alloys are likely to form during sputter deposition. It is indeed somewhat surprising that in view of the simplicity of the thermodynamic formation, the calculated compositions of the (Al,Zr) alloys for amorphous phase formation are in reasonable agreement with the experimental data presented in Figure 25. These data were obtained from TEM micrographs and SAD patterns of cosputtered deposited alloy films.[88] As shown in this figure, alloys with compositions denoted as A and B exhibit crystal grains with dotted SAD patterns. However, as the composition approaches point *C*, most of the grains disappear in the micrograph and multiple diffraction rings fade with a halo ring becoming clear in the SAD patterns. This suggests a transitional region from a polycrystalline structure to an amorphous state, in accord with the calculation. With increases in the Zr concentrations, the Al-Zr alloy films appear to be amorphous, which can be seen from the single diffuse ring in SAD patterns and the typical amorphous micrographs[90] (defocused to enhance the contrasted) at composition points *D*, *E*, and *F*. At point *G*, both the micrograph and the SAD pattern experienced an appreciable change from those of point *F*, suggesting the film transforms from an amorphous state to a crystalline structure again. At point *H*, *i.e.*, pure Zr, a polycrystalline fcc structure can be observed from both the micrograph and SAD pattern, indicating that the fcc Zr exist. Thicker films with typical compositions were deposited on glass for the XRD structure characterization, as shown in Figure 26. In the three XRD diffraction patterns, the big humps at about 24 deg result from the glass substrate, which was adopted to exclude any possible peaks from the substrate. This exercise indicates that the thermodynamic approach presented here can be used to make similar predictions for many other alloys and can identify alloy compositions for forming amorphous phases *via* sputter deposition, provided thermodynamic descriptions of the alloys in question are available.

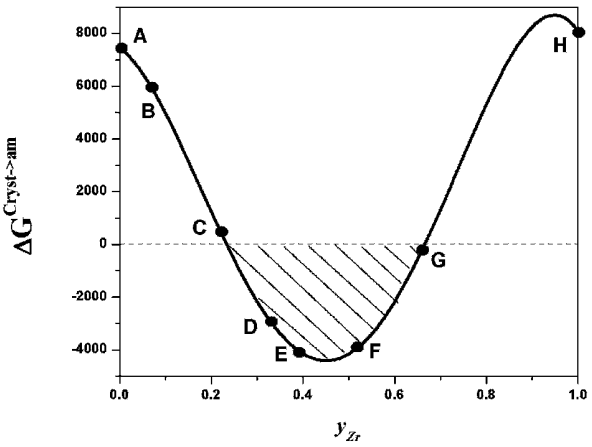

Fig. 24—The Gibbs energy difference between the fcc-(Al, Zr) solution and the amorphous (Al, Zr) phase *vs* the composition of Zr in mole fractions. Co-sputter-deposited alloys were made at the compositions denoted as A, B, *etc.* to H.

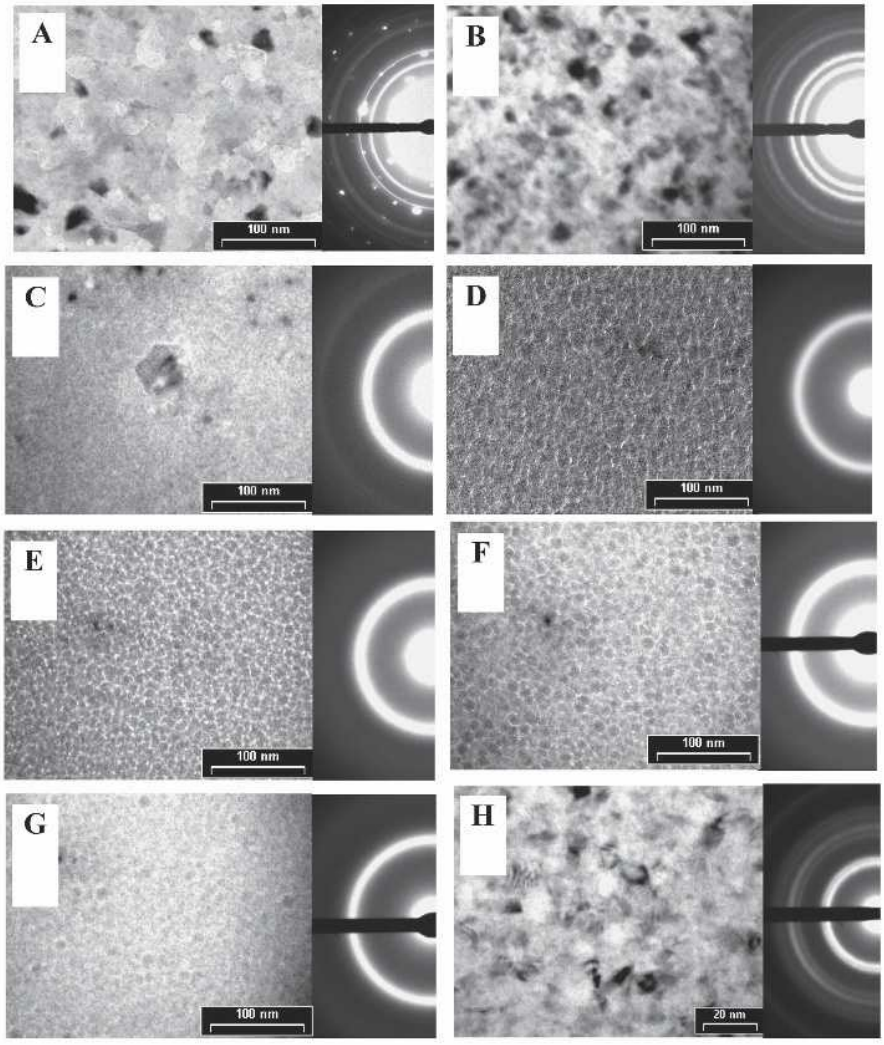

Fig. 25—TEM micrographs and SAD patterns of co-sputter-deposited (Al, Zr) alloy films with compositions of A—0, B—7, C—22, D—33, E—39, F—52, G—66, and H—100, all in mol percent of Zr.

E. *Materials Research/Development and Manufacturing: (5) Certification of Titanium Alloys for Commercialization*

In addition to playing an essential role in materials research and materials and processing development as noted previously, computational thermodynamics is beginning to play an important role in manufacturing. For instance, when a manufacturer sells products made of Ti6Al4V, it is necessary to certify the beta transus, *i.e.*, the temperatures of the transformation of Ti6Al4V from the high-temperature bcc structure, or beta (β), to the low-temperature hcp structure, or alpha (α). It is noteworthy to point out that the 6 wt pct Al and 4 wt pct V are the nominal compositions. The actual compositions in each batch of such alloys vary. In addition, there are always minute amounts of other impurities. The current practice in the titanium industry is that the metal supplier must carry out experiments such as DTA to measure experimentally the values of the transus for each batch of the metals sold. This measurement takes time and is thus costly. As part of the Manufacturing Affordability Initiative (MAI) of the Air Force Materials and Manufacturing (Wright-Patterson AFB, OH), Zhang[91] has been working with practicing engineers in the titanium metal industry to calculate the beta transus of Ti6Al4V using PANDAT[22] and PanTitanium.[92] Figure 27 shows a convincing correlation of the thermodynamically calculated beta transus values with those measured experimentally. It is not difficult to conclude that the beta transus could one day in the not too distant future be calculated thermodynamically for certification instead of requiring experimental measurement on individual batches of metals.

IV. RESEARCH

A. *Use of CSA to Calculate Multicomponent Phase Diagrams*

Chang *et al.*[46] had recently highlighted the great achievement of the Calphad approach in obtaining a thermodynamic description of a multicomponent alloy system based on descriptions of the lower order systems, normally binaries and ternaries. The lower order thermodynamic descriptions

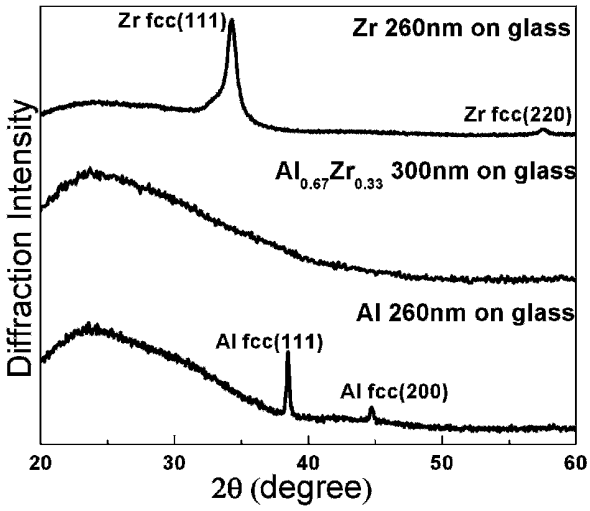

Fig. 26—The XRD results of three typical films on glass: pure Zr 260 nm, $Al_{0.67}Zr_{0.33}$ (in mole fractions) 300 nm, and pure Al 260 nm.

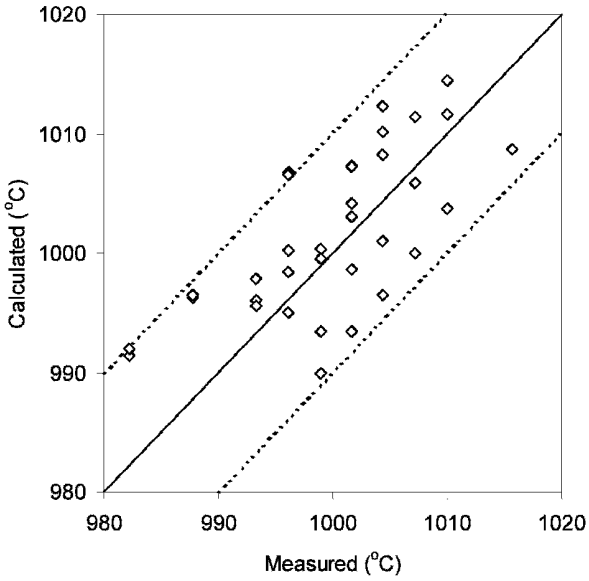

Fig. 27—A correlation of the thermodynamically calculated beta transus, *i.e.*, from the beta (bcc) phase to the alpha (hcp) phase using PANDAT and PanTitanium with actual measured values for Ti6Al4V. The experimental data were provided by D. Furrer, Ladish Co. (Cudahy, WI).

are developed in terms of known thermodynamic and phase equilibrium data. The thermodynamic data are mostly obtained experimentally, but some are obtained from the first principles calculations, particularly in recent years. The obtained thermodynamic descriptions for multicomponent systems can subsequently be validated with only limited experimental efforts, and experience has shown that the descriptions so obtained are quite good in many cases.[53] The exceptions are when a new phase forms in a quaternary system or a ternary phase extends into the quaternary temperature composition space, as is the case for the T2 phase in Mo-Si-B-Ti presented earlier in this article. From this description, it becomes possible to calculate a variety of phase diagrams of this multicomponent system such as isothermal sections, liquidus projection, isopleths, and stability diagrams, for teaching, research, and perhaps more importantly for practical applications. However, since the phase equilibria are governed by the relative Gibbs energies of the phases involved, it is often found that neither the experimentally measured nor first principles calculated thermodynamic quantities are sufficiently accurate to determine which of the possible phase equilibria corresponds to the stable one. Accordingly, experimental phase equilibrium data will continue to be needed for the lower order systems, particularly binaries, for the foreseeable future.

In spite of this great success of the Calphad approach in obtaining thermodynamic descriptions of multicomponent systems, there is also a continuing need to improve thermodynamic models, which, at present, are based on the Bragg–Williams approximation.[93,94,95] The compound energy formalism (CEF)[96] is one such model and is used nearly universally within the Calphad community. This model is used for phases that exist as disordered solutions at high temperatures but transform to ordered structures with decreases in temperatures. However, it has been well recognized that the formalism developed based on this approximation has difficulties in giving a satisfactory description of the thermodynamics of these phases due to the neglect of short-range ordering (SRO) in alloys at high temperatures.[46,97–99] Thus, the traditional Calphad approach does not lend confidence when extrapolating the thermodynamic descriptions of lower order systems to multicomponent alloys when ordered phases are involved, such as the technologically important Ni-based superalloys. Although the cluster variation method (CVM) is known to give a much improved description for the thermodynamics of the fcc phases,[100,101,102] it is computationally demanding, particularly for multicomponent alloy systems.[103,104] Accordingly, it becomes highly desirable to have a suitable and computationally efficient model to describe the thermodynamics of these phases, *i.e.*, the fcc phase, an ordered fcc phase, $L1_2$, with a stoichiometry of 0.75:0.25, and another ordered fcc phase, $L1_0$, with a stoichiometry of 0.5:0.5. The cluster/site approximation (CSA) also recognizes the existence of SRO but is computationally less demanding.[103,104] Oates *et al.*[104] demonstrated its suitability in accounting for the thermodynamics of the fcc phases in prototype Cu-Au binary. Subsequently, Zhang *et al.*[105] and Zhang *et al.*[106] showed the adequacy of the CSA to describe the thermodynamics of the hcp phase in Cd-Mg and the fcc phases in Ni-Al, respectively. More recently, Cao *et al.*[107,108] have successfully extended the use of the CSA first to the prototype ternary Cu-Ag-Au system and then to the real Ni-Al-Cr system. Prior to presenting the research results, I will first introduce the basic thermodynamic formulation for the CSA.[46,104,107]

The Gibbs energy of the fcc-base phases is taken to consist of two terms:[109]

$$G = G^{CI}(x_p) + G^{CD}(y_p^{(i)}) \qquad [3]$$

The quantity G^{CI} is the configurational independent term that depends only on the mole fractions of the component elements, *i.e.*, x_p, in the alloys but not on the details of the sublattice species occupation $y_p^{(i)}$. It is used to account for such quantities as excess elastic energies due to atomic size

mismatch, changing cell relaxation, and perhaps some other excess excitation contributions. The term G^{CD} is the configuration-dependent term and is a function of the distribution of the species $y_p^{(i)}$ on the respective sublattices. For the configuration-independent Gibbs energy G^{CI}, we use Eq. [1]. The term for G^{CD} according to the CSA[103–106] is

$$G^{CD} = \zeta RT\left(\sum_{p}^{C-1}\sum_{i=1}^{n} y_p^{(i)}\mu_p^{(i)} - \ln\varphi\right) - (n\zeta - 1)$$
$$RT\sum_{p}^{C}\sum_{i=1}^{n} f_i y_p^{(i)} \ln y_p^{(i)} \qquad [4]$$

where ζ is the number of energetically noninterfering clusters per site in the original CSA model[110] but can be treated as a parameter in developing a thermodynamic description for an alloy system, f_i are the sublattice fractions, n is the size of the cluster, and $y_p^{(i)}$, defined earlier, are the species fractions of component p on sublattice i. The $\mu_p^{(i)}$'s are the Lagrangian multipliers for the mass balance constraints in the Gibbs energy minimization and, physically, are related to the species chemical potentials of the lattice gas particles on the sublattice i. The cluster partition function, ϕ, is defined as

$$\varphi = \left(\sum_{j=1}^{C^n} \exp\left[\left(\sum_{i=1}^{n}\mu_p^{(i)}\right)_j - \varepsilon_j\right]\right) \qquad [5]$$

where ε_j is the cluster energy of a j-type cluster. The cluster energy can usually be obtained from the pair exchange energies, W, between components i and j.

For the prototype Cu-Ag-Au system, Cao *et al.*[107] compared the CSA-calculated coherent phase diagrams with the CVM-calculated ones by Kikuchi *et al.*[111] In other words, the G^{CI} term in Eq. [3] is taken to be zero and the CVM-calculated one is taken to be the "real" one. The CSA-calculated isotherms at high temperatures were found to be in accord with the CVM-calculated ones.[111] However, a distinct difference between the CSA-calculated isotherm at 240 °C and the CVM-calculated one was found, as shown in Figures 28(a) and (b). As shown in these two figures, while the CSA-calculated isotherm shows the existence of an island of the (Cu,Ag)Au_3 ($L1_2$) phase within the single-phase field of fcc α-(Au,Cu,Ag), the original CVM-calculated isotherm showed the absence of such an island. Professor C. Colinet (LTPCM-ENSEEG, Saint Martin d'Heres, France) subsequently recalculated this isotherm using the CVM and indeed found the existence of the $L1_2$ phase in the Au-rich corner, as shown in Figure 28(b). In the original CVM calculation, it was necessary to know the existence of this $L1_2$ phase in the Au-rich corner so as to estimate initial values to calculate the compositional stability of this phase. On the other hand, Cao *et al.*[107,108] used the PANDAT software, which is able to find the lowest Gibbs energy without starting points and thus obtain the most stable phase(s) automatically.[23,112,113] As noted above, ζ is the number of noninterfering clusters per site in the original CSA model (Eq. [2]). A value of $\zeta = 1.42$ was used for all three of the constituent binaries in the Cu-Ag-Au calculations.[107] It is also worthwhile pointing out that values of the pair exchange energies used in the CSA are, on average, within 5 pct of those used in the CVM.

Following on from our success in extending the CSA from binaries to calculating prototype ternary phase diagrams for the Cu-Ag-Au system, Cao *et al.*[108] began to apply

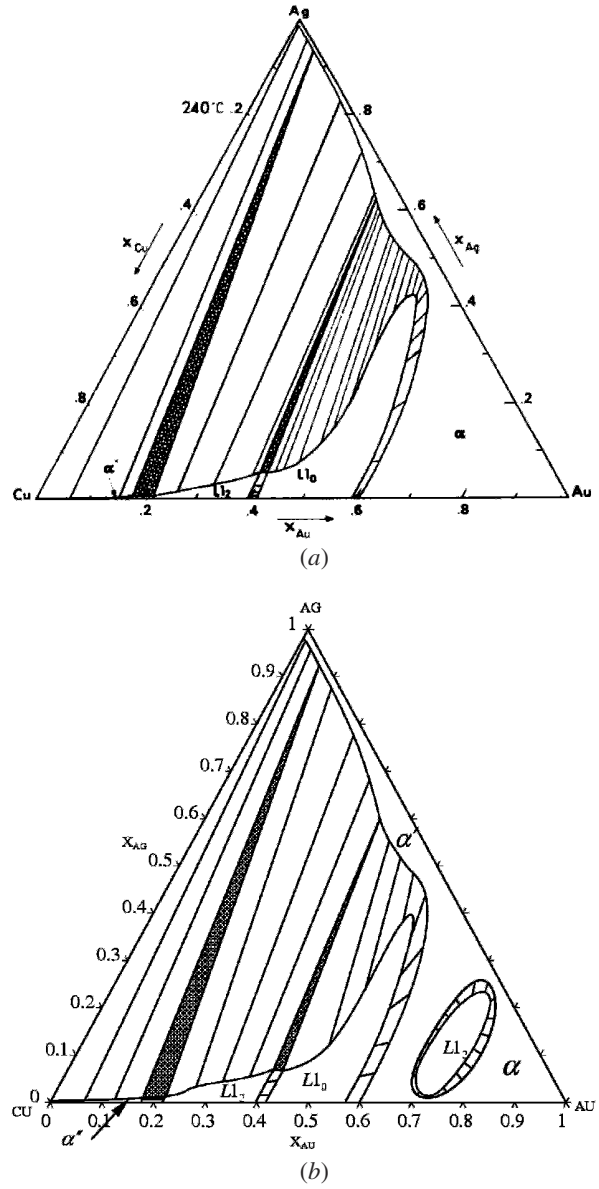

Fig. 28—Calculated coherent isotherms of Cu-Ag-Au at 240 °C: (*a*) CVM[111] and (*b*) CSA.[107]

this approximation to the fcc phases in the Ni-Al-Cr ternary system adopting the binary CSA description of Zhang *et al.*[106] for Ni-Al and obtained CSA descriptions for the other two binaries. Figures 29(a) and (b) show the CSA-calculated isotherm of Ni-Al-Cr at 1273 K and the CSA-calculated γ-solvus curves as a function of temperature along with experimental data. These γ-solvus curves were calculated at constant values of the mole fraction of Al varying from 0.09 to 0.17. The calculated phase boundaries, as shown in Figure 29(a), are consistent with the experimental data of Ochiai *et al.*,[114] and the calculated solvus of the γ phase shown in Figure 29(b) is in accord with the data of Hong *et al.*[115] Many other comparisons between calculation and experimental data were made and the agreement is similar

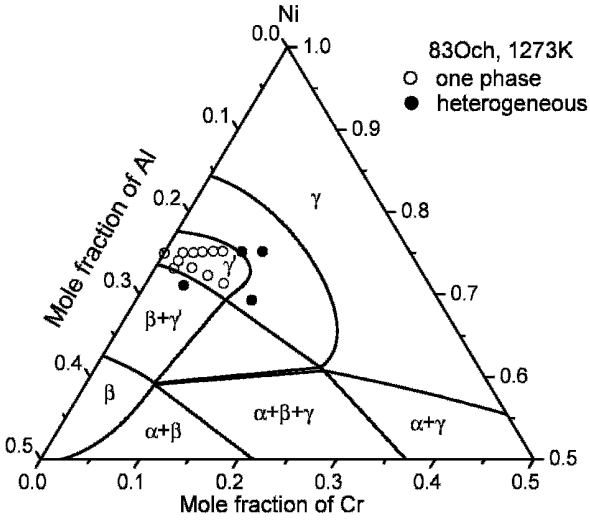

(*a*)

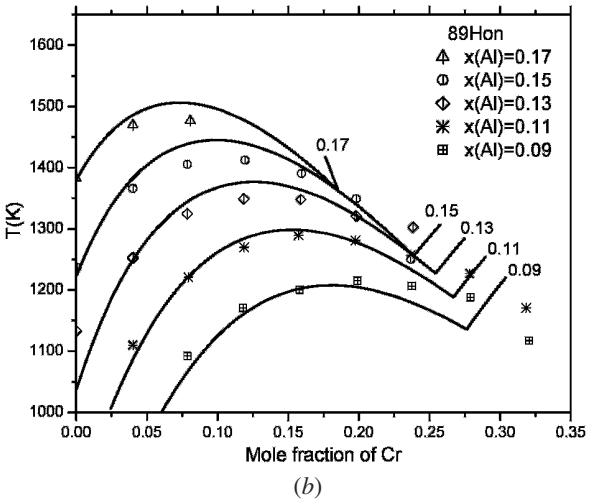

(*b*)

Fig. 29—Comparison of calculation with experimental data of Ni-Al-Cr:[108] (*a*) 1273 K (1000 °C) isothermal section and (*b*) the γ-solvus at constant values of Al.

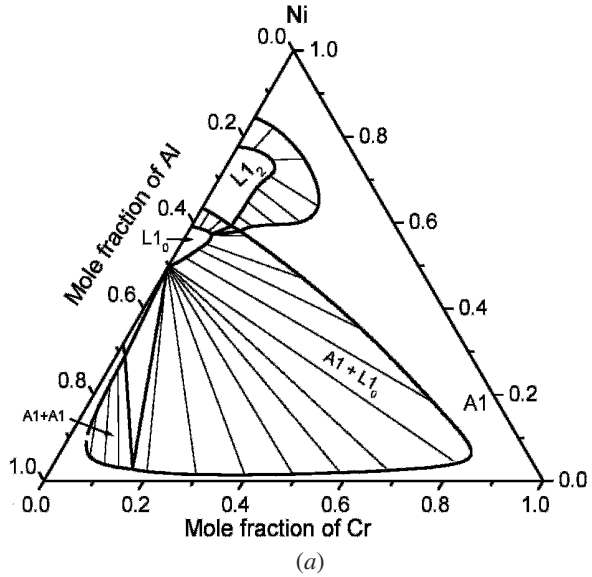

(*a*)

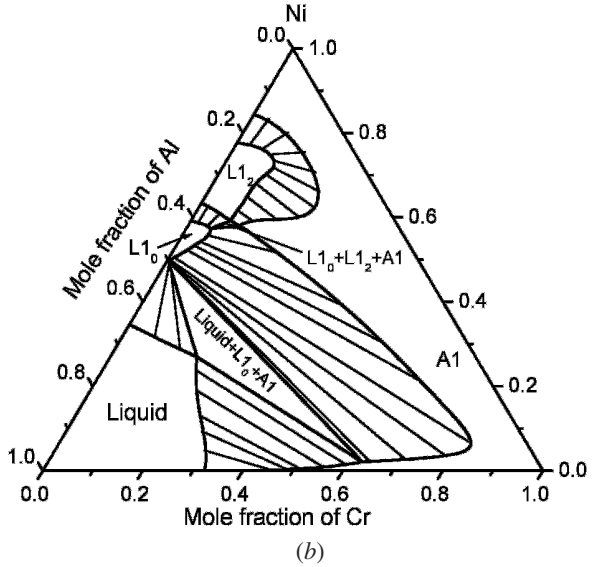

(*b*)

Fig. 30—CSA-calculated metastable isotherms of Ni-Al-Cr at 1273 K (1000 °C)[108]: (*a*) phase equilibria involving only the fcc phases and (*b*) phase equilibria involving only the fcc and the liquid phases.

to those shown in Figures 29(a) and (b) but not presented here.

An important question is: can one calculate metastable phase diagrams that are topologically correct using the thermodynamic models developed for each phase in terms of stable ternary phase equilibrium data and the binary thermodynamic descriptions? If one can, then the calculated metastable phase diagram can be used to study phase transformations and is likely to motivate researchers to synthesize metastable phases with desirable properties *via* novel experimental techniques. As shown in Figures 30(a) and (b), the calculated $\gamma + \gamma'$ (or $A1 + L1_2$) phase equilibria in the Ni-rich corner are nearly the same, as anticipated, since they correspond to the stable equilibria, as can be seen from Figure 29(a). Moreover, the calculated metastable phase equilibria away from the stable region, although different in these two diagrams, are consistent with the phase rule. In other words, the extensions of the phase boundaries to the metastable region show the existence of two-phase fields of $L1_2 + L1_0$, $A1 + L1_0$ as well as immiscibility of the A1 phase with the corresponding three-phase field toward the Al-rich corner. It is worth noting that Zhang *et al.*[106] had shown an immiscibility gap occurring in the A1 phase on the Al-rich side of the calculated metastable fcc Al-Ni binary diagram, as shown in Figure 31(a). It is noteworthy to point out that the topological features given in Figure 31(a) are the same as those obtained from first principle calculations coupled with the CVM.[116] For Figure 30(b), the liquid phase appears in the Al-rich corner with corresponding two- and three-phase fields involving the liquid phase. It is interesting also to compare the calculated metastable fcc isopleth with 2 mol pct Cr with that of Ni-Al,[106] as shown in Figure 31. Figure 31(a) shows that the A1(fcc) phase is

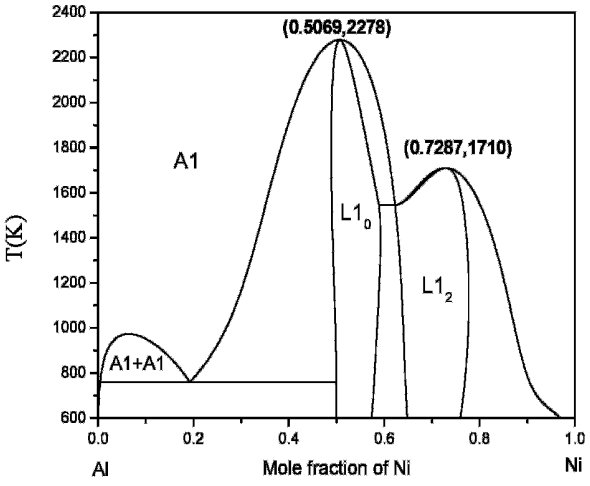

(*a*)

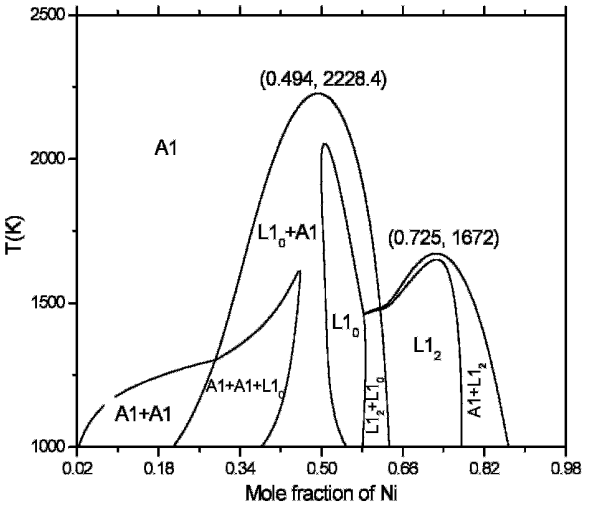

(*b*)

Fig. 31—CSA-calculated metastable fcc phase diagrams: (*a*) binary Ni-Al[106] and (*b*) an isopleth of Ni-Al-Cr with $x_{Cr} = 0.02$.[108]

stable at high temperatures. With decreasing temperature, the $L1_0$ appears at 50 mol pct Ni, the $L1_2$ phase at 75 mol pct Ni, and two A1 (fcc) phases toward the Al-rich side. The calculated isopleth with 2 mol pct Cr shown in Figure 31(b) has similar features except (1) a three-phase field of A1 + A1 + $L1_0$ appears between the 2 two-phase fields of A1 + A1 and A1 + $L1_0$ and (2) both the $L1_0$ and $L1_2$ phases no longer melt congruently as should be the case. These results are expected since a binary invariant such as the binary monotectoid, A1 + A1 + $L1_0$, becomes a tie-triangle in the ternary region over a range of temperatures. Of course, there is also another three-phase equilibrium of A1 + $L1_0$ + $L1_2$ also shown in this diagram at ~1470 K and ~60 mol pct Ni.

Figure 32 shows a calculated liquidus projection of the metastable Ni-Al-Cr ternary involving only the fcc and liquid phases. As shown in this figure, if the fcc phase were the only stable solid one, there would be a large range of compositions where the primary phase of solidification is

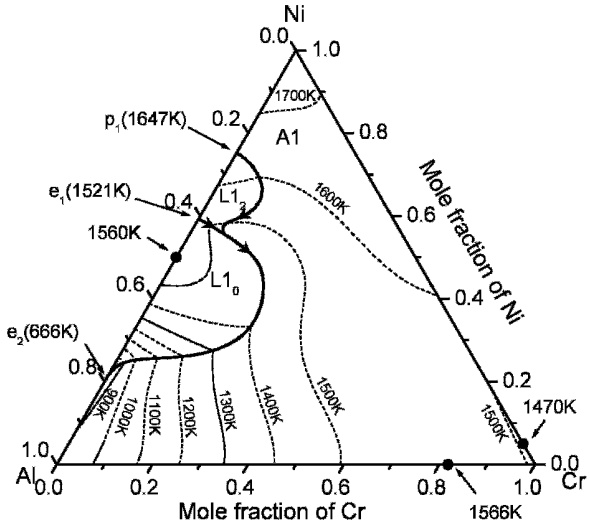

Fig. 32—CSA-calculated metastable liquidus projection of Ni-Al-Cr considering only the fcc and liquid phases in Ni-Al-Cr.[108] The solid circles indicate congruent melting.

the fcc-(Cr,Al,Ni) phase. The next one is the $L1_0$ phase and the last one the $L1_2$ phase. It would indeed be interesting to carry out some rapid quenching experiments such as melt spinning to confirm the calculated metastable liquidus projection. The phase diagrams for the binary Al-Cr and Ni-Cr systems are simple and are not presented here. The fcc solid solution of (Al,Cr) melts congruently at 82 at. pct Ni with a maximum temperature of 1566 K. On the other had, the fcc solid solution of (Ni,Cr) also melts congruently at 95 mol pct Cr with a minimum temperature of 1470 K. Moreover, the temperatures of the liquidus and solidus are very close to each other within 5 K. Figures 33(a) and (b) show the CSA-calculated metastable binary phase diagram of Al-Ni and an isopleth with a value of $x_{Cr} = 0.02$ when only the fcc and liquid phase exist. As shown in Figure 33(a), the $L1_0$ phase melts congruently and the $L1_2$ phase (γ') melts peritectically as in the stable Al-Ni phase diagram.[117] As a matter of fact, the calculated peritectic temperature of 1647 K is close to that of 1645 K in the stable Al-Ni diagram. On the other hand, the melting point of the $L1_0$ phase at 1560 K is much lower than the melting point of the stable β-NiAl (B2) phase at 1924 K (calculated) or 1915 K (experimental value with an uncertainty of ±15 K). This is understandable since the β phase is thermodynamically much more stable than the $L1_0$ phase. On the Al-rich side, a eutectic forms at a lower temperature than in the stable diagram. This is again anticipated since the intermetallic in the stable Al-Ni binary does not appear in this metastable phase diagram.

In view of the success of extending the CSA to calculate ternary Ni-Al-Cr properties, some of my graduate students are currently attempting to extend the use of the CSA to calculate phase diagrams of higher order alloy systems beyond three components.

It is worth noting that Kusoffsky *et al.*[118] and Abe and Sundman[119] have suggested modifications to the compound energy formalism (CEF),[96] used widely in the Calphad community, in an attempt to take into account the effect of SRO.

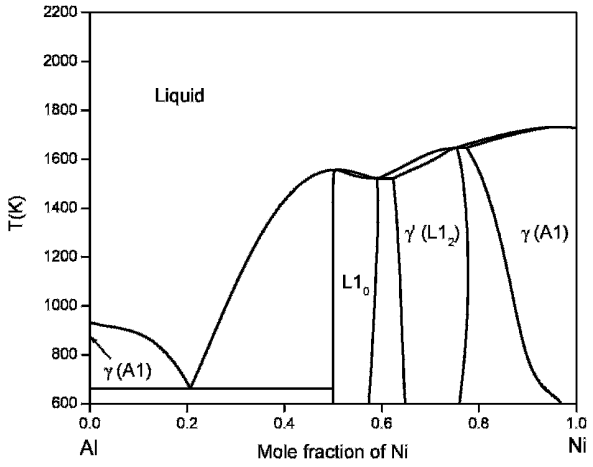

(*a*)

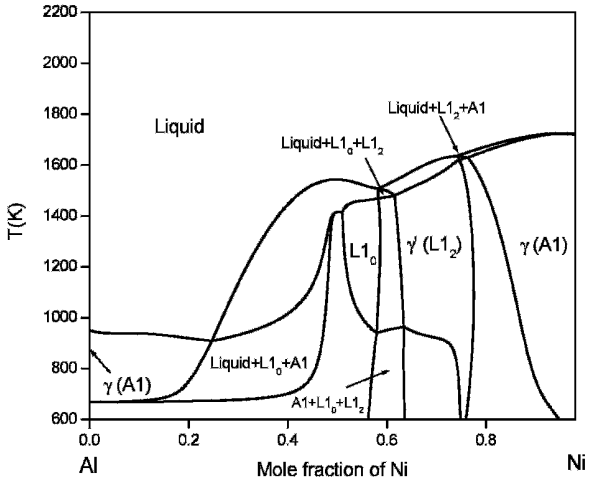

(*b*)

Fig. 33—CSA-calculated metastable phase diagrams involving only the fcc and liquid phases: (*a*) Ni-Al[106] and (*b*) an isopleth with $x_{Cr} = 0.02$.[108]

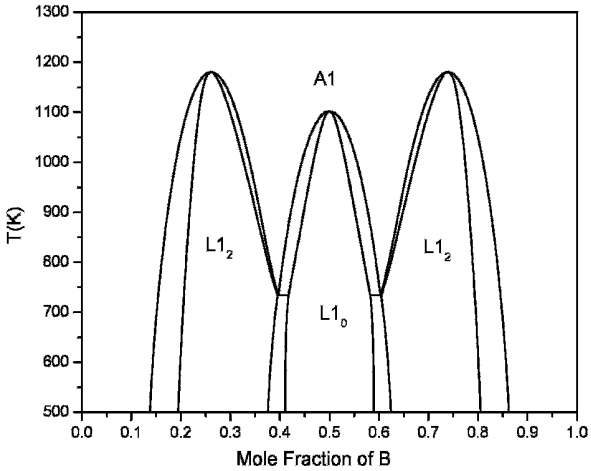

Fig. 34—Ordering phase diagram for the fcc phases calculated by the CSA using a pair exchange energy, $W_{AB} = -10{,}000$ J mol^{-1}, with a value of $\zeta = 1.3$.

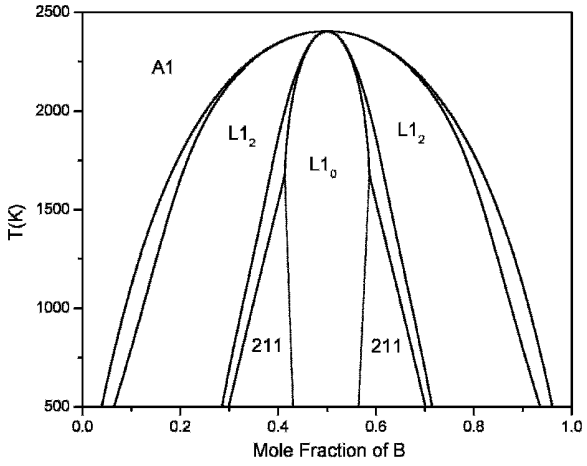

Fig. 35—Ordering phase diagram for the fcc phases calculated by the CEF using $U_{AB} = -10{,}000$ J mol^{-1}. The U_{AB} is the same as W_{AB}.

The CEF is rather complex and the readers are referred to the original article for a detailed description.[118] I will only give a brief summary. In its simplest form, the Gibbs energy in the CEF consists of three terms: one from end member compound energies, one from ideal mixing on the sublattices, and the third is an excess Gibbs energy. The latter is represented by Eq. [1], except that the parameters corresponding to interactions between atoms on different sublattices are introduced and referred to as the L parameters. These can be of many different types, with the ones of interest in the present context being the so-called reciprocal L parameters. When no reciprocal L parameters are used in the CEF, a Cu-Au phase diagram originally calculated by Shockley is obtained and is found to be topologically unsatisfactory. The introduction of the reciprocal L parameters, on the other hand, has been shown to account for the topological features of the Cu-Au phase diagram in a more satisfactory manner.[118] It should be appreciated, however, that *this has been achieved without the explicit introduction of SRO*. The effect of the reciprocal L parameters is to make the mixing enthalpy of the disordered phase more exothermic while having a minimal effect on the mixing enthalpy of the ordered phase. The configurational entropy of the disordered phase still corresponds to that of a random solution, *i.e.*, there is no SRO present. The ability of the CVM and CSA, on the other hand, to describe the topological features of the Cu-Au phase diagram comes directly from the configurational entropy of mixing contribution to the Gibbs energy, *i.e.*, SRO is explicitly considered.

Figures 34 and 35 show, respectively, a CSA-calculated and a CEF-calculated ordering phase diagram for the fcc phases in a binary A-B using the same pair exchange energy parameter, $W_{AB} = -10{,}000$ J mol^{-1}. For the CSA, a value of $\zeta = 1.3$ is used. It is evidently clear from Figure 34 that the topological features of the CSA-calculated diagram are identical to those of the CVM-calculated[100] and experimental phase diagram.[7] On the other hand, the topological features of the CEF-calculated phase diagram are the same as those calculated by Shockley.[97] In other words, all three

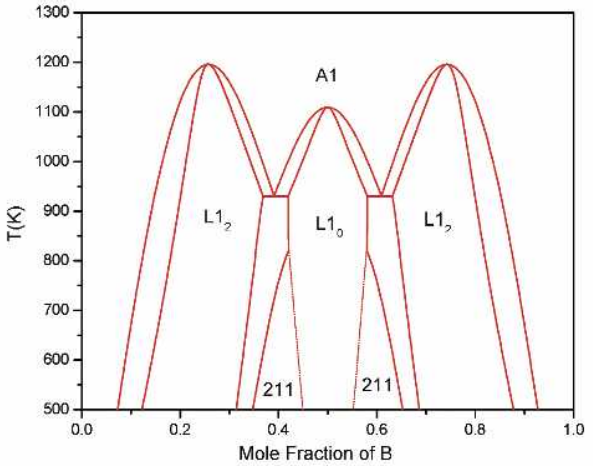

Fig. 36—Ordering phase diagram for the fcc phases calculated by the modified CEF using $U_{AB} = -10{,}000$ J mol^{-1} with the 24 reciprocal parameters given in Table IV. All the reciprocal parameters are taken to be $-10{,}000$ J mol^{-1}.

Table IV. Reciprocal Parameters Used to Calculate the Phase Diagrams in Figures 36 and 37 and the Thermodynamic Properties in Figure 38(a) through (c)

Index	Type	Value, J mol^{-1}
1	$L_{A,B:A,B:A:A}$	−10,000
2	$L_{A,B:A,B:A:B}$	−10,000
3	$L_{A,B:A,B:B:A}$	−10,000
4	$L_{A,B:A,B:B:B}$	−10,000
5	$L_{A,B:A:A,B:A}$	−10,000
6	$L_{A,B:A:A,B:B}$	−10,000
7	$L_{A,B:B:A,B:A}$	−10,000
8	$L_{A,B:B:A,B:B}$	−10,000
9	$L_{A,B:A:A:A,B}$	−10,000
10	$L_{A,B:A:B:A,B}$	−10,000
11	$L_{A,B:B:A:A,B}$	−10,000
12	$L_{A,B:B:B:A,B}$	−10,000
13	$L_{A:A,B:A,B:A}$	−10,000
14	$L_{A:A,B:A,B:B}$	−10,000
15	$L_{B:A,B:A,B:A}$	−10,000
16	$L_{B:A,B:A,B:B}$	−10,000
17	$L_{A:A,B:A:A,B}$	−10,000
18	$L_{A:A,B:B:A,B}$	−10,000
19	$L_{B:A,B:A:A,B}$	−10,000
20	$L_{B:A,B:B:A,B}$	−10,000
21	$L_{A:A:A,B:A,B}$	−10,000
22	$L_{A:B:A,B:A,B}$	−10,000
23	$L_{B:A:A,B:A,B}$	−10,000
24	$L_{B:B:A,B:A,B}$	−10,000

ordered phases, *i.e.*, $L1_2$, $L1_0$, and $L1_2$, transform to the disordered state at 50 mol pct. In addition, two 211 phases, or AABX with X being a mixture of A and B, form at lower temperatures. However, when a constant value of $-10{,}000$ J mol^{-1} is introduced for all 24 reciprocal L parameters, as given in Table IV, the topological features of the modified CEF-calculated diagram, as shown in Figure 36, correspond closely to those of the CVM- and CSA-calculated diagrams as well as the experimental one. The difference is the appearance of the two 211 phases in the modified CEF-calculated diagram. Shown in Figure 37 are the CEF- and modified

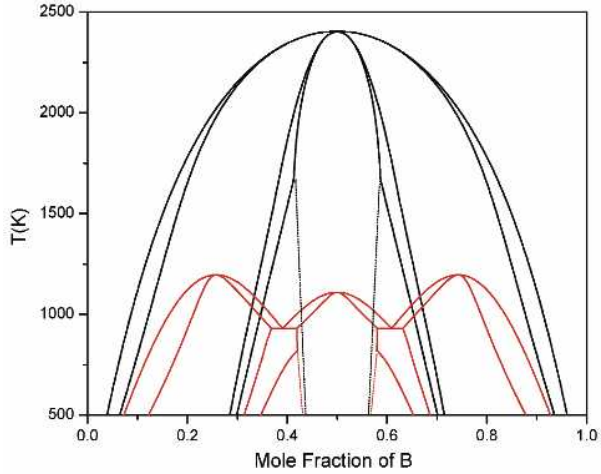

Fig. 37—Two ordering phase diagrams for the fcc phases calculated by the CEF and the modified CEF using the energy parameter and reciprocal parameters given in Figs. 35 and 36, respectively.

CEF-calculated ordering phase diagrams of a binary A-B, the former shown in black and the latter in red color.

Values of the Gibbs energy for the fcc phases at 50 mol pct calculated by CVM, CSA, CEF, and modified CEF are presented in Figure 38(a) as a function of temperature. The two Gibbs energy curves calculated by CVM and CSA are nearly the same, while the CEF-calculated values differ appreciably. First, the transformation from the ordered structure to the disordered one is of second order; and second, values of the Gibbs energy are more positive. With the introduction of the 24 reciprocal L parameters in the modified CEF, the calculated Gibbs energy values exhibit also a first-order phase transition. Let us now examine the CVM-, CSA-, CEF-, and modified CEF-calculated values of the enthalpy and entropy as a function of temperature shown in Figures 38(b) and (c). As shown in Figure 38(c), values of the entropy calculated by CVM and CSA are nearly the same while those of the modified CEF-calculated values are considerably higher. The appreciable differences in the calculated entropy values are due to the fact that SRO is taken care of in both the CVM and CSA but not in the modified CEF. In other words, the entropy of mixing in the modified CEF remains random and no SRO is accounted for. The larger entropy values obtained from the modified CEF are compensated for by the more positive enthalpy values, as shown in Figure 38(b). Compensation of these two quantities allows the calculated Gibbs energy values in the disordered and ordered phases to become identical at the desired transition temperature. This is achieved by adjusting the values of the reciprocal L parameters. Although it is possible to use this approach to obtain the topological features of a binary system based on the fcc structure, the entropy of mixing clearly does not include the existence of SRO. Moreover, the existence of the 211 phases also occurs at lower temperatures using the modified CEF; however, they do not appear in the CVM- and CSA-calculated phase diagrams.

B. *Use of the CSA for Calculating Coherent Interphase Boundary Energies*

In addition to bulk thermodynamic properties, interphase boundary (IPB) energies are also essential in describing

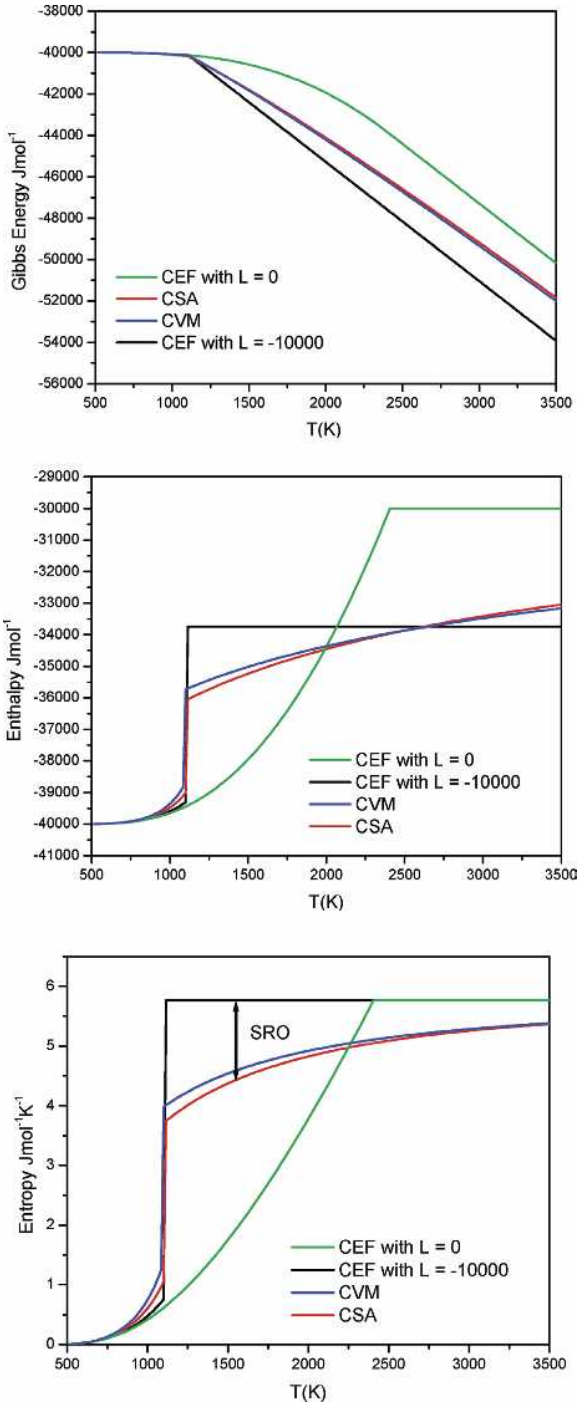

Fig. 38—The entropy, enthalpy, and Gibbs energy calculated by CVM, CSA, CEF, and modified CEF as functions of temperature at 50 mol pct.

phase transformations in an alloy and its subsequent microstructure evolution when this alloy is subjected to a thermal treatment. Yet, experimental data of IPB energies are rarely available due to the experimental difficulties in determining these quantities. This is particularly true for multicomponent alloys, and yet most real alloys are multicomponent. However, there have been attempts to calculate these quantities, such as the calculation of the IPB energies between two immiscible phases in binary alloys using the regular solution mode by Lee and Aaronson[120] and those between the fcc (A1) phase and the ordered phase ($L1_2$) using the CVM by Kikuchi and Cahn.[121] In the following, I will first present the CSA-calculated IPB energies between prototype A1-(Cu,Au) and $L1_2$-(Cu_3Au) by Cao *et al.*, which[122] are in accord with the CVM ones by Kikuchi and Cahn. I will then present the CSA-calculated values between the A1 and $L1_2$ phases in Al-Li and Ni-Al alloys, respectively. Last, I will present some CSA-calculated results on the effect of decreasing the layer thickness in a multilayered nanostructure on the critical temperature of a binary miscibility gap.

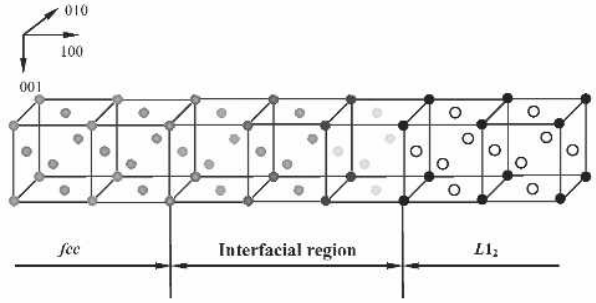

Fig. 39—A schematic supercell with a (100) IPB between an fcc (A1) phase and an $L1_2$ phase in a binary A-B. The black spheres represent A atoms such as Cu and Ni and the white spheres B atoms such as Au and Al. The gray color with differing intensities represents solution (A, B) with differing concentrations. The left side of this supercell represents the fcc (A1) phase and the right side the $L1_2$ phase. Only four lattice planes are shown but in reality there are many more than four.

Figure 39 shows a schematic representation of a supercell consisting of the fcc (A1) structure on the left and the $L1_2$ structure on the right with a (100) IPB between them. It is understood that the number of lattice planes for these two phases are many more than the four shown in this figure and the number of the lattice planes in the IPB depends on the IPB energy. The interfacial energy σ is the excess Gibbs energy of the entire system per unit interfacial area A due the existence of the interface. Thus, the interfacial energy is the difference between the total energy of the entire system less the bulk energy of the two phases normalized by the interfacial area as

$$\sigma = \frac{1}{A}\left[G - \sum_{i=1}^{C} \mu_i x_i \right] \qquad [6]$$

The symbols σ and A have been defined as noted above; G is the Gibbs energy of the entire system and $\sum_{i=1}^{C} \mu_i x_i$ is the Gibbs energy of the bulk alloy, with μ_i and x_i being the chemical potential and the mole fractions of the component i. Following the approach of Kikuchi and Cahn,[121] values of the IPB energies were calculated as a function of temperature using the CSA instead of the CVM. The results are presented in Figures 40(a) and (b). In both cases, the tetrahedron approximation was used. Cao *et al.*[122] used a pair exchange energy W for the CSA calculation from Oates *et al.*[104] As shown in Figure 40(b), the CSA-calculated IPB energies for the (100) plane are in accord with those given in Figure 40(a) calculated by Kikuchi and Cahn from the congruent

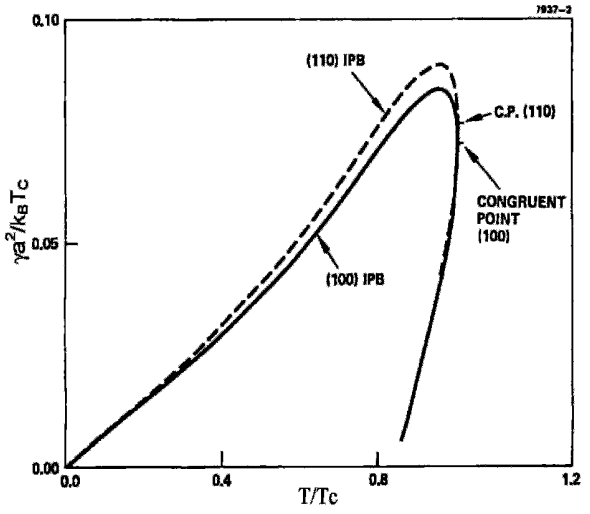

(*a*)

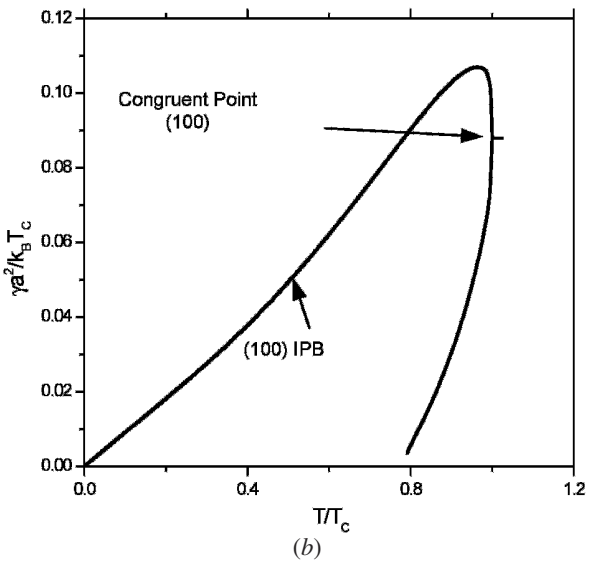

(*b*)

Fig. 40—Calculated coherent IPB energies between the fcc-(Cu, Au) and $L1_2$-Cu_3Au phases using the tetrahedron approximation: (*a*) CVM-calculated values for the (100) and (110) planes[121] and (*b*) CSA calculated values for the (100) planes.[122]

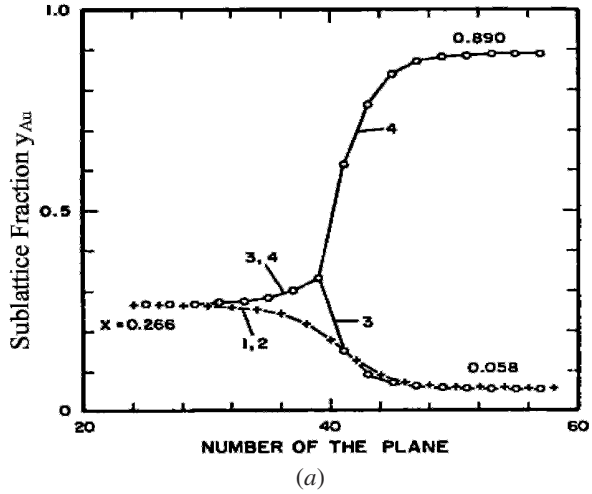

(*a*)

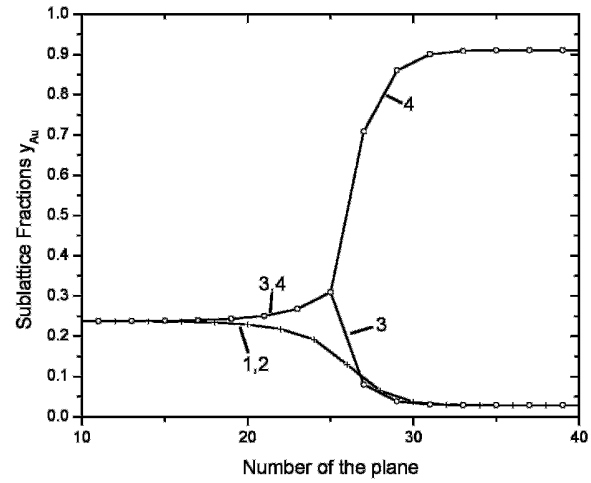

(*b*)

Fig. 41—Calculated concentration profile for the (100) IPB at the congruent point: (*a*) CVM[121] and (*b*) CSA.[122]

point down to low temperatures. As also shown in Figure 41(b), the CSA-calculated concentration profile for the (100) IPB between these two phases at the congruent point are also in accord with the CVM-calculated values shown in Figure 41(a). Clearly, a diffused interface exists between the A1 and the $L1_2$ phases. As noted previously,[121,123] the vanishing of the calculated IPB energy at 0 K using the tetrahedron approximation is due to the neglect of the longer range interaction in the lattice. Using the tetrahedron-octahedron approximation of the CVM (TO-CVM), expressed in terms of the parameter $\alpha = W_{AB}^{(2)}/W_{AB}^{(1)} = -0.1$, Asta[123] calculated the phase diagrams of the prototype Cu-Au binary and then the coherent IPB energies between the fcc-(Cu,Au) and the $L1_2$-(Cu_3Au) phases. The terms $W_{AB}^{(2)}$ and $W_{AB}^{(1)}$ denote the next nearest neighbor and the nearest neighbor pair exchange energies, respectively. Figures 42(a) and (b) show the TO-CVM and tetrahedron-pair approximation of the CSA (TP-CSA) calculated phase diagram and coherent IPB energies between the fcc-(Cu, Au) and $L1_2$-Cu_3Au phases for the (100) planes. The TO-CVM calculated values were taken from Asta[123] and shown in these figures as discrete points while the TP-CSA-calculated values are plotted as smooth curves. As shown in Figure 42(b), the coherent IPB energy at 0 K is finite and decreases first with increasing temperature and then changes slowly with further increases in temperatures. Cao *et al.*[122] used the TP-CSA to calculate the phase diagram and coherent IPB energies.[124] Their calculated reduced temperatures expressed as a function of composition as shown in Figure 42(a) are in accord with the TO-CVM calculated values. Likewise, the TP-CSA calculated coherent IPB energies given in Figure 42(b) shown as a smoothed curve are in accord with the TO-CVM calculated results. Cao *et al*. did not calculate the values down to 0 K due to numerical difficulties and they will resolve this difficulty in the near future. In short, the agreement between the TP-CSA and TO-CVM calculated IPB energies is encouraging. Indeed Cao *et al*.[122] proceeded to calculate the IPB

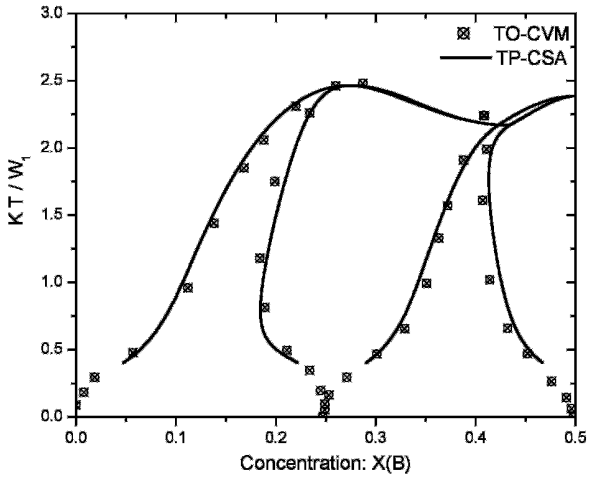

(*a*)

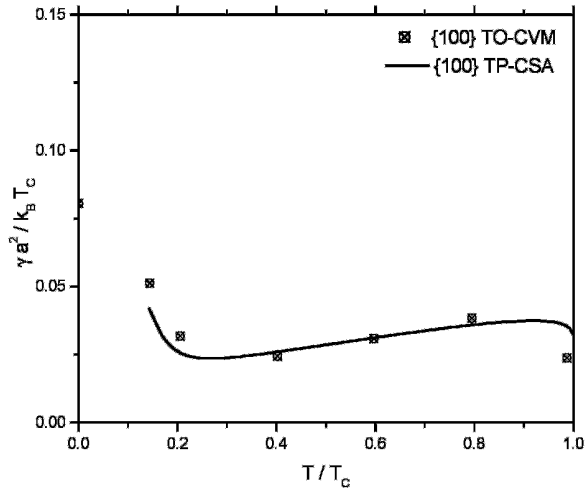

(*b*)

Fig. 42—(*a*) Calculated prototype Cu-Au phase diagram with $\alpha = -0.1$ with the TO-CVM calculated values shown as discrete points[123] and the TP-CSA values as smoothed curves.[122] (*b*) Calculated IPB energies between the fcc and $L1_2$ phases with $\alpha = -0.1$. The TO-CVM calculated values are shown as discrete points[123] and the TP-CSA values as a smoothed curve.[122]

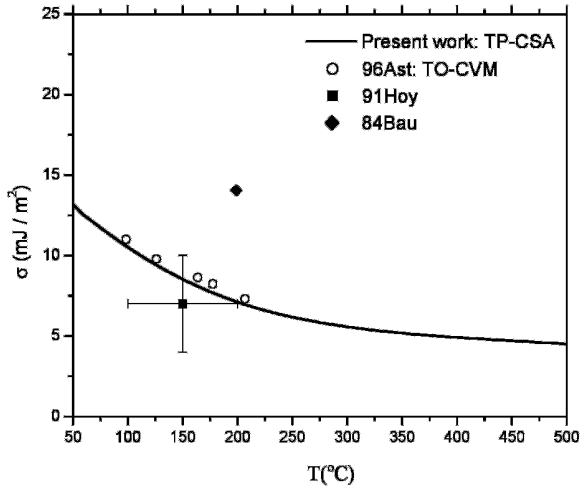

(*a*)

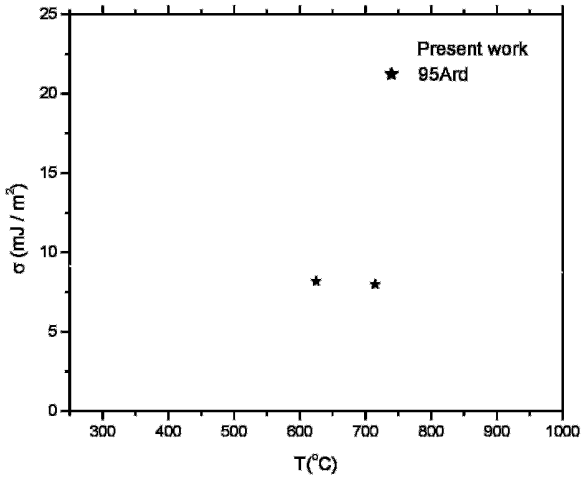

(*b*)

Fig. 43—(*a*) Comparisons of TP-CSA-calculated coherent IPB energies between fcc-(Al) and $L1_2$-Al_3Li[122] with the TO-CVM values[123] and the experimental data.[125,126] (*b*) Comparisons of TP-CSA-calculated coherent IPB energies between γ and γ' in Ni-Al[122] with experimental data.[127,128]

energies between the fcc and $L1_2$ phases in binary Al-Li and Ni-Al.

As shown in Figure 43(a), the TP-CSA calculated IPB energies are in accord with the TO-CVM calculated values.[123] Within the uncertainties of the measurements, there is agreement between the calculated values and the experimental data of Hoyt and Spooner[125] and Baumann and Williams.[126] Figure 43(b) shows that the TP-CSA calculated IPB energies between γ and γ' in Ni-Al are in accord with the experimental values of Ardell.[127] Ardell re-evaluated the data of Marsh and Chen[128] and obtained values in the range of 2 mJ/m^2, which are not shown in this figure. It is worth noting that Dr. Chris Woodward, AFRL/MLLM (Wright-Patterson AFB, OH),[129] shared his calculation of IPB energies between γ and γ' in Ni-Al with me. He used a first principles cluster expansion method coupled with Monte Carlo calculations to estimate the interfacial width and excess free energy in γ and γ' in Ni-Al. For temperatures in the range of experimental measurements (Figure 43(b)), his calculated IPB energies are in good agreement with our estimates, and with the available results from experimental measurements. These results indicate that the CSA, computationally less demanding than the CVM, offers an alternative and perhaps practical approach to calculate (or estimate) coherent IPB energies for γ and γ' in other binary Ni alloys and likely ternary and higher order Ni alloys of practical importance. Graduate students in my group have been exploring the possibility of extending the CSA to calculate IPB energies between γ and γ' to higher order alloys such as Ni-Al-Cr.

The use of CSA to calculate coherent IPB energies was also extended by Cao *et al.*[130] to investigate the effect of the layer-thickness *M* in a multilayered nanostructure on the critical point of an immiscible binary A-B. The symbol *M*

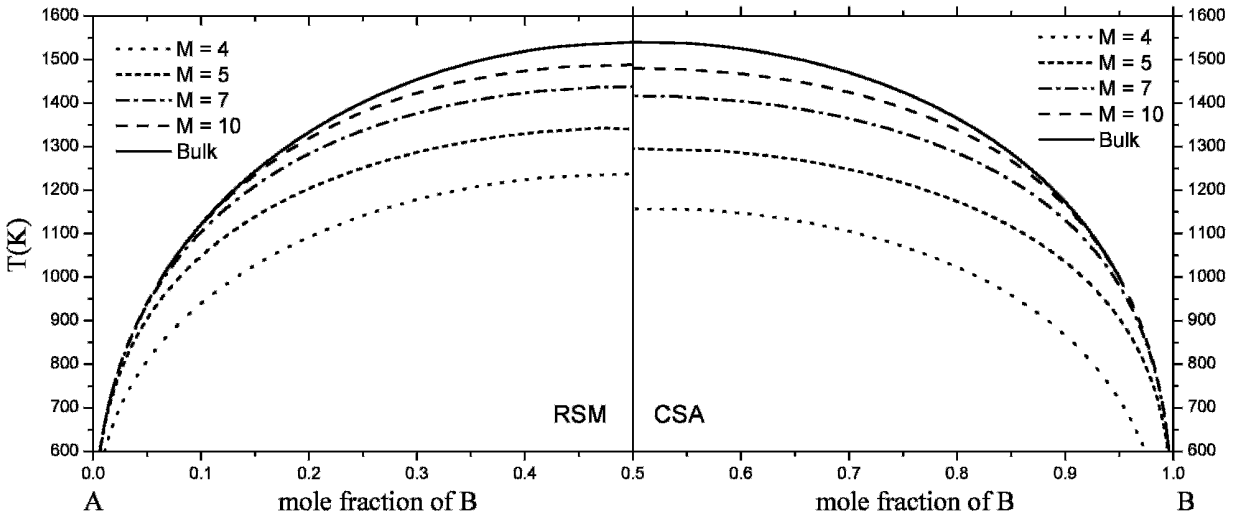

Fig. 44—Calculated phase diagrams of A/B multilayered nanostructure as a function of M using CSA[130] and RSM.[120] The symbol denotes the number of lattice planes per layer of the metal.

denotes the number of lattice planes for each metal layer. When the thickness of a metal layer in such a structure decreases, the contribution of the coherent IPB energy to the total Gibbs energy is no longer small, as for the bulk case. It is this IPB energy that contributes to the lowering of the critical temperature. On the other hand, the surface energy contribution is negligible in a multilayered nanostructure structure since there are only two surfaces and can be neglected. Cao *et al*. showed that CSA-calculated results are essentially the same as the CVM-calculated values[131] but differ somewhat from those calculated using the regular solution model (RSM).[120] Figure 44 shows the effect of decreasing M on the miscibility gap with the solid curve being the miscibility gap for a binary A-B in the bulk. The RSM-calculated gap is plotted from pure A to 50 mol pct B, while the CSA-calculated gap is plotted from 50 mol pct B to pure B. When M decreases, the temperatures of the gap also decrease when compared with that for the bulk alloys. The CSA-calculated temperature of the gap decreases faster than the RSM-calculated one.

V. CONCLUSIONS

This article consists of three major parts on computational thermodynamics: phase diagram calculation in teaching - Section II (see page 2), applications - Section III (see page 10) and research - Section IV (see page 20). In the section on teaching, I presented first the relationships between the topological features of a simple binary phase diagram and the relative thermodynamic stability of the liquid phase *vs* that of the solid phase using a strictly regular solution model. The important message to be conveyed to students is that the characteristic features of phase equilibria are governed by the relative thermodynamic stability of one phase *vs* the other. For instance, under what conditions does maximum congruent melting take place and under what other conditions does a eutectic form? By using either commercial software or one written by a student herself or himself, she or he is able to change the solution parameters and obtain many different types of phase diagrams. An interesting and counterintuitive example is the formation of a closed miscibility gap in a ternary when the regular solution parameters for all three constituent binaries are negative. This occurs when the regular solution parameters for two of them are negative and about the same in value but that of the third binary is appreciably more negative.

Since most commercial alloys are multicomponent, *i.e*., greater than three, often as many as ten, visualization of multicomponent phase diagrams is extremely challenging. Using phase diagram calculation software, the following phase and related diagrams were calculated and presented: (1) a liquidus projection of a quaternary Al-Cu-Mg-Si system in the Al-rich corner, (2) an isopleth, *i.e*., a temperature composition section, (3) a reaction scheme, (4) the phase fractions of a quaternary alloy as a function of temperature when solidified under nonequilibrium conditions, and (5) the liquid compositions as a function of temperature during nonequilibrium solidification. These diagrams provided most of information needed during the solidification of a quaternary Al-Cu-Mg-Si alloy.

In Section III on applications, I provided five examples to show the importance of computational thermodynamics including phase diagram calculations for materials research/development and manufacturing. They are as follows. (1) The use of an efficient strategy to develop a thermodynamic description of Mo-Si-B-Ti using a combined computational/experimental approach, on the basis of which multiphase alloys were identified as potential materials for applications at high temperatures. (2) The use of a calculated isopleth to identify optimum additions of titanium to improve the GFA of a known quaternary $Zr_{56.28}Cu_{31.3}Ni_{4.0}Al_{8.5}$ alloy. The addition of Ti rapidly decreases the liquidus temperature, reaches a minimum at 4.9 mol pct Ti, and then increases again. The GFA of the 4.9 mol pct Ti alloy, *i.e*., $Zr_{51.38}Cu_{31.3}Ni_{4.0}Al_{8.5}Ti_{4.9}$, increases at least 100 pct in terms of the diameter of the cast glass rods. (3) Utilization of calculated fractions of solids formed under nonequilibrium conditions in the weld pool and PMZ to eliminate or at least minimize liquation cracking in Al welds. An Al weld consists of the weld pool diluted with

added fillers and the PMZ. The PMZ is essentially the base metal whose composition differs from that of the weld pool. The criterion for liquation cracking is when the fractions of solid in the weld pool during the later stage of solidification are larger than those of the PMZ. When the reverse is the case, liquation cracking does not occur. The experimental results obtained from many studies are in accord with the calculated fractions of solids in the PMZ and the weld pool. This means one can select an appropriate filler metal based on calculated results using a thermodynamic database of Al alloys.[29] (4) Based on a simple thermodynamic formulation, compositions of (Al,Zr) alloys were calculated to exhibit tendencies to form amorphous thin films obtained *via* a rapid cooling process such as sputter deposition. The calculated alloy compositions were substantiated experimentally. These results indicate that this thermodynamic approach could be used for other alloy systems when their thermodynamic descriptions are available. (5) In the last example, I have shown that computational thermodynamics can be used reliably to calculate the beta transus of Ti6Al4V for certification when a manufacturer sells this metal. This eliminates the costly approach of obtaining this information experimentally for certification for each batch of the metals produced. As long as the compositions of Ti6Al4V are known, the beta transus can be readily calculated in a timely manner.

In Section IV on research, I focused on the potential of using the CSA to describe the fcc phases instead of either the Bragg–Williams approximation or the CVM. The CSA retains the strengths of the Bragg–Williams approximation and is thus computationally less demanding than the CVM while retaining the existence of SRO. Following the Calphad approach but adopting the CSA for the fcc phases instead of the Bragg–Williams approximation, it was shown that the agreement between calculated and experimentally determined stable phase equilibria are as good as previous studies but with fewer parameters. More importantly, the calculated metastable phase diagrams such as the solid-state phase diagrams involving only the fcc phases and the solid/liquid phase diagrams involving the fcc and liquid phases are what one expects. This implies that the thermodynamic driving forces calculated using the CSA should provide more realistic thermodynamic values when studying phase transformations. All research results to date suggest that the CSA can be readily applied to multicomponent systems beyond ternaries. I also presented a brief summary of the modified CEF, based on the Bragg–Williams approximation, by incorporating reciprocal parameters.[118] This modified CEF is able to describe the phase diagram of the prototype Cu-Au binary. It was shown that the ability of this improved CEF to account for the phase diagram of Cu-Au is due to the effect of the reciprocal parameters bringing about the relative stabilization of the enthalpy contribution to the excess Gibbs energy of the disordered phase at the expense of the ordered phase. The configurational entropy of mixing of the disordered phase still corresponds with that for a random solution, *i.e.*, there is no short-range order. The CVM and CSA, on the other hand, account for the phase diagram of Cu-Au in terms of the existence of SRO, *i.e.*, in the entropy contribution to the Gibbs energy.

In addition to phase diagram calculations, the CSA has been used successfully to calculate the IPB energies between the fcc (A1) and $L1_2$ structure not only for prototype Cu-Au alloys but also for two binary systems, *i.e.*, IPB energies between (Al) and Al_3Li and γ and γ' in Ni-Al. It appears promising to extend this approach to higher order alloys.

I have focused in this article only on the Calphad approach using phenomenological models to calculate phase diagrams. On the other hand, it is worth noting that significant advances have also been made in the use of the first principles approach coupled with CVM or cluster expansion to calculate phase diagrams. Readers are referred to an article by van de Walle and Ceder,[132] which uses this approach in calculating prototype phase diagrams without experimental data Even thought it is extremely challenging to extend this approach to calculate phase diagrams of real alloys in agreement with experimentally determined ones, I believe continual advances are being made. Moreover, some of the first principles calculated alloy energetics could be readily used to obtain thermodynamic descriptions of real alloys, particularly for the metastable and unstable phases.

ACKNOWLEDGMENTS

I thank my current graduate students, W. Cao, Jun Zhu, J. Yang, H. Cao, and C.X. Ji, and Postdoctoral Research Associate, Dong Ma; my recent former graduate students, Drs. Y. Yang and P. Ladwig; Professor W.A. Oates, University Salford (Salford, United Kingdom); Drs. F. Zhang and S.-L. Chen, CompuTherm, LLC (Madison, WI); Dr. D. Durrer, Ladish Co. (Cudahy, WI); Professor S. Kou, UW–Madison; and Dr. X.-Y. Yan, Alcoa Technical Center (Alcoa, PA) for all of their help. The financial support from the NSF (Grant No. DMR-0309468), the AFOSR (Grant No. F49620-03-1-0083), the DOE-BES (Grant No. DE-FG-02-99ER45777), the AFMR/ML (Grant No. F33615-98-C-2874), the DARPA (ARO Contract No. DAAD 19-01-1-525), and the Wisconsin Distinguished Professorship is gratefully acknowledged.

REFERENCES

1. T.B. Massalski: *Metall. Trans. B*, 1989, vol. 20B, pp. 445-73.
2. Y.A. Chang and W.A. Oates: "Our Experience in Teaching Thermodynamics at the University of Wisconsin, Madison," 2003, www.tms.org/pubs/journals/JOM/0312/Chang/Chang-0312.html
3. E. Rudy: "Ternary Phase Equilibria in Transition Metal-Boron-Carbon-Silicon Systems, Part IV. Compendium of Phase Diagram Data," AFML-TR-65-2, Wright-Patterson AFB, OH, 1969.
4. A.T. Dinsdale: *CALPHAD*, 1991, vol. 15, pp. 317-425.
5. P. Villars and L.A. Calvert: *Pearson's Handbook of Crystallographic Data for Intermetallic Phases*, ASM, Metals Park, OH, 1985, vol. 3, pp. 2748, 3250.
6. O. Redlich and A.T. Kister: *Ind. Eng. Chem.*, 1948, vol. 40, pp. 345-48.
7. R.R. Hultgren, P.D. Desai, D.T. Hawkins, M. Glesier, and K.K. Kelley: *Selected Values of Thermodynamic Properties of Binary Alloys*, ASM, Metals Park, OH, 1973.
8. T.B. Massalski, J.L. Murray, L.H. Bennett, and H. Baker: *Binary Phase Diagrams*, ASM, Metals Park, OH, 1986.
9. Y.-Y. Chuang, K.-C. Hsieh, and Y.A. Chang: *Metall. Trans. B*, 1985, vol. 16B, pp. 277-85.
10. Y.-Y. Chuang and Y.A. Chang: *Z. Metallkd.*, 1986, vol. 77, 460-66.
11. J.J. Van Laar: *Z. Phys. Chem.*, 1908, vol. 63, pp. 216-53.
12. J.J. Van Laar: *Z. Phys. Chem.*, 1908, vol. 63, pp. 257-97.
13. A.D. Pelton and W.T. Thompson: *Progr. Solid State Chem.*, 1975, vol. 10, pp. 119-55.
14. M. Hasebe and T. Nishizawa: *CALPHAD*, 1980, vol. 4, pp. 83-100.
15. Y.A. Chang and S.-L. Chen: in *Advanced Physical Chemistry in Process Metallurgy*, N. Sano, W.-K. Lu, and P.V. Riboud, eds., Academic Press Ltd., London, 1997, pp. 5-41.

16. H.L. Lukas, J. Weiss, and E.-T. Henig: *CALPHAD*, 1982, vol. 6, pp. 229-51.
17. B. Sundman, B. Jansson, and J.-O. Anderson: *CALPHAD*, 1985, vol. 9, pp. 153-90.
18. A.T. Dinsdale, S.M. Hodson, T.I. Barry, and J.R. Taylor: *Proc. 27th Annual Conf. of Metallurgists*, CIM, Montreal, 1988, vol. 11, pp. 59-68.
19. G. Eriksson and K. Hack: *Metall. Trans. B*, 1990, vol. 21B, pp. 1013-23.
20. W.T. Thompson, G. Eriksson, C.W. Bale, and A.D. Pelton: in *High Temperature Materials Chemistry*, Electrochemical Society, Inc., Pennington, NJ, 1997, pp. 16-30.
21. WinPhad software for multicomponent phase diagram calculations by CompuTherm, LLC, Madison, WI, since 1998.
22. PANDAT software for multicomponent phase diagram calculations by CompuTherm, LLC, Madison, WI, since 2000.
23. S.-L. Chen, F. Zhang, S. Daniel. F.-X. Xie, X.-Y. Yan, Y.A. Chang, R. Schmid-Fetzer, and W.A. Oates: *JOM*, 2003, vol. 55, pp. 48-52.
24. C.W. Bale, P. Chartrand, S.A. Degterov, G. Erisson, K. Hack, R. Ben Mahfoud, J. Melancon, A.D. Pelton, and S. Peterson: *CALPHAD*, 2002, vol. 26, pp. 189-228.
25. J.L. Meijering: *Philips Res. Rep*., 1950, vol. 5, pp. 333-56.
26. J.L. Meijering: *Philips Res. Rep*., 1951, vol. 6, pp. 183-210.
27. J.L. Meijering and H. K. Hardy: *Acta Metall*., 1956, vol. 4, pp. 249-56.
28. Y.A. Chang, J.P. Neumann, A. Mikula, and D. Goldberg: *INCRA Monograph VI, Phase Diagrams and Thermodynamic Properties of Ternary Copper-Metal Systems*, The International Copper Research Association, Inc., New York, NY, 1979.
29. PanAluminium, a thermodynamic database for aluminum alloys with 16 elements by CompuTherm, LLC, Madison, WI, since 1998, but has been continually updated.
30. F. Rhines: *Phase Diagrams in Metallurgy, Their Development and Applications*, McGraw-Hill, New York, NY, 1951.
31. Y.A. Chang, J.P. Neumann, and U.V. Choudary: *INCRA Monograph VII, Phase Diagrams and Thermodynamic Properties of Ternary Copper-Sulfur-Metal Systems*, The International Copper Research Association, Inc., New York, NY, 1979.
32. Y.A. Chang and K.-C. Hsieh: *Phase Diagrams of Ternary Copper-Oxygen-Metal Systems*, ASM INTERNATIONAL, Metals Park, OH, 1989.
33. Y.A. Chang, X.-Y. Yang, F.-Y. Xie, and S.-L. Chen: in *Solidification of Aluminum Alloys*, Men G. Chu, D. Granger, and H. Han, eds., TMS, Warrendale, PA, 2004, pp. 3-18.
34. J.F. Loffer: *Intermetallic*, 2003, vol. 11, pp. 529-40.
35. Y. Yang, Y.A. Chang, L. Tan, and Y. Du: *Mater. Sci. Eng. A*, 2003, vol. 361, pp. 281-93.
36. Y. Yang: Ph.D. Thesis, University of Wisconsin, Madison, WI, 2004.
37. Y. Yang, Y.A. Chang, L. Tan, and W. Cao: *Acta Mater*., 2005, vol. 53, pp. 1711-20.
38. Y. Yang, Y.A. Chang, and L. Tan: *Intermetallics*, 2005, vol. 13, pp. 1110-15.
39. Y. Yang and Y.A. Chang: *Intermetallics*, 2005, vol. 13, pp. 121-28.
40. H. Nowotny, E. Dimakopoulou, and H. Kudielka: *Mh. Chem*., 1957, vol. 88, pp. 180-92.
41. J.H. Perepezko, R. Sakidja, and S. Kim: *Materials Research Society Symposia Proc*., Materials Research Society, Pittsburgh, PA, 2001, vol. 646, pp. N4.5.1-4.5.12.
42. D.M. Berczik: United States Patent 5,595,616, 1997.
43. D.M. Berczik: United States Patent 5,693,156, 1997.
44. M.K. Meyer, M.J. Kramer, and M. Akinc: *Intermetallics*, 1996, vol. 4, pp. 273-81.
45. E. Strom, J. Zhang, and D. Feng: *Trans. Nonferrous Metals Society of China*, 2002, vol. 12 (4), pp. 676-80.
46. Y.A. Chang, S.-L. Chen, F. Zhang, X.-Y. Yan, F.-Y. Xie, R. Schmid-Fetzer, and W.A. Oates: *Progr. Mater. Sci*., 2004, vol. 49, pp. 313-45.
47. Y. Liu, G. Shao, and P. Tsakiropoulos: *Intermetallics*, 2000, vol. 8, pp. 953-62.
48. K.E. Spear and P.K. Liao: *Bull. Alloy Phase Diagram*, 1988, vol. 9, pp. 457-66.
49. N. Saunders: in *COST 507*, I. Ansara, A.T. Dinsdale, and M.H. Rand, eds., European Communities, Luxembourg, 1988.
50. S.K. Lim and H.L. Lukas: in *COST 507*, I. Ansara, A.T. Dinsdale, and M.H. Rand, European Communities, Luxembourg, 1998, vol. 2.
51. H.J. Seifert, H.L. Lukas, and G. Petzow: *Z. Metallkd*., 1996, vol. 87, pp. 2-13.
52. C. Baetzner: Thesis, Max Planck Institut-PML, Stuttgart, Federal Republic of Germany, 1994.
53. U.R. Kattner: *JOM*, 1997, vol. 49 (12), pp. 14-19.
54. D. Xu, G. Duan, and W.L. Johnson: *Phys. Rev. Lett*., 2004, vol. 92, p. 245504.
55. Z.P. Lu, C.T. Liu, J.R. Thompson, and W.D. Porter: *Phys. Rev. Lett*., 2004, vol. 92, pp. 245503/1-245503/4.
56. D. Ma, H. Cao, K.C. Hsieh, L. Ding, and Y.A. Chang: *Appl. Phys. Lett*., 2005, vol. 87, pp. 171914/1-171914/3.
57. X.Y. Yan, Y.A. Chang, Y. Yang, F.Y. Xie, S.L. Chen, F. Zhang, S. Daniel, and M.H. He: *Intermetallics*, 2001, vol. 9, pp. 535-38.
58. A. Inoue: *Acta Mater*., 2000, vol. 48, pp. 279-306.
59. D. Turnbull: *Contemp. Phys*., 1969, vol. 10, pp. 473-88.
60. Z.P. Lu and C.T. Liu: *Phys. Rev. Lett*., 2003, vol. 91, pp. 115505/1-115505/4.
61. G.E. Metzger: *Welding J*., 1967, vol. 46 (10), pp. 457S-469S.
62. N.F. Gittos and M.H. Scott: *Welding J*., 1981, vol. 60 (6), pp. 95S-103S.
63. M. Katoh and H.W. Kerr: *Welding J*., 1987, vol. 66 (12), pp. 360S-368S.
64. H.W. Kerr and M. Katoh: *Welding J*., 1987, vol. 66 (9), pp. 251S-259S.
65. M. Miyazaki, K. Nishio, M. Katoh, M. Mukae, and H.W. Kerr: *Welding J*., 1990, vol. 69 (9), pp. 362S-371S.
66. M.B.D. Ellis, M.F. Gittos, and I. Hadley: *The Welding Inst. J. (UK)*, 1997, vol. 6 (2), pp. 213-55.
67. C. Huang and S. Kou: *Sci. Technol. Welding Joining*, 2004, vol. 9, pp. 149-57.
68. C. Huang and S. Kou, *Welding J*., 2004, vol. 83, pp. 111S-122S.
69. S.A. Wolf, D.D. Awschalom, R.A. Buhrman, J.M. Daughton, S. von Molnár, M.L. Roukes, A.Y. Chtchelkanova, and D.M. Treger: *Science*, 2001, vol. 294, pp. 1488-95.
70. J.S. Moodera, L.R. Kinder, T.M. Wong, and R. Meservey: *Phys. Rev. Lett*., 1995, vol. 74, pp. 3273-76.
71. Zutic, J. Fabian, and S.D. Sarma: *Rev. Mod. Phys*., 2004, vol. 76, pp. 323-410.
72. G.A. Prinz: *Science*, 1998, vol. 282, pp. 1660-63.
73. H. Shim, B.K. Cho, J. Kim, T.W. Kim, and W.J. Park: *J. Appl. Phys*., 2003, vol. 93, pp. 7026-28.
74. J.S. Moodera, J. Nassar, and G. Mathon, *Ann. Rev. Mater. Sci*., 1999, vol. 29, pp. 381-432
75. E.Y. Tsymbal, O.N. Mryasov, and P.R. LeClair: *J. Phys., Condens. Matter*, 2003, vol. 15, pp. R109-R142.
76. K. Ohashi, K. Hayashi, K. Nagahara, K. Ishihara, E. Fukami, J. Fujikata, S. Mori, M. Nakada, T. Mitsuzuka, K. Matsuda, H. Mori, A. Kamijo, and H. Tsuge: *IEEE Trans. Magn*., 2000, vol. 36, pp. 2549-53.
77. J.J. Sun, K. Shimazawa, N. Kasahara, K. Sato, T. Kagami, S. Saruki, S. Araki, and M. Matsuzaki: *J. Appl. Phys*., 2001, vol. 89, pp. 6653-55.
78. Z.G. Zhang, P.P. Freitas, A.R. Ramos, N.P. Barradas, and J.C. Soares: *Appl. Phys. Lett*., 2001, vol. 79, pp. 2219-21.
79. J.R. Childress, M.M. Schwickert, R.E. Fontana, M.K. Ho, P.M. Rice, and B.A. Gurney: *J. Appl. Phys*., 2001, vol. 89, pp. 7353-55.
80. J.J. Yang, P.F. Ladwig, Y. Yang, C.-X. Ji, Y.A. Chang, F.X. Liu, B.B. Pant, and A.E. Schultz: *J. Appl. Phys*., 2005, in press.
81. P.F. Ladwig, J.J. Yang, Y. Yang, F. Liu, B.B. Pant, A.E. Schultz, and Y.A. Chang: *Appl. Phys. Lett*., 2005, vol. 87, pp. 061901/1-061901/3.
82. S. Lee, C. Choi, and Y. Kim: *Appl. Phys. Lett*., 2003, vol. 83, pp. 317-19.
83. E. Ma and M. Atzmon: *Phys. Rev. Lett*., 1991, vol. 67, pp. 1126-29.
84. E. Ma, F. Brunner, and M. Atzmon: *J. Phase Equilibria*, 1993, vol. 14, pp. 137-41.
85. H.J. Fecht, G. Han, Z. Fu, and W.L. Johnson: *J. Appl. Phys*., 1990, vol. 67, pp. 1744-48.
86. H. Yoshioka, H. Habazaki, A. Kawashima, K. Asami, and K. Hashimoto: *Electrochimica Acta*, 1991, vol. 36, pp. 1227-33.
87. J. Ho and K. Lin: *J. Appl. Phys*., 1994, vol. 75, pp. 2434-40.
88. J.J. Yang, Y. Yang, and Y.A. Chang: *J. Appl. Phys*., 2005, vol. 98, 074508/1-074508/6.
89. T. Wang, Z. Jin, and J. Zhao: *J. Phase Equilibria*, 2001, vol. 22, pp. 544-51.
90. D.B. Williams and C.B. Carter: *Transmission Electron Microscopy: A Textbook for Materials Science*, Plenum Press, New York, NY, 1996, pp. 474-75.
91. F. Zhang: CompuTherm, LLC, Madison, WI, private communication, 2004.
92. Pan Titanium, a Thermodynamic Database for Titanium Alloys by CompuTherm, LLC, Madison, WI, since 2002, but has been continually updated.
93. W.L. Bragg and E.J. Williams: *Proc. R. Soc*., 1934, vol. A145, pp. 699-730.

94. W.L. Bragg and E.J. Williams: *Proc. R. Soc*., 1934, vol. A151, pp. 540-66.
95. W.L. Bragg and E.J. Williams: *Proc. R. Soc*., 1935, vol. A152, pp. 231-52.
96. J.O. Anderson, A.F. Guillermet, M. Hillert, B. Jason, and B. Sundman: *Acta Metall*., 1986, vol. 34, pp. 437-45.
97. W. Shockley: *J. Chem. Phys*., 1938, vol. 6, pp. 130-44.
98. D. de Fontaine: *Solid State Phys*., 1979, vol. 34, pp. 73-274.
99. D. de Fontaine: *Solid State Phys*., 1994, vol. 47, pp. 33-176.
100. R. Kikuchi: *Phys. Rev*., 1951, vol. 81, pp. 988-1003.
101. R. Kikuchi and C.M. Van Baal: *Scripta Metall*., 1974, vol. 8, pp. 425-28.
102. J.M. Sanchez and D. de Fontaine: *Phys. Rev. B*, 1978, vol. 17, pp. 1926-36.
103. W.A. Oates and H. Wenzl: *Scripta Mater*., 1996, vol. 35, pp. 623-27.
104. W.A. Oates, F. Zhang, S.-L. Chen, and Y.A. Chang: *Phys. Rev. B*, 1999, vol. 59, pp. 11221-11225.
105. J. Zhang, W.A. Oates, F. Zhang, S.-L. Chen, K.-C. Chou, and Y.A. Chang: *Intermetallics*, 2001, vol. 9, pp. 5-8.
106. F. Zhang, Y. Du, W.A. Oates, S.-L. Chen, and Y.A. Chang: *Acta Mater*., 2003, vol. 51, pp. 207-16.
107. W. Cao, Y.A. Chang, J. Zhu, S.-L. Chen, and W.A. Oates: *Acta Mater*., 2005, vol. 53, pp. 331-35.
108. W. Cao, J. Zhu, Y. Yang, F. Zhang, S.-L. Chen, W.A. Oates, and Y.A. Chang: *Acta Mater*., 2005, vol. 53, pp. 4189-97.
109. B. Sundman, S.G. Fries, and W.A. Oates: *CALPHAD*, 1998, vol. 22, pp. 355-57.
110. C.N. Yang and Y. Li: *Chin. J. Phys*., 1947, vol. 7, pp. 59-71.
111. R. Kikuchi, R. Sanchez, D. de Fontaine, and H. Yamauchi: *Acta Metall*., 1980, vol. 28, pp. 651-62.
112. S.-L. Chen, S. Daniel, F. Zhang, Y.A. Chang, W. A. Oates, and R. Schmid-Fetzer: *J. Phase Equilibria*, 2001, vol. 22, pp. 373-78.
113. S.-L. Chen, S. Daniel, F. Zhang, Y.A. Chang, X.-Y. Yan, F.-Y. Xie, R. Schmid-Fetzer, and W.A. Oates: *CALPHAD*, 2002, vol. 26, pp. 175-88.
114. S. Ochiai, Y. Oya, and T. Suzuki: *Bull. P M E (T I T)*, 1983, vol. 52, pp. 1-17.
115. Y.M. Hong, H. Nakayima, Y, Mishima, and T. Suzuki: *Iron Steel Inst. Jpn. Int*., 1989, vol. 29, pp. 78-84.
116. A. Pasture, K. Colinet, A.T. Paxton, and M.J. Schilfgaarde: *J. Phys., Condens. Matter*, 1992, vol. 4, pp. 945-59.
117. H.-M. Huang and Y.A. Chang: *Intermetallics*, 1998, vol. 6, pp. 487-98; Corrigendum: *Intermetallics*, 1999, vol. 7, pp. 625-26.
118. A. Kusoffsky, N. Dupin, and B. Sundman: *CALPHAD*, 2001, vol. 25, pp. 549-65.
119. T. Abe and B. Sundman: *CALPHAD*, 2003, vol. 27, pp. 403-08.
120. Y.W. Lee and H.I. Aaronson: *Acta Metall*., 1980, vol. 28, pp. 439-547.
121. R. Kikuchi and J.W. Cahn: *Acta Metall*., 1979, vol. 27, pp. 1337-53.
122. W. Cao, J. Zhu, S.-L. Chen, W.A. Oates, M. Asta, and Y.A. Chang: *Acta Mater*., 2005, in press.
123. M. Asta: in *Theory and Applications of the Cluster Variation method and Path Probability Methods*, J.L. Moran-Lopez and J.M. Sanchez, eds., Plenum Press, New York, NY, 1996, pp. 237-54.
124. V.G. Vaks and G.D. Samolyuk: *J. Exp. Theor. Phys*., 1999, vol. 88, pp. 89-100.
125. J.J. Hoyt and S. Spooner: *Acta Metall*., 1991, vol. 39, pp. 689-93.
126. S.F. Baumann and D.B. Williams: *Scripta Metall*., 1984, vol. 18, 611-16.
127. A.J. Ardell: *Interface Sci*., 1995, vol. 3, pp. 119-25.
128. C. Marsh and H. Chen: *Acta Metall*., 1990, vol. 38, pp. 2287-98.
129. C. Woodward: AFRL/MLLM, Wright-Patterson AFB, OH, private communication, 2004.
130. W. Cao, J. Zhu, Y. Yang, W.A. Oates, and Y.A. Chang: *Scripta Mater*., vol. 53, pp. 1379-82.
131. R. Kikuchi and L.-Q. Chen: *Nanostr. Mater*., 1995, vol. 5, pp. 257-68.
132. A. van de Walle and G. Ceder: *J. Phase Equilibria*, 2002, vol. 23, pp. 348-59.